Final work : Modeling of a fan blade-off event for electric fan thruster

Auteur : Bonet Jara, Belen
Promoteur(s) : Ponthot, Jean-Philippe
Faculté : Faculté des Sciences appliquées
Diplôme : Master en ingénieur civil en aérospatiale, à finalité spécialisée en "turbomachinery aeromechanics (THRUST)"
Année académique : 2022-2023
URI/URL : http://hdl.handle.net/2268.2/18156

MSc in Turbomachinery Aeromechanics (THRUST)

University of Liège - School of Engineering and Computer Science

---

Modeling of a Fan Blade-Off Event

for

Electric Fan Thruster

Author
Belén Bonet Jara

Academic Promoter (ULiège)
Prof. Jean-Phillippe Ponthot

KTH Supervisor
Prof. Nenad Glodic

Master thesis completed in order to obtain the degree of Master of Science in Civil Engineer in Aerospace, specialization in "turbomachinery aeromechanics"

Academic year 2022–2023

Members of the jury

Prof. Jean–Philipe PONTHOT, *Academic Promoter*
University of Liège, Faculty of Engineering (Liège, Belgium)
Department of Aerospace & Mechanical engineering
Computational Mechanics Laboratory (MN2L)

Prof. Nenad GLODIC, *KTH Supervisor and Director of the THRUST Program*
KTH Royal Institute of Technology (Stockholm, Sweden)
Unit of Heat and Power Technology
Brinellvägen, 68

Prof. Ludovic NOELS
University de Liège, Faculty of Engineering (Liège, Belgium)
Department of Aerospace & Mechanical engineering
Computational & Multiscale Mechanics of Materials (CM3)

Abstract

This MSc Thesis provides a comprehensive exploration of the electric fan thruster that is being developed under the *EleFanT* project, a collaborative effort between GKN Aerospace and KTH - Royal Institute of Technology. This project's primary objective is the development and analysis of a preliminary numerical model for the Hard-wall Containment design of the fan case, with a specific focus on addressing the challenges posed by Fan Blade-Off (FBO) events in aviation engines.

The thesis commences by detailing the key characteristics of the developed numerical model and the analytical methodologies employed to ensure its accuracy and reliability. General simulation conditions are established to serve as a baseline reference point. The study proceeds to examine the sensitivity of results to blade meshing within the elastic region, aiming to determine the optimal meshing configuration for the blade component. Subsequently, a similar sensitivity analysis is conducted at the system level, encompassing the entire Hard-wall Containment model. The outcomes of these analyses inform the final configuration selection while also acknowledging potential limitations in the model's representation.

The analysis deepens the understanding of the dynamic behavior of FBO events, with a focus on quantifying energy transfers and forces generated during distinct impact phases. A primary emphasis is placed on comprehending forces transmitted to the engine structure. Insights are drawn from analysis of time-evolving force signals, revealing the significance of considering vibrational forces experienced by the fan case following blade detachment.

The research culminates in a series of significant findings. The study demonstrates the pivotal role of energy transfers in dissipating kinetic energy, particularly through friction and blade deformation. Furthermore, the containment capability of the fan case is evaluated, yielding promising results that suggest its potential effectiveness in containing detached blades.

The findings illuminate the intricate dynamics of FBO events, and the various difficulties in constructing a reliable and realistic numerical model to represent it. The study also underscores the need for future research to delve deeper into the model's complexities and explore avenues for improvement. Given the project's scope, various facets remain ripe for further investigation, including refining meshing techniques, experimental validation, and exploring advanced failure criteria. This investigation represents a fundamental stride in propelling the enhancement of safety and efficiency within the *EleFanT* project's engine development, thereby establishing a pathway for continuous advancements in this critical realm.

Acknowledgement

This manuscript stands as the culmination of a remarkable two-year journey, a voyage replete with invaluable lessons and experiences that have shaped me. It bears testament to the ceaseless dedication required to amass the necessary knowledge that molds a proficient aerospace engineer. Yet, the heart of our industry resides in collaboration, a symphony of synergies that is imperative for the remarkable advancement of aviation technology. Gazing backward, in my own odyssey, this truth remains unaltered. Without all the individuals who have crossed my path, since the moment I decided to venture beyond my home country to embrace loftier aspirations, this achievement would have remained but a distant dream.

First and foremost, my gratitude extends deeply to my parents, Belén and Vicente, unwavering pillars of support, beacons of guidance, and wellsprings of encouragement throughout my academic pursuits. I am deeply appreciative of the barriers they have dismantled for me and for their imparted wisdom on the value of perseverance and dedication.

Next, I would like to acknowledge the pivotal contribution of my brother, Jorge, whose academic journey has served as the fruit of my inspiration as long as I can remember. I am grateful to have witnessed the rewards that come from the pursuit of excellence and for his encouragement and enriching discussions, fountains of motivation that have bolstered me during the toughest moments.

To my grandmothers, Maruja and Carmen, and the rest of my family, whose steadfast belief in my capabilities has been instrumental in my accomplishments, and whose unconditional love has been an essential wellspring of strength, I extend my deepest appreciation.

To each and every individual whom I have crossed paths with and whom I am fortunate to call friends. These cherished companions, who oftentimes know me better than I comprehend myself, have intuitively lent their support during times of heaviest burdens. These friends, who have served as impromptu teachers, have enriched my journey with indelible lessons.

Of course, a special tribute is owed to the person who has journeyed alongside me for countless hours. Thank you, Irene, for making me lose count of all that you have given me over these two years. Your generosity knows no bounds, and your unwavering support has been the constant that carried me when I needed it most.

Finally, I owe a debt of gratitude to my two esteemed mentors and advisors for their expert guidance and support throughout this endeavor. Thank you, Jean-Philippe, for your meticulous and

enlightening explanations, your dedicated involvement in this project, and for your infectious passion for this engineering field. Your valuable insights, feedback, and mentorship have profoundly influenced the direction and outcomes of this research. Thank you, Nenad, for closely accompanying and encouraging me over these two years. I am privileged to have had the opportunity to work on the *EleFanT* project under your guidance, and I extend my heartfelt appreciation to all those involved in making this opportunity possible.

Thank you all for being an integral part of my journey and for your relentless belief in my potential to become the engineer I have always aspired to be.

Abbreviations

FBO - **F**an **B**lade-**O**ff

FEA - **F**inite **E**lement **A**nalysis

FE - **F**inite **E**lement

FEM - **F**inite **E**lement **M**ethod

FAA - **F**ederal **A**viation **A**dministration [5]

EASA - **E**uropean union **A**viation **S**afety **A**gency [4]

CFRP - **C**arbon **F**iber **R**einforced **P**lastic

SI - **I**nternational **S**ystem of Units

RB - **R**eleased **B**lade

TB - **T**railing **B**lade

FC - **F**an **C**ase

Contents

Chapter 1

Introduction

This chapter provides a general introduction to the context in which this thesis has been realized. Its objective is to clearly establish the foundations of the sense and motivation that have led to its development, as well as to provide initial notions of some of the concepts involved that are repeatedly mentioned throughout this report.

First, the historical context of the fan blade-off phenomenon is highlighted in Section 1.1. This part details how this phenomenon became a concern for the pertinent authorities and how its treatment has evolved throughout the years. Next, in Sections 1.1.1 and 1.1.2, a general explanation of airworthiness guidelines and their extrapolation to real-world practices in the industry is given. Finally, the motivations and objectives from which this work has emerged are detailed in Section 1.2, providing an overview of the project from which it originates, EleFanT [11], and outlining the expected objectives upon its completion.

1.1 Context

Fan blade-off (FBO) events have been a significant concern in the aviation industry since the early days of commercial flights. The catastrophic effects of a fan blade failure, such as severe damage to the aircraft and injuries or loss of life to passengers and crew, have driven research into developing better containment systems and mitigation techniques to prevent or minimize the impact of such events.

The first recorded FBO event occurred in 1953 during a test flight of a de Havilland Comet 1 aircraft, as reported by the UK's Air Accident Investigation Branch [8]. The aircraft was conducting a series of test flights to evaluate its performance and airworthiness prior to its entry into commercial service with British Overseas Airways Corporation. During the test flight, the

aircraft experienced a sudden loss of power and control, followed by a loud bang and vibrations. The crew quickly identified that one of the aircraft's four Rolls-Royce Avon turbojet engines had suffered a catastrophic failure, which had caused one of the engine's compressor blades to detach and penetrate into the wing. A further study conducted by the Federal Aviation Administration (FAA) showed that over the subsequent few decades, between 1969 and 1997, there were a total of 676 uncontained engine failure events in fixed wing aviation [15], including the 1973 National Airlines Flight 27, the 1984 Aeroflot Flight 3519, and the 1985 British Airtours Flight 28M [56]. However, the most notable event occurred in 1989 when United Airlines Flight 232 experienced an engine failure due to uncontained engine debris of its tail-mounted engine [55]. The failure was caused by the separation of a fan disk due to a crack that was originated during the manufacturing process and was propagated due to fatigue stresses. As it can be appreciated from Fig. 1.1, the debris from the failure caused extensive damage to the aircraft, resulting in the loss of its hydraulic systems, therefore limiting its control. The incident resulted in a crash that claimed the lives of 111 people. Following this accident, regulatory agencies around the world, including the FAA, the European Aviation Safety Agency (EASA), and the International Civil Aviation Organization, established more stringent inspection and maintenance requirements for fan blades and other engine components.

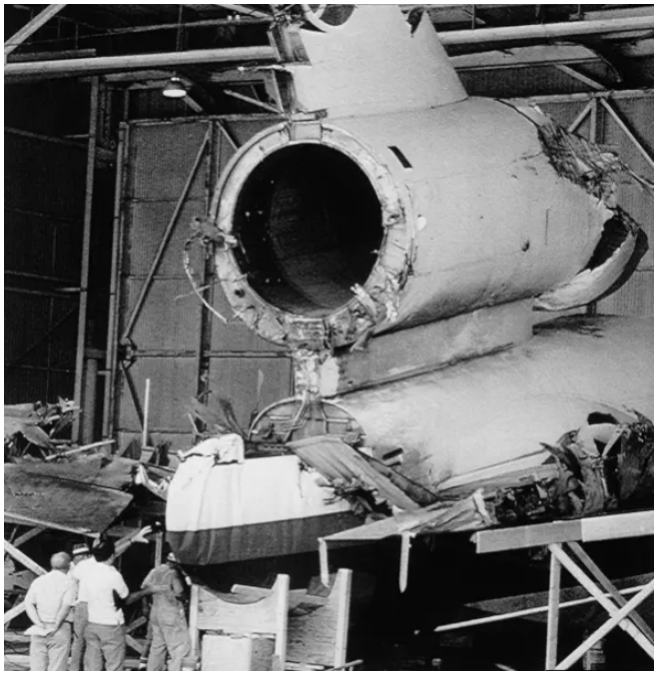

Figure 1.1: Reconstruction of the United Airlines 232's tail section, July 28, 1989 [32].

In this context, FBO events are rare but potentially catastrophic occurrences. These events involve high-energy and high-speed interactions between various engine components, such as released blades, neighbouring blades, containment structures, bearings, and mounting attachments.

There are different possible causes why a fan blade may break off. Amongst others, it can be due to **foreign object damage** like bird-strike, **fatigue failure** at the dovetail, or **manufacturing defects** that lead to stress concentration zones. To prevent damage to the aircraft and ensure passenger safety, it is essential that the critical structures are designed to allow it to continue flying while the engine is being shut down. It is also crucial to concentrate the damage inside the engine, for which the containment capability and absorption of the kinetic energy of the released fragments of the casing is of paramount importance. The released blade undergoes high plastic deformations and may fragment, and the same happens with the trailing blade, which is the blade immediately next to the failed one. Depending on the configuration, the casing may also suffer high deformations and even be pierced to trap the blade in an external containment wrap.

It is difficult to estimate the frequency of FBO events as it depends on several factors, including the number of flights, the type of aircraft, and the maintenance procedures in place. To understand the causes of FBO events, various approaches have been taken, including laboratory tests, engine monitoring, and data analytics. Laboratory tests involve subjecting engine components, including fan blades, to simulated operating conditions to determine their failure modes and develop strategies to prevent them. These tests can identify specific factors, such as material fatigue and stress, that contribute to fan blade failure [41]. Engine monitoring involves collecting real-time data from engines in service to detect abnormalities that may indicate potential blade failure. Data analytics involves using machine learning algorithms to analyze large amounts of data from various sources, including engine performance data, maintenance records, and weather conditions, to identify patterns and predict possible failures.

Figure 1.2: Damaged engine fan case from blade-off testing [39].

Additionally, more advanced inspection methods, such as eddy current testing and microwave signals, are now used to detect cracks and other defects in fan blades [42]. These inspections can identify potential problems before they become critical and allow for the timely replacement of

damaged blades. Finally, some aircraft are equipped with sensors that can detect vibrations and other abnormal engine behavior, allowing for early detection and prevention of fan blade failures [23].

Several mitigation techniques have been developed to reduce the risk of FBO events. One approach is to use alternative materials to more traditional metals, such as composite materials, in fan blade construction [36]. These materials offer a higher resistance to fatigue and damage, reducing the likelihood of blade failure through this mechanism. Moreover, they align with one of the primary objectives of aviation, which is the minimization of total weight. Nevertheless, there are also limitations such as their higher susceptibility to damage from impact, like bird strikes or debris ingestion, or the loss of properties due to time degradation.

Given the unpredictability of the reason for blade failure, it opens the possibility to also evaluating the problem from the perspective of improving containment capability [19, 28, 48, 49, 53]. One approach for this type of analysis is through computer simulation and modeling [59]. Finite Element Analysis (FEA) is commonly used to simulate the high-energy impact and to predict the evolution of fan blade debris in the event of failure. This approach allows engineers to evaluate different containment system designs and assess their effectiveness in preventing debris from damaging critical components. Another approach is through physical testing of containment systems using high-speed cameras and other specialized instrumentation [58, 57]. Through this approach, engineers can observe the real trajectory of fan blade debris in a controlled environment.

In conclusion, FBO events remain a significant safety concern in the aviation industry. While relevant progress has been made in understanding its causes and developing mitigation techniques, continued research and development are required to further improve safety. Approaches such as laboratory testing, engine monitoring, and data analytics can help identify the factors that contribute to blade failure, while using more durable materials and advanced inspection methods can reduce the likelihood of failures occurring. Ultimately, ongoing efforts to develop effective fan blade containment systems will play a vital role in ensuring the continued safety of the aviation industry.

1.1.1 FAA Regulations Governing Blade Containment

In the wake of FBO events, regulatory agencies have made significant efforts to establish comprehensive certification requirements to ensure the safety of passengers and crew, as well as the critical systems of the aircraft. Different countries have their own regulations for FBO events, with, for instance, the FAA[1] in the U.S. [24], EASA in Europe, and CAAC in China having fairly similar guidelines. To be certified, an engine must pass rigorous tests, including the ability to withstand catastrophic engine failure. One of the key tests is the FBO test, which involves the loss of one of

[1]The present work focuses specifically on this regulation.

the fan blades. Although blades from any component of the engine are expected to be contained, fan blades are typically the most energetic due to the trend towards higher bypass ratios, resulting in longer and heavier blades, potentially increasing the kinetic energy (for the same velocity) of the impact and posing a greater risk for catastrophic impact.

These regulations also mandate that engine manufacturers conduct a certification test to demonstrate that the most critical blade can be contained when released at the engine's maximum rotating speed. This test involves two primary objectives: not causing an engine fire and not fracturing the fan case or mounting attachments when operated for at least 15 seconds after blade loss. But most importantly, the FAA acknowledges the use of analytical techniques and numerical simulation as equivalent to rig tests. More detailed information about this particular federal regulation can be extracted from Fig. 1.3. This approach enables companies to develop their own certification methodologies, which can be more cost-effective and efficient while still ensuring the safety and integrity of the aircraft.

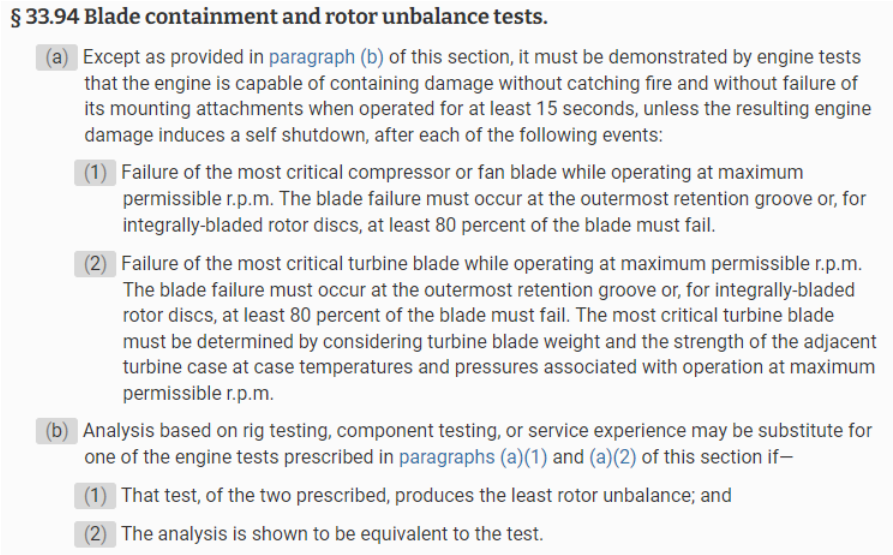

§ 33.94 Blade containment and rotor unbalance tests.

(a) Except as provided in paragraph (b) of this section, it must be demonstrated by engine tests that the engine is capable of containing damage without catching fire and without failure of its mounting attachments when operated for at least 15 seconds, unless the resulting engine damage induces a self shutdown, after each of the following events:

(1) Failure of the most critical compressor or fan blade while operating at maximum permissible r.p.m. The blade failure must occur at the outermost retention groove or, for integrally-bladed rotor discs, at least 80 percent of the blade must fail.

(2) Failure of the most critical turbine blade while operating at maximum permissible r.p.m. The blade failure must occur at the outermost retention groove or, for integrally-bladed rotor discs, at least 80 percent of the blade must fail. The most critical turbine blade must be determined by considering turbine blade weight and the strength of the adjacent turbine case at case temperatures and pressures associated with operation at maximum permissible r.p.m.

(b) Analysis based on rig testing, component testing, or service experience may be substitute for one of the engine tests prescribed in paragraphs (a)(1) and (a)(2) of this section if—

(1) That test, of the two prescribed, produces the least rotor unbalance; and

(2) The analysis is shown to be equivalent to the test.

Figure 1.3: FAA regulation regarding FBO certification: 14 CFR § 33.94 [24].

At this point, it is important to emphasize that the work carried out in this thesis is not a certification process, but rather the establishment of the foundations for a numerical model that, in future versions, will be capable of faithfully reproducing the FBO event.

1.1.2 Airworthiness compliance

Rig testing has historically been utilized for certification of engines, from single-component testing to highly expensive whole engine testing [54]. In order to simulate engine conditions, it is necessary to comprehend the fundamental requirements for FBO test engine configuration. These conditions

involve the engine running at full power while the base of the fan blade is fractured by an explosive charge to produce the release. Experimental tests have shown that plasticity/yielding and blade tip friction rubbing are significant factors, including large rotations, multi-body contact, sliding friction, and inelastic deformation. Furthermore, it would be imperative to conduct this testing for all phases of the design process, as there may be changes in materials, geometry, or configuration. The latter makes the certification task even more complex.

There are several difficulties associated with FBO testing. Firstly, it can be dangerous to intentionally damage an aircraft engine to reproduce a catastrophic event. Secondly, the testing is very expensive, making it infeasible to test every engine design under all possible scenarios. Another fact to consider is that there can be significant variability in the types of damage caused by FBO events, making it difficult to create a realistic emulation of every conceivable case. Furthermore, it can be challenging to reproduce exactly the same damage that occurred in an actual FBO event in a test environment, making it difficult to assess the effectiveness of design changes or maintenance procedures. Lastly, certification agencies like FAA or EASA have strict regulations governing engine testing, which can be difficult to navigate.

Figure 1.4: Rolls Royce Test Rig installation for the UltraFan [44].

Despite testing for FBO events provides valuable information for improving engine design and maintenance procedures, it is indeed a complex process that requires careful planning, execution, and analysis to ensure that it is safe, cost-effective and accurate. In this line, numerical simulation can greatly reduce the cost and time required for industrial procedures. A common practice is first to create a comprehensive high-fidelity model to capture the structural loads resulting from blade loss. The model includes the time-dependent trajectory of the released blade with the containment structure, using solvers like LS-DYNA [10] explicit nonlinear transient FEA approach, which has been proven to be robust. There has been extensive demonstration of good correlation between LS-DYNA results with test rig data [54]. After this first analysis of the impact per se, a consecutive analysis of the transmission of forces to the other components is usually performed by means of an implicit FEA solver[2].

To increase the analysis capabilities and confidence, organizations and companies are collaborating to develop and validate new tools with test data [50]. The current trend in the aerospace industry is to use numerical analysis where appropriate in order to reduce study cases, uncertainties, and cost during the experimental campaign. However, there is currently no industry-wide standard analytical modeling procedure to simulate FBO. Thus, each engine manufacturer must demonstrate their ability to perform such analysis.

Finally, it should be noted that this section only provides a general overview of current techniques for a better understanding of the following text. The state of the art of various more detailed aspects of the strategies employed today are mentioned throughout this document as part of the justification for the use of some of them.

Industry challenges

Accurately modeling the interactions between fan blades, engine components, and surrounding structures during a blade-out event is a major challenge. The dynamic and nonlinear structural coupling and post-containment unbalance can make it difficult to predict system behavior under various operating conditions. Additionally, debris released during a blade-out event can further damage the engine and surrounding structures, adding complexity to the simulation and modeling process.

On the other hand, there are different perspectives to design the fan case architecture: the hard-wall and soft-wall containment[3]. During this project, emphasis will be placed on the hard-wall containment design. In this case, the containment structure is composed of a metal ring with a sufficient thickness to contain the blade inside the engine. As for the second, it is built by a thinner

[2]Section 2.3 contains more extended information about this topic

[3]The different containment designs are explained in Section 2.1 in more detail.

metal ring wrapped by a composite material with high fracture toughness, such as Kevlar, whose objective is to trap and dissipate the blade energy through its pronounced deformation.

The phenomenon's intrinsic complexity results from a combination of large deformations, contact interactions between different elements, elasto-plastic material behavior, progressive material failure, and fragmentation under high strain rates. Furthermore, in the case of soft-wall containment, interaction of wrap/casing and material response of fabric wrap also adds to the complexity.

Obtaining accurate and reliable data to inform the simulation models is also a challenge. This includes data on the material properties of the fan blades, behavior of the engine components, and surrounding structures under different loading conditions, which may not be readily available. In the same sense, the scale and complexity of high-fidelity simulations that capture the full range of interactions and behaviors required to accurately model FBO events can be computationally expensive and resource-intensive, limiting their regular use and sensitivity analysis on different design and operating conditions. Lastly, performing explicit simulations without encountering numerical instability can also be challenging.

Therefore, significant research is necessary to overcome numerical simulation difficulties. Standardization and validation of simulation models are needed to ensure consistency in modeling approaches and assumptions and validate the accuracy and reliability of the results against real-world data. In this line, and understanding the size of the problem under consideration, this project proposes a small contribution to the whole wide development needed for the accurate numerical modeling of the FBO.

1.2 Motivation and Objectives

The objective of this project is to develop a FE model in LS-DYNA that can replicate the primary physical phenomena associated to the FBO event such as the release of the blade or the interaction between the blade and other components like the fan case. The model should be able to predict the loads and deformations on both the fan case and the released blade, thus providing a framework for designing its thickness and overall dimensioning.

The design of the model should be optimized to achieve a minimum weight configuration that offers sufficient containment resistance while holding structural integrity, e.g. the metal ring does not collapse, which entails reducing the thickness of the fan case. In consequence, the model must have sufficient flexibility for modification to allow for changes in both the containment configuration and the type of blades used.

Additionally, the project aims to provide GKN Aerospace with an initial understanding of the design requirements to withstand the resulting loads along with other relevant data for the study of the subsequent instantaneous unbalance of the rest of the rotating and adjacent components.

1.2.1 EleFanT project

GKN Aerospace's EleFanT project [11], which stands for **Ele**ctric **Fan T**hruster, is an initiative aimed at developing more efficient and environmentally-friendly aircraft engines. This project is a collaboration between GKN Aerospace and KTH - Royal Institute of Technology. It is partly funded by the Swedish Energy Agency, which supports research and innovation in various fields. EleFanT is part of a broader trend in the aviation industry towards more sustainable and efficient aircraft engines, paving the way to electric aviation for small regional aircraft, which targets net zero emissions by 2050 [30]. The development of new technologies and materials is crucial to achieving this goal, and initiatives like this one are an important step towards a more sustainable future for air travel.

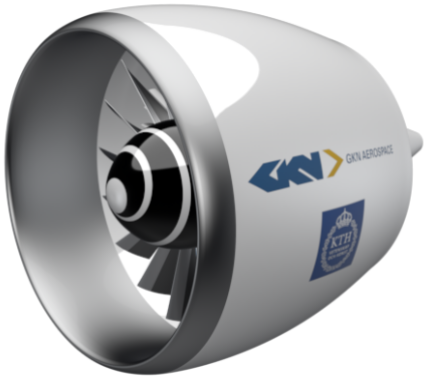

Figure 1.5: Electric Fan Thruster (EleFanT project) by GKN Aerospace [11].

The project focuses on the development of electric propellers for smaller regional aircraft, powered by batteries, hydrogen fuel cells or hybrid propulsion solutions, reducing dependency on fossil fuels and minimizing operational costs [11]. The project also aims at integrating advanced technologies, such as lightweight materials and innovative aerodynamic designs, to further improve the engine's and overall system performance. This new technology is based on a ducted fan, shown in Fig. 1.5, which enhances static thrust and efficiency, reduces perceived noise, and improves safety both on the ground and in flight, also providing installation advantages. Electric aircraft systems require less maintenance and enable turbines in hybrid-electric systems to constantly run at the optimal operating point, leading to less wear and tear, longer operation cycles, and reduced cost of ownership.

1.2.2 Scope of research

Due to the limited time frame of the project, which is around five months, the research objectives have been constrained within certain boundaries. To ensure the workload is manageable and the tasks are completed within the specified time frame, only the first phase of the FBO event is studied here. The initial phase focuses on the analysis that involves the high-speed impact of the released blade against the other blades and its subsequent radial containment by the fan case. Therefore, the built explicit model does not predict the transferring of the loads to the rest of the components, but only the loads applied to the fan case immediately after the FBO.

The project is only focused on the FBO phenomenon, but it could be potentially extrapolated to other regions of more conventional engines, e.g. turbine or compressor blade-off. All specific loads related to the event could be accurately estimated using FEM; however, this process would be very time-consuming, requiring a very detailed knowledge of the engine geometry, which is still subject to changes in this early stage. Therefore, a simpler model layout has been developed to estimate loads in a more general configuration environment, focusing only on certain crucial components, like the fan case and the released blade, potentially constituting a benchmark for future model improvements and design refinements.

This model is numerically validated and sensitivity studies are conducted on diverse parameters such as contact, material models, and boundary conditions definition. The numerical model and solution procedures are optimized for fast simulation and execution. Finally, the physical phenomena involved are studied, and the fan case is sized to withstand the pertinent loads.

Note on Public Domain Data usage

The utilization of Public Domain Data in academic reports has become increasingly prevalent due to its widespread accessibility and potential to enhance research efforts. When employing such data, it is crucial to comply with ethical and legal guidelines, such as appropriately acknowledging the sources and verifying that the data is indeed in the public domain. It is also necessary to consider any potential biases or limitations that may exist in the data and to address them appropriately in the report.

Since this state of the design process is very particularised for each type of engine, most companies do not share their methodologies or results for business secrecy purposes. Additionally, as the conceptual stage implies a new and very different design that the company lacks experience in, there is no relevant available data from either numerical or experimental results that could be provided.

It is important to keep this in mind as it imposes a significant limitation on the validation and

verification against the physical model. Therefore, the results presented here cannot guarantee complete reliability compared to the real model.

Finally, similar prototypes to those proposed in the literature are created aside from this project's primary objectives to validate numerical approaches, such as mesh sensitivity analyses, constitutive models or the expected order of magnitude of loads generated after impact.

Chapter 2

Methodology

This chapter presents the methodology adopted in this project in order to achieve the proposed objectives in the most efficient and rigorous manner. In addition, some theoretical concepts of the physics of the problem are also introduced in order to be able to refer to them, if necessary, in later sections.

First, in Section 2.1, an overview of the model considered and its rationale is given. This is followed in Section 2.2 by a description of the design process on which this project is based. Next, Section 2.3 discusses the state of the art and the most commonly used techniques for this type of simulation in order to establish the concrete path to be taken. Finally, Section 2.5 is a compilation of the most important theoretical concepts for the general understanding of the LS-DYNA software architecture.

2.1 Review of Design Models

This section presents the containment model to be evaluated in this project, as well as a brief conceptual explanation of its rationale and the trade-offs involved in its design. Two main models are usually used in industry, which essentially differ in the casing architecture.

As stated in previous sections, fan containment systems play a crucial role in preventing fan blade fragments from damaging aircraft components, e.g. principal hydraulic systems, or piercing the fuselage, and causing catastrophic accidents. However, there exist several design approaches to ensure safety while gaining maximum benefits in terms of costs and manufacturing. There are two types of fan containment systems: hard-wall fan containment and soft-wall fan containment. Hard-wall containment involves the use of a stiffer metal structure to contain fan blade fragments, while soft-wall containment uses a more flexible barrier, usually made of composite materials and

a thinner metallic ring. Both systems include ribs and stiffeners which enhance system stiffness and both typically have generally cylindrical geometries.

Hard-wall fan containment is the traditional method for containing debris inside the engine. It involves the use of a metal ring, which thickness is designed to withstand and deflect blade-out shrapnel so no high-energy fragments would penetrate the cowling, i.e. the outer shell of the engine. Hard-wall containment is typically used in larger aircraft and in engines with high-energy turbine stages. These systems are constructed from high-strength but ductile-enough alloys (titanium, aerospace grade aluminum or high-ductility steel [51]), which arrest the kinetic energy of the blade through plastic deformation, and possibly exhibiting a controlled amount of cracking. While hard-wall fan containment is a proven technology, it has some disadvantages such as the addition of significant weight to the aircraft, since the fan case is one of the heaviest parts of the engine. Some other practices also suggest the implementation of hollowed structured material systems in order to reduce weight while maintaining the aerodynamically enhanced architecture of this containment structure, e.g. *Rolls Royce Trent 900* [38]. Common practices in industry for hard-wall fan containment also include the use of shrouds, disks, and other components to prevent perforation. Examples of hard-wall fan containment in the aviation industry include *CFM56*, shown in Fig. 2.1, and *Pratt & Whitney PW4000* family.

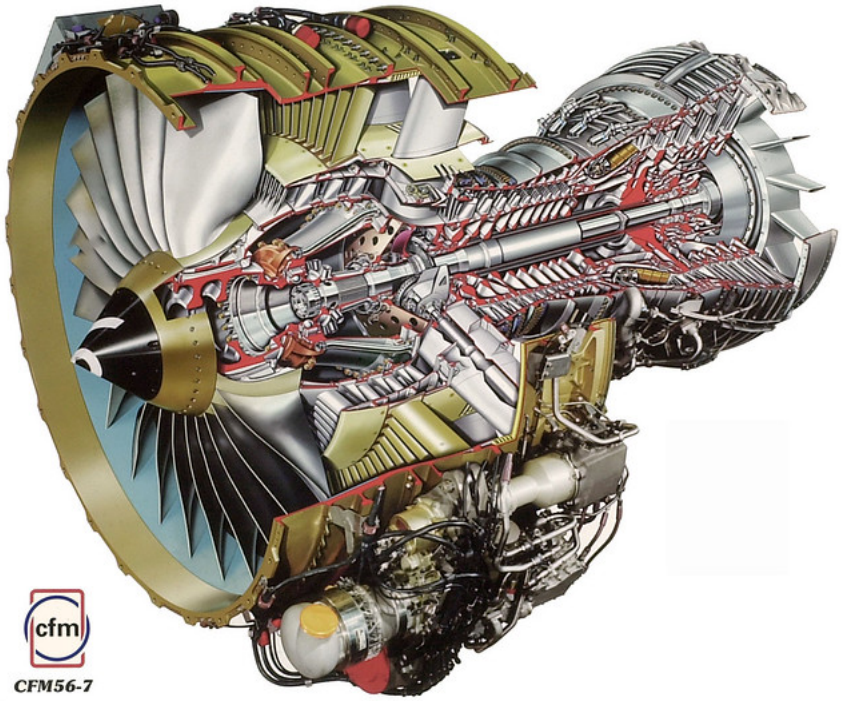

Figure 2.1: Engine CFM56-7 graphical schematic [13]. The fan case is composed by a solid metallic ring, providing a hard-wall containment architecture.

Soft-wall fan containment is a newer approach and involves the use of a more deformable

barrier to trap the fragments. This approach is typically used in smaller aircraft and engines with lower-energy turbine stages and it was developed in order to mitigate weight penalization from more traditional designs. As Fig. 2.2 shows, these systems consist of a relatively thin inner ring, usually made with some aerospace grade aluminium, surrounded by layers of dry fabric made of high-strength materials such as aramid (Kevlar). These Kevlar fabric layers are designed to dissipate the kinetic energy of the released fragments through large deformations (like a net catching a trapeze artist). Therefore, enough space must be included between the ring and the outer shell of the engine as the blade is supposed to puncture and be trapped in the flexible structure. As a consequence of including this empty space, the engine's diameter is enlarged, which can produce an increase in drag. Furthermore, these are more complex systems to design, requiring more sophisticated materials and manufacturing processes.

Figure 2.2: Engine GE90-115B soft-wall fan containment system [6]. It is composed by an inner metallic ring wrapped in Kevlar layers.

Despite acting as a detriment on the outer aerodynamic design, this arrangement comes with the advantage of modifying the sequence of events during the FBO. In this case, the released blade is captured away from the main flow path, which avoids fragmentation and further damage to neighboring blades. These lighter weight technologies have become a very common practice in industry in engines such as *Trent700*, *PW4084* and *GE90* [21].

Apart from assessing the relative weight-savings that they could potentially provide, other factors such as collateral damage associated with the impact must also be evaluated. While the stiffer case causes a domino effect of blade failures due to interference with the path of the broken

blade, in the soft case the non-damaged blades are forced to rub on the fan case due to small clearances. The latter highlights the importance of reducing the thickness of the fan case as much as possible for the benefit of the weight, but not so much that it largely deforms as to produce derived inconveniences.

In short, this project presents a part of what would be the process of designing and evaluating the relative merits of one architecture over the other. To carry that evaluation, firstly, the hard-wall containment with metal blades is developed, as its modeling is more elementary. The objective of this first step is to create a robust and efficient prototype that serves as a benchmark for subsequent developments. The next step, which falls outside the scope of this project, would be introducing the composite blade model in order to evaluate its effect on the sizing of the hard-wall containment. The final step, also beyond the present study, would be the design of the soft-wall fan case, which includes more modeling elements such as the validation of the composite material model for the Kevlar wrap and its interaction with the metallic ring.

Composite blade

The use of composite materials in fan blades, especially carbon fiber reinforced plastics (CFRP) has gained popularity in the last two decades due to their high strength-to-weight ratio, corrosion resistance, and improved fatigue performance compared to traditional metal alloys [33]. Especially as fan or propeller blades these materials show enhanced efficiency with respect to more traditional techniques. The advantages are not only in terms of overall weight savings, but it would also produce a less severe impact in the case of fan blade off, as lighter blades contain less energy to be dissipated, resulting in a less massive containment system. However, there are also limitations to using composite blades in fans that must be considered in the case of carrying out a simulation of the event and during the interpretation of its results.

Firstly, composite materials are more susceptible to damage from impact, such as bird strikes or debris ingestion, which could be a potential reason for a fan blade-off. While metal blades may dent or bend under these conditions due to their higher ductility, composite blades can suffer significant damage that may compromise their structural integrity. Additionally, composite materials can degrade over time due to exposure to heat, moisture, and UV radiation. This can result in a loss of strength and stiffness, which may not be detectable through visual inspection alone. On top of that, the manufacturing, testing and maintenance of composite blades require specialized skills and equipment, which can be costly and highly complex. Finally, the inspection and repair of composite blades also require specialized training and equipment, which may not be readily available at all airports or maintenance facilities.

2.2 Design Process

This section presents the scheme of work followed throughout this MSc thesis. The different steps taken for each phase of the study have been considered necessary and essential in order to achieve the objectives proposed in previous sections.

It should be noted that, prior to the development of this process, research and understanding of both the operation of the LS-DYNA solver and the different most common techniques in the state of the art have been carried out. This has also entailed the collection and application of recommendations on the use of certain numerical parameters provided by the software developers [16].

Finally, since the complete model is composed of different parts that are subjected to different forces and boundary conditions, each task mentions to which part or set of components it applies. Although some of the concepts are clarified and expanded in Chapters 3 and 4, in order to facilitate the reading in the proposed order, an example of the complete model is attached in Fig. 2.3, showing the different parts discussed in this section.

2.2.1 Preliminary model

This preliminary stage of the FBO study is simply about familiarizing oneself with the LS-DYNA environment, the physics of the process, and the various necessary concepts to carry out a more in-depth analysis. Despite not being one of the stages of the design process per se, it has been an important task as it has refined the definition of certain aspects of the simulation and debugged faults in the code that runs the explicit and implicit solvers of LS-DYNA[1].

[1]The inner working of LS-DYNA package is further explained in Section 2.5.

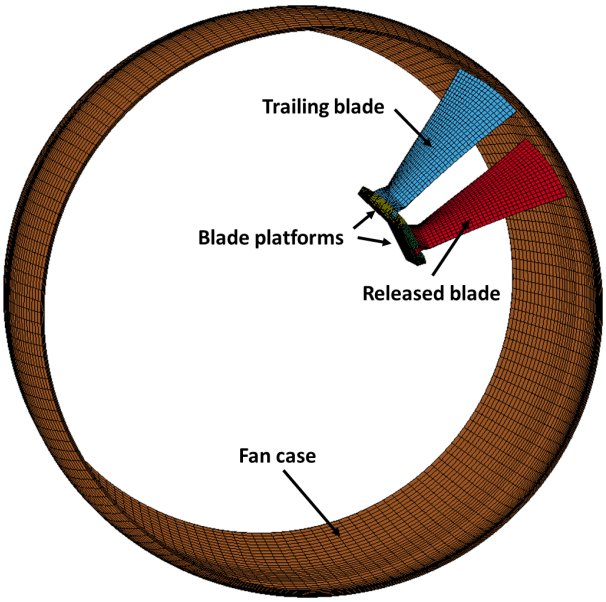

Figure 2.3: Components and disposition of the hard-wall containment preliminary model.

To shed more light on the subject, some of these aspects are the setup of boundary conditions, such as the generation of initial velocity in the blades and platforms, or the way to simulate the fracture and release of the considered blade. Additionally, embedded in this same process is the instruction in the *ICEM CFD* software of the ANSYS package [1] used to create meshes using hexahedral elements for complex geometries like the blades or platforms. This latter step has resulted in a process that has significantly improved the quality of the simulations and, in some cases, allowed them to run when the quality of the elements was so poor that the simulation crashed. The reason for using this second software for meshing is that both LS-DYNA and the *ANSYS Mechanical* environment in Workbench only provide simple automated *meshers* which are not sufficiently sophisticated to create structured meshes in more complex geometries.

Therefore, the testing of this model, based on the hard-wall containment layout, and its derivative versions due to minor modifications and improvements, is not a thorough analysis based on the parametric study of the different algorithms involved in the numerical model. Its ultimate goal has been to build a schematic process for the construction of the final model and explore the couplings and compatibilities between the different environments used, including *ANSYS Mechanical*, *ICEM CFD*, *ANSYS Workbench LS-DYNA*, and *LS-Prepost* (the LS-DYNA solver interface independent of Workbench).

Summarizing, this model has not been verified or validated in any way beyond qualitatively checking that the simulation represents the desired physics of the process and does not exhibit any numerical errors or instabilities. For this reason, it is not considered pertinent to provide further

details on the different phases of constructing this model and instead, the following sections expand further on those that have been treated in greater detail.

2.2.2 Blades

It is worth noting that in this section, only the design steps are mentioned and described. The detailed explanation and presentation of relevant results of the final model are provided in Chapters 3 and 4.

Modal analysis

First and foremost, the analysis focuses primarily on the two considered blades. Furthermore, given the complexity of their geometry and, consequently, the greater difficulty in obtaining a sufficiently suitable mesh for the target simulation type, it is important to verify its quality through additional steps.

Therefore, a modal analysis is first performed to verify how faithfully the mesh is able to represent the blade's geometry and inertial characteristics. This is carried out in two different softwares, LS-DYNA with implicit integration scheme in double precision and ANSYS Mechanical in Workbench, to double-check its correct completion. Note that similarly to the preliminary model, no results of these simulations are shown in this report, since they are not strictly necessary for its main objectives.

Stress initialization and blade explicit rotation

The next step involves initializing stresses on the blades due to being subjected to a constant centrifugal force during rotation. When in this state, the blades undergo a phenomenon called dynamic stiffening, during which their geometry slightly changes. Typically, the stresses reached during this phase are elastic, and the displacements are small, resulting in a new state referred to as blade "pre-stress" or "pre-load".

When these characteristics are present in an explicit simulation, it is convenient to induce steady-state pre-loads through implicit simulation prior to transient dynamic analysis, thus ensuring solution stability and shortening final simulation time. Despite finding different methods to accomplish this in the LS-DYNA environment, the one that provides greater control over the results without excessively penalizing the effort and time required to set up the simulation has been chosen. This is the so-called **two-step blade pre-load** analysis procedure.

The alternative is known as "dynamic relaxation". This method consists of a single step and essentially involves including both an implicit pre-load and an explicit blade rotation in the same

simulation. In simpler terms, this method is based on introducing a strongly damped transient solution at the beginning of the simulation through the use of the so-called dynamic relaxation (DR) factor. The objective of this technique is to damp out radial and torsional vibration due to rapid deployment of rotation. Once the solution is considered converged, i.e. the kinetic energy due to nodal vibrations has been sufficiently reduced, the solution automatically proceeds to the explicit phase. In Fig. 2.4, it is schematically shown how during the dynamic relaxation phase, a ramp load is applied and kept constant until convergence. Once converged, the transient phase begins, during which the centrifugal load is maintained constant.

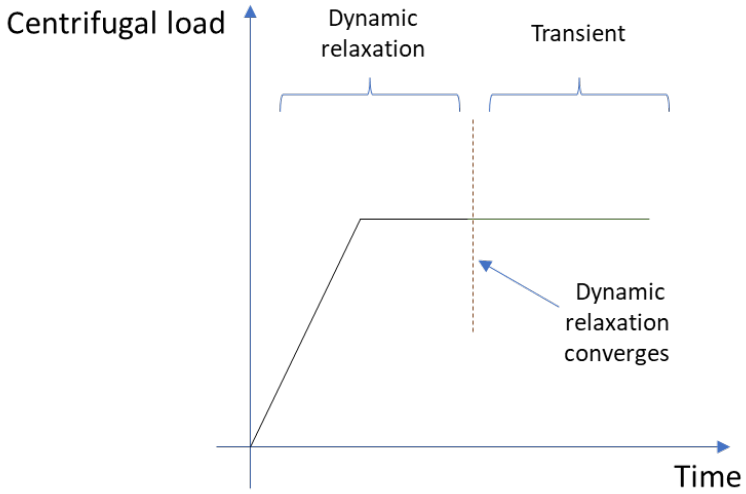

Figure 2.4: Simplified diagram of how dynamic relaxation works in LS-DYNA.

However, the two-step blade pre-load analysis method has been ultimately chosen as it promises to be the most robust according to the guidelines provided by the LS-DYNA developers and experienced users. It should be noted that this step is applied to both blades simultaneously. It involves, firstly, applying the blade pre-load using the implicit solver option in LS-DYNA to simulate the centrifugal force on the blade, which clamped condition is applied by constraining the translation and rotation of the nodes at the zones in contact with the platform. These areas are shown in Fig. 2.5, and they are the same for both blades.

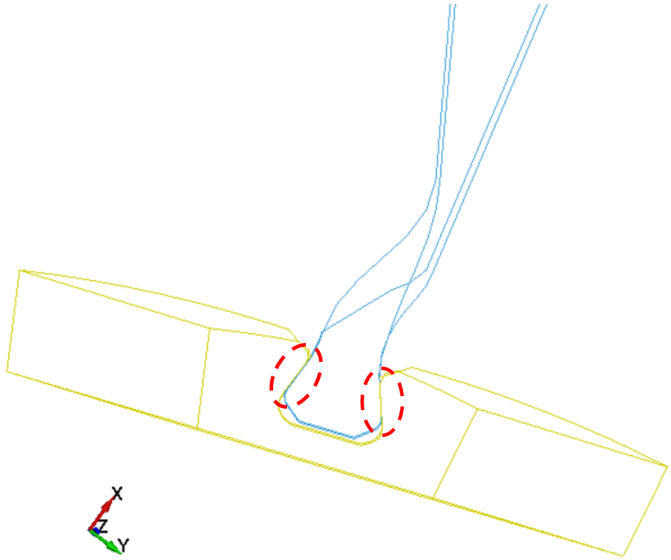

Figure 2.5: Blade-to-platform contact (dashed-red ellipses).

From this first simulation, an output file is obtained that captures the description of the deformed geometry, stresses, and strains. This file is then used to start an explicit simulation in which the blade is rotated for a complete revolution to verify the stability of the expected results. This is done by studying the evolution of the centrifugal force and the stresses of the elements in an arbitrary section of the blade, which should remain invariant during the rotation as a rigid body. Fig. 2.6 provides a graphical aid to better understand the workflow followed and just described.

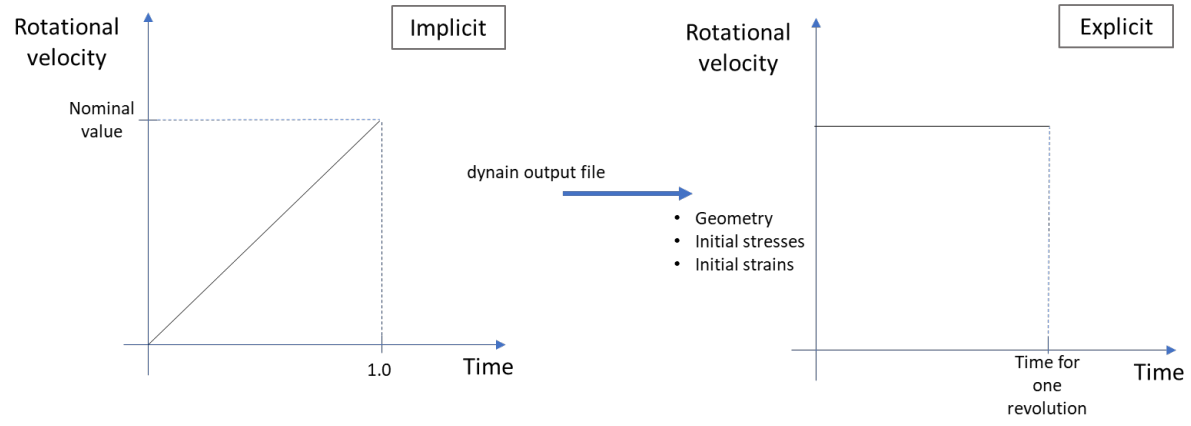

Figure 2.6: Simplified diagrams of the two-step pre-load analysis procedure adopted.

Finally, this last simulation is also used to check other aspects of the numerical solution such as the energy balance or the physical behavior of the blades.

2.2.3 Hard-wall containment model

The next step in the process is the construction of the complete model. Since the fan case is composed of a single uniform material, no additional steps are required other than assembling all the parts and defining the boundary conditions and other parameters.

Within this process, the fan case is meshed using *ANSYS Mechanical* in *Workbench*, being the automatic mesher capable of creating a quality mesh that is sufficiently modifiable for this simple cylindrical geometry. Additionally, the meshes of the platforms to which the blades are attached are also added. In this case, *ICEM CFD* is used. Their configuration remains unchanged throughout all the simulations as they are considered rigid and their contribution is purely inertial.

Afterwards, the comparison is conducted by evaluating the obtained results from the simulations of each model version. This includes examining the stability of the solutions, the agreement with expected behavior, and the consistency of the results across different scenarios or loading conditions. Based on this analysis and comparison, the most suitable model version is selected, taking into account the desired objectives, accuracy, computational efficiency, and any other specific criteria relevant to the containment design.

This iterative process of analysis, comparison, and selection ensures that the chosen model version provides the optimal numerical model for the containment design.

2.2.4 Summary

The following is a recapitulation of the established design process:

1. **Familiarization and understanding of the LS-DYNA environment, process physics, and necessary concepts.**
    - Configuration of boundary conditions and simulation of blade rotation.
    - Qualitative verification of the simulation and debugging of LS-DYNA code.
    - Exploration of the couplings and compatibilities among the different utilized environments.
2. **Detailed analysis of the construction and design phases of the model.**

    Blades
    - Validation of the chosen construction approach through modal analysis.
    - Initialization of stresses and deformations on the blades using implicit simulation.

- Generation of files containing deformed geometry and stresses for use in explicit simulation.
- Explicit simulation of blade rotation to verify stability and consistency of results.

Hard-wall containment model

- Meshing of the fan case.
- Incorporation of pre-stressed blades and platforms into the complete model.
- Setting up simulation conditions and launching the simulation in LS-Prepost.

3. **Analysis of results and comparison of different versions of the models.**
   - Selection of the optimal model based on criteria such as numerical efficiency, accuracy, and containment design.

It is important to note that this recapitulation of the design process offers a general overview, but each stage may involve multiple additional steps and considerations that are addressed in detail during the project development.

2.3 Current Trends in Modeling

The following is a generic presentation of current techniques and methodologies for carrying out airworthiness verification and optimal design for an FBO event. As mentioned above, the classical technique for engine certification used to be experimental. However, the facilities and processes to carry it out are highly complex and time-consuming, leading to high costs. In addition, it is difficult to obtain the measurement capability of all the desired variables as well as an automated variation of different parameters that numerical simulation provides. For example, by simulation it is possible to capture more details such as energy transfer and dissipation between the different parts involved. Additionally, FBO is a highly destructive test and achieving an acceptable repeatability rate requires a great deal of effort.

Nevertheless, many developments in the fan containment and design analysis have been done in an internal level of the companies, being highly propietary and confidential, therefore not being a large amount of public domain information on the topic. The firsts major recorded efforts to study hard-body impact on engines started around late 70s. However, it was not until the late 1980s that a finite element model was developed for accurate containment design. Until then, soft-wall containment was designed with multiple layers of Kevlar to ensure debris confinement [54]. Since then, numerous advances have been made with respect to the modeling of Kevlar 49 [51] or the

implementation of hybrid alternatives that allow the introduction of explicit and implicit analyses in the same simulation [27]. These developments contributed to the acceptance by aviation safety and certification agencies of airworthiness demonstration using numerical models in the absence of test rig data [24].

Thus, given the increasing fidelity of the software tools used, industry has tended to use this type of technique to certify its components. As already mentioned, during FBO it is not only the highly energetic impact and its direct repercussions on the structural integrity of other components that are at stake, but also the post-containment vibrations that could potentially cause further damage to the engine and its attachments. Mitigation measures for this part of the event are tremendously important to ensure the structural integrity of the engine and safety of the passengers. These out-of-balance forces can highly damage the engine's structure, as it was registered in the "uncontained" FBO failure of the CFM56-7 of the Southwest Airlines' Flight 3472 in 2016 with the failure of the inlet structure [13].

For these reasons, an industry-wide practice is to divide the event into two phases according to the characteristics of the physical phenomena involved:

In the first case, a high-speed impact occurs, resulting in the transformation of kinetic energy from the released blade into deformation energy or the dissipation of this energy through frictional interaction and damage. All these phenomena occur in only a few fractions of a second, so the analysis must be adapted to such dynamicity. The solution for this is to carry out an explicit transient simulation. In this stage, initial conditions, material properties, and other relevant parameters are input. The simulation produces results such as stress state and deformations in the impacted structure.

The explicit analysis typically includes fewer components in the prototype. However, each of them are much more detailed, for example in terms of mesh refinement, geometry or complexity of the numerical model of the materials. These components are generally those directly involved in the impact: the containment system, the blades and platforms and, occasionally, also the shaft. An example of this can be seen in Fig. 2.7a, a case study conducted by the Aerospace Working Group and collected in an LS-DYNA repository [12].

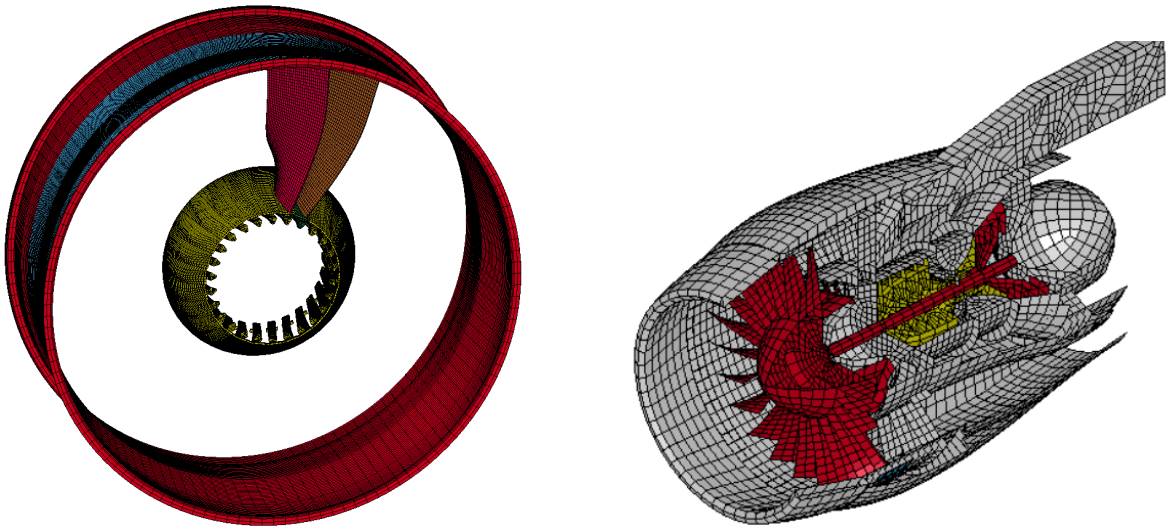

(a) (b)

Figure 2.7: Explicit [12] (a) and implicit [29] (b) models in LS-DYNA.

The results obtained from the explicit simulation are then transferred to another software or analysis tool, e.g. *NASTRAN*. In this stage, a more global implicit simulation is conducted. This simulation may involve a larger model, allowing for complex contacts and vibrations between components, or a more in-depth analysis of the transferring of the loads and deformations to the components not directly involved in the impact event. Fig. 2.7b shows how an implicit model consists of many more engine components but with a much coarser and simpler mesh.

In summary, the described process involves conducting an initial explicit simulation of the impact to obtain detailed results on the stress state and being able to extract conclusions regarding the containment capability of the case. These results are then transferred to an implicit software for further analysis and calculation of loads on a larger model. Despite being the most extended practice in industry, it is important to note that the specifics and exact flow of this process may vary depending on the tools and methods used in each case.

2.4 Material Modeling

Selecting the appropriate material model is crucial to accurately simulate the response of structures subjected to high-velocity impacts. The chosen model should correctly predict deformation over time and account for damage. When working with aluminum alloys and other metals, it is usually important to also consider the influence of strain rate, as they are commonly highly sensitive to it.

There are various approaches that can be taken for this, depending on the availability of

material data parameters or the degree of rigour with which the event is to be simulated. Sources describing true stress - true strain curves for a variety of aluminium alloys for aeronautical use can be found in the literature [43].

Since these materials are used in the model, an extensive search has been carried out to determine which mathematical models included in LS-DYNA provide the most reliable results for the FBO event, while being feasible in terms of available data. Some of these sources are later used in the construction of the models.

2.4.1 Numerical material models

First, a review of current modeling trends of the metallic materials used is presented. In addition, for each of them, the reasons for their selection/exclusion in this project are highlighted.

These materials are Al7075-T6 for the blades and Al2024-T3 for the fan case. Note that the platforms are considered rigid. The methodology employed in constructing these material models is founded on a fusion of experimental research methodologies and 3D computer simulation technologies. By utilizing software packages, one can simulate the material behavior under dynamic loading conditions. To effectively carry this out, a profound comprehension of the intricate material behavior models is necessary. These are dependent on a variety of parameters and conditions such as the initial stress state, the strain rate, and the temperature. To equip the constitutive models and fracture criteria with requisite parameters and constants, one must possess an extensive database on the dynamic properties of the considered materials.

Two trends have been observed, particularly: use of the Johnson-Cook constitutive model or the definition of the elasto-plastic material constitutive relation through a piece-wise linear function plus the introduction of the strain-rate influence.

Johnson-Cook

The Johnson-Cook constitutive model (1983) is a phenomenological model, i.e. it is based on experimental observations at the macroscopic level, that reproduces non-linear material behavior observed in impact and penetration of metals. It has been found that the determination of the parameters for this model, which are necessary to describe the behaviour in the severe conditions encountered during high-speed impacts, can be challenging. Therefore, a lot of work has been done to combine experimental tests and numerical models in order to provide a set of parameters adapted to the LS-DYNA package for a variety of alloys [31, 34, 22].

Despite its extensive usage in the state of the art, the Johnson-Cook model has been excluded from this master's thesis work as it has been deemed that the identification of the proper material

parameters falls beyond the established project limits. Employing and validating this model would require a more meticulous effort that exceeds the available time frame. However, the reader is strongly encouraged to consider its future incorporation for more advanced versions of the proposed model. More information about this material model can be found in Annex A.

Piecewise Linear Plasticity

The second material model, which is also frequently used in the literature [17, 19, 57, 40, 52], is a robust method known in the LS-DYNA jargon as Piecewise Linear Isotropic Plasticity. In this environment this material is identified as *MAT_024 or *PLP*. This model offers a multi-linear strain-stress behavior with isotropic hardening along with the optional addition of strain rate effects, and a plastic-strain-based failure criterion. It has been extensively tested and is considered one of the most straightforward yet comprehensive material models for accurately representing the real behavior of metals. Additionally, it is computationally optimized and available for a variety of element types, making it less prone to present issues in simulations.

The construction of this model can be approached through different methods. In addition to the basic material parameters such as density (ρ), Poisson's ratio (ν), Young's modulus (E), and yield strength (σ_y), a fifth parameter called the tangent modulus (E_T) can be introduced. With this method, a bilinear constitutive relationship is being constructed, consisting of a first slope defined by E and a second line that starts at the yield point and has a lower slope equivalent to E_T.

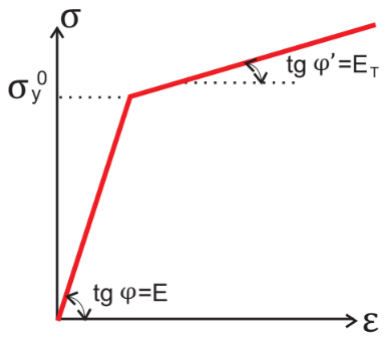

$$\frac{E}{E_T} >> 1$$

$$E_T = \frac{d\sigma_y}{d\varepsilon}$$

Figure 2.8: Idealization of real behavior: elastic-plastic linear hardening definition using the tangent modulus [47].

Notwithstanding its simplicity, given the search for a better approximation of the constitutive model, the alternative way has been chosen. In this approach, the piece-wise linear curve of effective true stress vs. effective true plastic strain is introduced in eight points, from the yield stress to the failure point.

With regard to strain-rate sensitivity, this model allows for the introduction of additional data describing its strain-rate behavior. This is often used in simulations of high-speed impact

and explosive events, where the strain rate is extremely high and the material response is highly nonlinear. Ballistic tests at Glenn Research Center suggest that very high strain rates can occur in this type of event [46], occasionally even reaching up to several thousands of s^{-1} [20]. However, since this feature is not utilized in this work, the discussion regarding this aspect can be found in Appendix B. The reasons for discarding this effect are explained in Section 3.1.5.

In essence, a PLP model defined by eight points in the plastic region is selected. Despite being considered the optimal material model in this case, striking the trade-off between capabilities and simplicity, it is important to emphasize that the models represented by these equations are still approximations. Therefore, there is a possibility that not all materials are faithfully described across the entire range of events. LS-DYNA also offers the possibility of implementing additional material models, which can be highly beneficial for the later stages of more advanced and in-depth analyses.

Finally, it is important to once again highlight the lack of experimental results for the tested model, which limits the validation and rigor of the numerical model to some extent. Consequently, this work acknowledges this limitation and strives to construct the most accurate model possible through reasoning and qualitative evaluation. Furthermore, several future lines of work are proposed for different conditions when available, addressing this issue.

2.5 Theoretical Background

In this section, some of the most relevant mathematical concepts and formulations for the problem under consideration are presented. The aim of this is to provide some notions of the mechanics of continuous media and show in general terms how LS-DYNA is constructed internally.

Therefore, the focus is mainly on the description of the equations governing continuous nonlinear mechanics and the treatment of their discretized form in order to solve them by means of the FEM. More specifically, the kinematics of bodies, the fundamental conservation laws and, finally, the equations of motion are discussed. This is followed by a review of the main time integration schemes and their respective characteristics and uses. Ultimately, some key concepts about other numerical model algorithms such as hourglass mode control and the different contact formulations and their application in LS-DYNA are added.

It should be noted that all equations and theoretical concepts have been obtained from theoretical material taught in previous courses [47], relevant books in non-linear mechanics [18] or the theoretical manual provided by LS-DYNA [26].

2.5.1 Continuum mechanics and kinematics

Continuum mechanics is the study of the deformation of bodies under applied force that are assumed to be continuous, i.e., materials that can be modeled by a set of continuous and smooth functions. Their behavior is described by their deformation and stress, and their equations of motion result from setting the force balance of the system. Note that throughout this project, and for the sake of simplicity, all materials are considered continuous and homogeneous.

Kinematics is the study of the motion of a continuous material body without considering the causes of that motion, i.e. the forces. It is concerned with the description of its deformation and motion in terms of its position, velocity, and acceleration at different points in time.

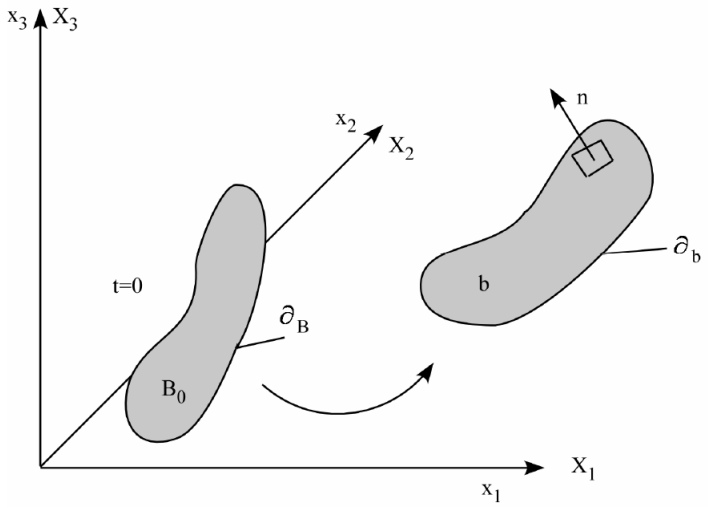

Figure 2.9: Reference configuration and an arbitrary current deformed configuration of a body according to LS-DYNA formulation [26].

Thus, this branch aims to describe the time-dependent transformation of a body from the reference to the current configuration. As can be seen in Fig. 2.9, the position of the particles in reference state (B_0) at $t = 0$ is denoted as X_α, with $\alpha = 1, 2, 3$, while the current configuration after finite deformation at time t (b) is described by the x_i-coordinate set, with $i = 1, 2, 3$.

The modeling approach in LS-DYNA for crash and impact simulations is the Lagrangian formulation, i.e. a material-based reference frame, where the current configuration, i.e. the set of positions in body space, can be expressed as a function of the reference frame for each instant of time (Eq. 2.1). Therefore, in an all-Lagrangian approach, the mass of material within each element is invariant and both elements and materials translate, rotate and deform together.

$$x_i = x_i(X_\alpha, t) \tag{2.1}$$

This, together with initial conditions, e.g. position or velocity at $t = 0$, describe the time-dependent deformation of a body.

2.5.2 Conservation laws

The conservation laws are the fundamental physical principles that govern the behavior of materials. Although some components of the simulations, i.e. the platforms, are considered rigid, the following equations apply to the deformable bodies, as they are the ones being analyzed. These mathematical constructs ensure that certain properties such as mass, momentum, and energy are conserved during any physical phenomenon.

The first law is the **conservation of mass**. This principle states that the mass of a closed system remains constant during a physical process. It is described as follows:

$$\rho J = \rho_0, \tag{2.2}$$

where ρ is the current density, ρ_0 the density at the reference and J is the Jacobian, which is described by the determinant of the deformation gradient matrix $F_{i\alpha}$ (Eq. 2.3), and it is a measure of the change in volume.

$$F_{i\alpha} = \frac{\partial x_i}{\partial X_\alpha} \tag{2.3}$$

The next law is the **conservation of linear momentum**. This law states that the momentum, which is a measure of an object's motion if no external force is applied, and is defined as the product of mass and velocity, is conserved during the deformation process. This implies that the derivative of stress plus body forces are equal to inertial forces, as can be seen in Eq. 2.4. Is the solution of this equation what is sought to solve the time-dependent deformation of the considered body.

$$\sigma_{ij,j} + \rho f_i = \rho \ddot{x}_i, \tag{2.4}$$

where σ_{ij} are the components of the Cauchy stress tensor and $\sigma_{ij,j}$ the spatial derivation of such tensor, f_i is the body force density, and $\ddot{x}_i$ is the acceleration. This equation must satisfy the traction ($t_i(t)$) and displacement ($D_i(t)$) boundary conditions, apart from the contact discontinuity condition. These three conditions are gathered, respectively, in equations (2.5), (2.6) and (2.7). In these equations n_i is a unit outward normal to a boundary element.

$$\sigma_{ij} n_i = t_i(t), \tag{2.5}$$

$$x_i(X_\alpha, t) = D_i(t), \tag{2.6}$$

$$(\sigma_{ij}^{+} - \sigma_{ij}^{-}) n_i = 0. \tag{2.7}$$

Finally, the **conservation of energy** law, also referred to as the *first law of thermodynamics*, ensures that the amount of total energy at the beginning and end of the process remains the same. This law states that energy can neither be created nor destroyed, but converted from one form of energy to the other. This relationship is captured in Eq. 2.8.

$$\mathcal{Q} + \mathcal{W} = \dot{\mathcal{K}} + \dot{\mathcal{U}} \tag{2.8}$$

This equation is integrated over time to be used as an equation of state and to evaluate important aspects of the simulation such as global energy balance.

2.5.3 Equations of motion

Nonlinear mechanics equations describe the behavior of a body under certain external forces, taking into account non-linearities arising from the constitutive law of the material or the magnitude of the displacements. The second-order differential equation that relates displacements, velocities, and accelerations to material properties and external loads is Eq. 2.4. Since it is not possible to analytically solve this equation, numerical methods such as FEM must be used to obtain an approximation of the displacements for each time instant. This is done by superimposing a mesh of interconnected finite elements through nodes, which are the points in the solid where the position is tracked over time. Depending essentially on the geometry and expected behavior of each solid, a suitable formulation is used for the elements of this mesh, i.e., solid[2], shell, beam...

Eq. 2.9 describes the balance of the inertial, dissipative and internal forces (left hand side), respectively, relate to external forces (right hand side). This equation is a result of discretizing Eq. 2.4 using FEM and combining it with a constitutive model. Therefore, through spatial semi-discretization, the spatial field **x** and its time-derivatives are defined by approximating them through nodal values of displacement u, velocity $\dot{u}$, and acceleration $\ddot{u}$. For the present case, as LS-DYNA is accounting for a non-linear formulation, the internal forces are a non linear function of the displacements (u).

[2]LS-DYNA encompasses all available 3D element formulations under this name.

$$m\ddot{u} + c\dot{u} + f_{int}(u) = p(t) \tag{2.9}$$

To solve for the displacements in this new system of equations, iterative numerical methods like Newton-Raphson are used. Additionally, when dealing with a problem involving large displacements and non-linearities, it is necessary to track the temporal evolution of these displacements throughout the entire simulation. This is achieved through temporal discretization of Eq. 2.9 using the so-called time steps. This creates a system of non-linear equations whose temporal evolution is integrated to determine the displacements at each time instant, which are determined by the discretization. There are two main methods for this, which are described in Section 2.5.4.

2.5.4 Time integration

This section discusses the time integration schemes used in computational mechanics of solids and how they are approached in LS-DYNA. It highlights the significance of the integration time step size, Δt, and how it determines the accuracy, efficiency and stability of results. The equations involved in the finite element method and the need for an appropriate integration strategy are presented.

Integration schemes are divided into two types, implicit and explicit, depending on the information used at each time step.

Explicit integration

For the explicit integration LS-DYNA uses the *Central Difference Method*, in which only information at time t_n is used. This scheme is based on the inversion of the mass matrix to solve for acceleration at a given time, as indicated in Eq. 2.10. It is worth noting that this equation is analogous to Eq. 2.9, but disregarding the dissipative forces, adding hourglass control non-physical forces and particularizing at a time t_n. In this expression, $\ddot{u}$ is the acceleration vector at that time instant, **m** is the diagonal mass matrix, **p** accounts for external loads and **H** is the hourglass resistance, if any. This last term arises as a result of the so-called "Hourglass Control". In general terms, this is an algorithm created to counteract and control the modes associated with spurious zero deformation energy, i.e., hourglassing modes, which arise from the use of underintegrated elements. This method is further discussed in Section 2.5.6.

$$\ddot{u}(t_n) = m^{-1}\left(p(t_n) - f_{int}(u(t_n)) + H(t_n)\right) \tag{2.10}$$

Once nodal accelerations are obtained, the global nodal velocity vector **v** is evaluated at an

intermediate time step $\Delta t^{n+1/2}$ (Eq. 2.11), from which the global nodal displacement vector for the desired time step u^{n+1} is obtained (Eq. 2.12).

$$v^{n+1/2} = v^{n-1/2} + a^n \Delta t^n, \tag{2.11}$$

$$u^{n+1} = u^n + v^{n+1/2} \Delta t^{n+1/2}, \tag{2.12}$$

where

$$\Delta t^{n+1/2} = \frac{\Delta t^n + \Delta t^{n+1}}{2}, \tag{2.13}$$

is the intermediate time step. Once the system is solved for displacements, the geometry is updated by adding them to the initial reference state. This is a relatively straightforward process that does not require internal iterations at each time step to achieve convergence.

However, one of the peculiarities of this method is that it is conditionally stable, and this stability is essentially subjected to the size of the time step. The maximum time step size (Δt_{crit}) that ensures solution stability is limited by the Courant-Friedrichs-Lewy (CFL) condition (1928), which establishes a relationship between the time step size and the element size. Eq. 2.14 represents this expression for the three-dimensional case assuming a uniform discretization, where v_i is the velocity, Δx_i the element size, and typically, $C_{max} = 1$ for explicit solvers.

$$C = \Delta t \left(\sum_{i=1}^{3} \frac{v_i}{\Delta x_i} \right) \leq C_{max} \tag{2.14}$$

This condition physically translates into the algorithm's ability to compute the passage of a pressure wave through the element in discrete time steps of the same duration. Therefore, in order to capture this, the maximum size of these time steps must be limited by the minimum time it takes for this wave to completely cross the smallest element. Consequently, the smallest element size in the entire mesh is the one that determines the critical time step. The mathematical form of the critical time step varies depending on the type of element used, as it depends on the definition of its characteristic length.

The time step control algorithm in LS-DYNA is responsible for updating, along with the stresses and forces, the size of the time step through looping over all the elements and taking the minimum value. Additionally, the chosen value is multiplied by a safety factor (< 1) that ensures the stability of the solution (TSSFAC parameter in LS-DYNA nomenclature). In the case of solid

elements, which are the ones used in this MSc thesis, the critical time step is calculated according to Eq. 2.15.

$$\Delta t_e = \frac{L_e}{[Q + (Q^2 + c^2)^{1/2}]}, \tag{2.15}$$

where Q is a function of the bulk viscosity coefficients C_0 and C_1, which describes the resistance to rate of change of volume of the material, $L_e = \dfrac{v_e}{A_{e_{max}}}$ the characteristic length, with v_e the element volume and $A_{e_{max}}$ the area of the largest side, and **c** is the adiabatic speed of sound, which is a function of material properties (E, ρ, ν...). For a more detailed formulation refer to LS-DYNA Theory Manual, Section 22.1 [26].

Implicit integration

On the other hand, the implicit integration algorithm needs for information at two time steps for its solution, t_n and t_{n+1}, which is a priori unknown. Therefore, an iterative process is necessary to ensure global equilibrium convergence. LS-DYNA employs an incremental-iterative numerical algorithm that updates the time increment based on the ease of convergence of the method. Several algorithms are available that result from variations of the fundamental Newmark's method [26]. This method is unconditionally stable (at least for linear problems), implying that the time step is not necessarily limited to a maximum value, even though it must be set in accordance to the physics of the problem to obtain an accurate solution.

More about implicit time integration formulation can be found in LS-DYNA Theory Manual, Section 34 [26].

Comparison

Regarding the evaluation of the relative advantages and disadvantages of each scheme, a more functional view of each one has been taken in order to tailor the simulation conditions for different types of problems. The implicit approach has the advantage of exactly, or within a very small tolerance, satisfying the equation of motion and being able to use higher time increments. From this, it can be easily concluded that it can potentially lead to overall lower computational times. However, an iterative process is required for the convergence of the equilibrium condition and the inversion of the stiffness matrix requires high computational effort. Consequently, the amount of time it takes to converge at every time step is a priori unknown. This convergence can vary greatly from problem to problem, and in some cases, equilibrium may not be achieved.

Concerning the mesh, although it has less influence on CPU time compared to explicit integration, implicit time integration appears to be more sensitive to its quality. Mesh quality is

based on the uniformity and organization of node distribution, as well as the similarity of the elements to a cube (3D) or a square (2D). Therefore, if a low quality mesh contains highly distorted elements or even elements with negative Jacobians, the algorithm may not be able to solve it. Furthermore, care must be taken of initial penetrations in the contact definition, unconstrained degrees of freedom and non-smooth material constitutive curves, amongst others. For all the mentioned reasons, this type of scheme is typically used for static, quasi-static, or low-frequency dynamic problems, and, usually, for longer problems (those taking several seconds of real time).

Meanwhile, the explicit integration is particularly effective in handling highly nonlinear problems with high frequency phenomena, large velocities. The reason for this is that since its time step is inherently very small, it is able to capture the physics of events even if they have a very short characteristic time. However, this comes with the disadvantage of being a conditionally stable scheme, with its maximum time step limited for obtaining precise and bounded results. Therefore, the number of time steps required to solve a problem using an explicit scheme can be 100 to 10,000 times greater than that of an implicit scheme [26], thus limiting its use to short-duration processes. Finally, it is common to use explicit integration schemes when more sophisticated material models are to be implemented, or when a large number of sliding and contact interfaces are expected in the simulation.

In summary, each scheme has its own advantages and disadvantages, and it is important to select the most appropriate method for the specific problem being addressed. For the present case, the explicit scheme is used in all simulations due to the nature of the impacts and interactions involved in the FBO. However, the implicit scheme is also employed to obtain the blade pre-stress and its modal analysis.

2.5.5 Contact

This section highlights what contacts are and their crucial role in impact simulations. Additionally, the different algorithms considered in this thesis and that are available in LS-DYNA are presented. Therefore, the objective of this section is to provide the reader with basic knowledge about the internal architecture of contacts in LS-DYNA in order to justify the decisions made and serve as a reference for subsequent analysis sections.

The contact algorithm in a FEM simulation bases its functioning on the definition of certain surfaces formed by existing nodes and elements to prevent parts of the model from penetrating or separating from each other. In this case, this allows the disconnected Lagrangian elements to interact with each other as desired. Depending on the contact interaction during the physical process and the conditions of the numerical model, the treatment varies, which is why LS-DYNA offers a wide range of options with numerous parameters. The process of handling them is described in

more detail in subsequent sections, where only those contacts whose impact has been proven to be relevant are included. Proper setup of contacts is a crucial element in the construction of FEM simulations as it typically consumes a significant portion of the CPU time[3].

In this context, contact is defined by identifying locations that need to be checked for potential nodal penetrations. This can be done in various ways, such as globally identifying the different parts that will interact or defining slave nodes and master segments in contact pairs. On the one hand, a "segment" is defined as the face of an element (3D case) that is included in the contact. On the other hand, the terms *master* and *slave* refer to the roles each part plays in a contact pair. This, in turn, divides the treatment of contacts into two types: *one-way* and *two-way* contact. As shown in Fig. 2.10, in the case of one-way contact, the master is usually the part that is more coarsely meshed, and only the slave nodes are checked for penetration. However, in two-way algorithms, the roles are constantly reversed, and therefore the search for penetrations is performed symmetrically, eliminating the importance of the master-slave distinction. Although the first option is faster for obvious reasons, in this work, the second option has been employed due to the demanding conditions encountered in impact during an FBO event.

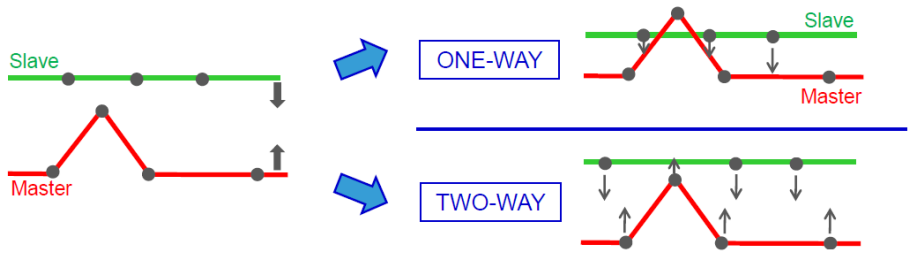

Figure 2.10: Simple graphical example illustrating the differences between one-way and two-way contact [45].

This leads to the introduction of the way contacts are currently defined for simulating these types of events. Historically, this was done by individually defining all expected contact pairs. However, this approach becomes impractical when the different interactions are not completely clear at a first glance. Similarly, the definition of self-contact could also be a tedious process. For this reason, robust "*single-surface*" algorithms have been developed, allowing all potentially interacting parts to be included under a single definition. This global contact approach offers significant advantages in terms of pre-processing, numerical robustness, and computational efficiency, which is why this formulation has been chosen.

In summary, a single-surface type of definition and a two-way penetration search are employed for the different contact interactions, i.e. released blade - fan case, released blade - trailing blade,

[3]According to the obtained results, this portion usually ranges between 20-30% of the total CPU time.

and trailing blade - fan case.

The following essential differentiation is based on the method used to enforce non-penetration conditions. Firstly, there exist the so-called *constraint-based* methods. Their basic operation relies on applying kinematic constraints in the global equations by transforming the nodal displacements of the slave nodes along the contact interface. On the other hand, a penalty-based method can also be used. In this case, the contact treatment is internally represented by linear numerical springs between the slave nodes and the closest master segments. When a node penetrates the segment, it is detected by the search algorithm and the depth of penetration is calculated. A force is then applied to the node that has penetrated. Thus, the stiffness of these fictitious springs determines the magnitude of the forces applied to the penetrating nodes to bring them back to the surface. This method has been proven to be very stable and to barely excite mesh hourglassing.

As illustrated in Fig. 2.11, two forces are applied: one in the normal direction (F_N) and another in the tangential direction (F_T) to the master segment.

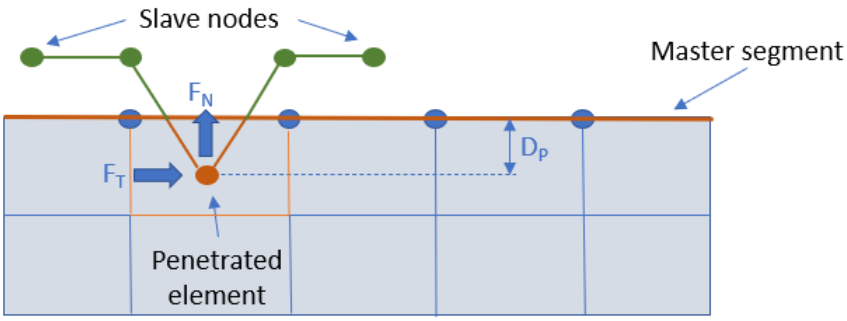

Figure 2.11: Diagram of a slave node penetrating the master segment and contact forces application.

The first force (Eq. 2.16) is the result of the product of the numerical spring stiffness (k) and the penetration distance of the node (D_P). The contact stiffness for solid elements is calculated as indicated by Eq. 2.17. Here, f_s is the penalty factor, **A** is the contact area of the segment, **K** is the bulk modulus, which takes into account material properties such as **E** and ν, and **V** is the volume of the element in question. As can be deducted, the applied contact forces depend on the material properties of the involved parts, even for rigid materials, for which these properties must also be defined. In the case of dissimilar materials, the lower of the two stiffness values is chosen for the force computation. Concerning the penalty factor, this can be manipulated by the user in order to adjust the stiffness and obtain the desired contact behavior.

$$F_N = k \cdot D_P \tag{2.16}$$

$$k = \frac{f_s \cdot A^2 \cdot K}{V} \tag{2.17}$$

Regarding the tangential force , it is based on the Coulomb friction model, as indicated by Eq. 2.18, and is proportional to the normal force and a user-defined friction coefficient, which is material-dependent.

$$F_T = \mu \cdot F_N \tag{2.18}$$

The last relevant distinction is related to the node penetration search method. Only one of them has been considered due to its clear advantages over the others, so it has not been deemed necessary to extend its explanation beyond its mention. This method is the *Bucket Sort approach*, which replaces incremental search methods by offering a more efficient and faster alternative. For more information, please refer to the LS-DYNA Theory Manual [26].

There are two final aspects that are relevant in the definition of these single surface, two-way, penalty methods, namely, the *contact viscous damping* and *eroding contact* option. In the first case, viscous damping is an artifact that dampens normal oscillations at the contact surfaces. To activate it, a desired damping value as a percentage of critical damping, $c_c = 2m\omega$, is required, where ω is computed with the minimum mass of the contact pair and the interface stiffness. The introduction of this parameter is very useful for noisy contact forces. On the other hand, *eroding contact* is a way to invoke the updating of the contact surface as elements are deleted due to material failure. This feature is highly recommendable when element failure is expected, as is the case here.

Tied contacts

The explanation of this type of contacts has been isolated due to the fact that they serve a different purpose than non-penetration contacts. As their name suggests, the so-called ”tied contacts”, aim to join two different meshed parts.

Their operation is based on constraining the movement of the slave node with the master surface. Consequently, it is not possible to use them to join deformable and rigid parts. Therefore, a variation of this method can be employed, which uses a penalty-based approach that allows for a certain ”off-set distance” between the slave and the master, thus softening the kinematic constraints.

2.5.6 Hourglass Control

Hourglass control is an important algorithm implemented in LS-DYNA to address the issue of hourglassing in finite element simulations. Hourglassing refers to spurious modes of deformation

that can occur in certain elements, leading to unrealistic results and numerical instabilities. Their characteristic way of deformation takes place orthogonally to the strain calculations, and, consequently, is neglected in the energy equation (no energy associated). In Fig. 2.12, a representation of four of the twelve hourglass modes that an underintegrated hexahedral solid can undergo is presented.

Hourglass modes arise from the use of underintegrated elements, with the exception of triangular shells and tetrahedral solids. In this specific case, all elements used are hexahedral solid elements with only one integration point at their center. This choice is made because it is the most robust and efficient option, allowing for faster simulations. However, it comes with the disadvantage of potentially encountering these non-physical modes of deformation.

The reason for this is that the use of underintegrated elements further limits the ability of the discrete system to accurately capture certain modes of deformation due to their reduced number of integration points. This problem can be partially or completely mitigated by locally refining the mesh, as this increases the number of integration points in the problematic areas, allowing for a better representation of the deformation modes. Despite this, generally, it is still recommended to use anti-hourglass algorithms and monitor their behavior.

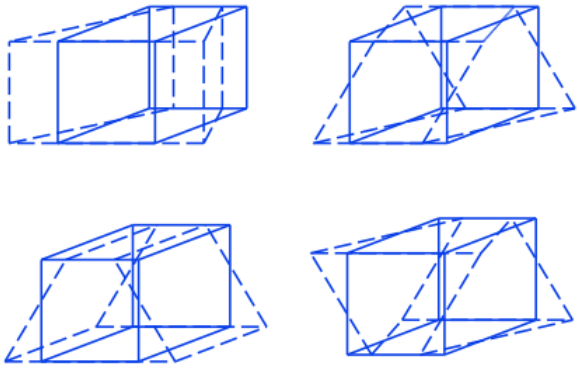

Figure 2.12: Representation of four hourglass modes of an underintegrated hexahedral solid [26].

Through different approaches, the hourglass control algorithm aims to counteract these undesired deformations through the application of opposing numerical forces, as can be observed in Fig. 2.13. The selection and application of the hourglass control algorithm (*IHQ* in LS-DYNA), including the appropriate type of hourglass control and coefficients, depend on various factors, such as the specific element formulation, material behavior, and simulation requirements. Proper implementation and configuration of the hourglass control algorithm are essential to obtain accurate and reliable results. Additionally, the application of this artifact must be applied with care since significant energy dissipation, which is the result of the work done by these hourglass forces, is to be avoided. A common way to assess its effectiveness is by evaluating the **ratio of hourglass**

energy to peak internal energy. A general practice is to ensure that this ratio stays lower than 0.1 for the entire model and, ideally, each part.

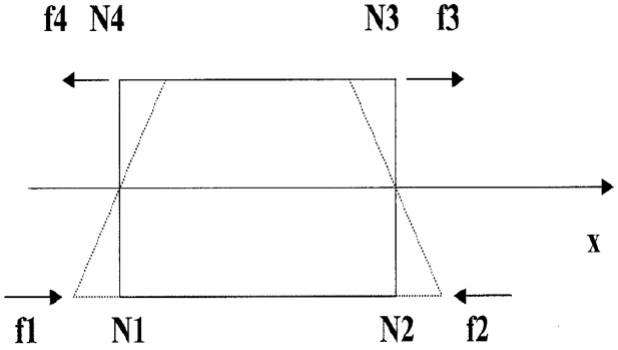

Figure 2.13: Simplified graphical example of the application of numerical forces (f_1, f_2, f_3 and f_4) to their respective nodes (N_1, N_2, N_3 and N_4) to counteract an hourglass mode of deformation (dotted line) [9].

For explicit solutions, especially those involving high-velocity simulations with high strain rates, the use of the **viscous hourglass control** is usually recommended. This type of hourglass control applies forces that are proportional to the nodal velocities, effectively suppressing incremental hourglass deformation, but not being able to recover from previously accumulated hourglass deformation.

For implicit simulations, only one type of hourglass control is available, which is a **stiffness-based hourglass control**. This approach can also be used for explicit solutions, especially for those involving low to moderate velocity phenomena. In this case, artificial counteracting forces are applied proportional to the hourglass modes displacements, thus having the ability of reducing accumulated hourglass deformation. While in general these algorithms are more effective in suppressing hourglassing modes than viscous ones, they have the disadvantage that they can sometimes over-stiffen the part to which they are applied. In order to minimize this effect, it is advised to reduce the hourglass coefficient (*QM* in LS-DYNA).

In conclusion, the hourglass control algorithm in LS-DYNA plays a crucial role in stabilizing these parasitic zero energy modes and improving the accuracy and stability of FEM simulations. By employing the recommended hourglass control methods, accurate and reliable results can be achieved for the FBO event simulation. Further details about its application and parameters modification are included in Chapter 3.

Chapter 3

Numerical model

This chapter provides a detailed description of the geometric features, meshing, material properties, boundary conditions, and other numerical parameters of the hard-wall containment model. In addition, the main assumptions and simplifications of the model are presented, along with pertinent modeling characteristics of the explicit software.

Section 3.1 presents the general simulation conditions, aiming to provide the reader with a common reference point for all subsequent variations. Section 3.2 is focused on studying the insensitivity of the results obtained in the elastic region with respect to the blade mesh. The results obtained are presented in different sub-sections, serving as justification for the decision of the optimal mesh in this case.

Next, in Section 3.3, a similar process is explained, analyzing the sensitivity of the numerical results to the mesh, but this time considering the entire Hard-Wall Containment model. Similarly, the results are presented, justifying the final choice and acknowledging the limitations of the model.

Finally, Section 3.4 presents the different taken ways to improve the model, particularly in terms of mesh refinement, and showcases the results and conclusions obtained throughout the process.

Lastly, it should be mentioned that some LS-DYNA specific syntax used in this work has been provided for LS-DYNA users. The detailed explanation of each of the so-called ”cards” (marked by a * at the beginning) that contain all the numerical parameters is not included in this explanation, as it could overwhelm the discussion of the FBO. For more information on this, please refer to the LS-DYNA User Manual [35].

3.1 Generic Numerical Model

In this section, the general conditions of the numerical model are presented, without focusing on the mesh. The aim is to create a common framework for all subsequent simulations in order to obtain consistent results, solely attributed to intentional variations. The attributes presented in this section encompass a combination of physical conditions of the actual FBO event, such as rotation speed, boundary conditions, or materials used, and numerical model characteristics, such as material models or the type of element employed, among others.

It is important to note that all the work carried out here is part of a "proof of concept". A proof of concept refers to a demonstration or preliminary study conducted to evaluate the feasibility and potential of a particular approach or idea. In this context, the development of a numerical model and conducting simulations have served as a proof of concept to assess the viability of the proposed methodology to simulate the FBO event. However, it is crucial to acknowledge that the work cannot be taken further (verified model) due to the lack of data for model validation and verification against real-world observations. Validation experiments and comparison of simulated results with empirical data are essential to establish the reliability and applicability of the model. Therefore, it is necessary to emphasize that this work is limited to a preliminary "proof of concept", and any further conclusions or practical applications would require rigorous validation based on reliable experimental data.

3.1.1 Simulation conditions

Firstly, in this subsection, the translation of the physical conditions of the FBO event for the fan of the EleFanT [11] project to the numerical model is presented. The International System of Units (SI) is being used consistently throughout the entire work.

Unless stated otherwise, all simulations are performed in single-precision using the Central Different Method explicit integration scheme [26] with LS-DYNA default values. A security scale factor, *TSSFAC*, for the time step of 0.9 is applied. This value has proven to be sufficiently low to capture the relevant physical events of the problem without destabilizing the solution, while also not excessively penalizing the total CPU time. Finally, the FBO simulation covers a total time of 10 ms, which is approximately equivalent to half a revolution.

It should be noted that the images shown in this section to illustrate the different parts correspond to a generic model in terms of meshing, so their sole purpose is to facilitate layout visualization. Therefore, mesh characteristics are of no interest here and will not be discussed until later sections.

Boundary and initial conditions

The model consists of a 40^o sector representative of the hub (Fig. 3.1a) and the fan case (Fig. 3.2a). This comprises a total of five components: two consecutive blades with their respective attached platforms, and the fan case. No shaft, connections or bearings have been introduced as no post-containment dynamic response is studied. All geometry files have been provided by the industrial [11].

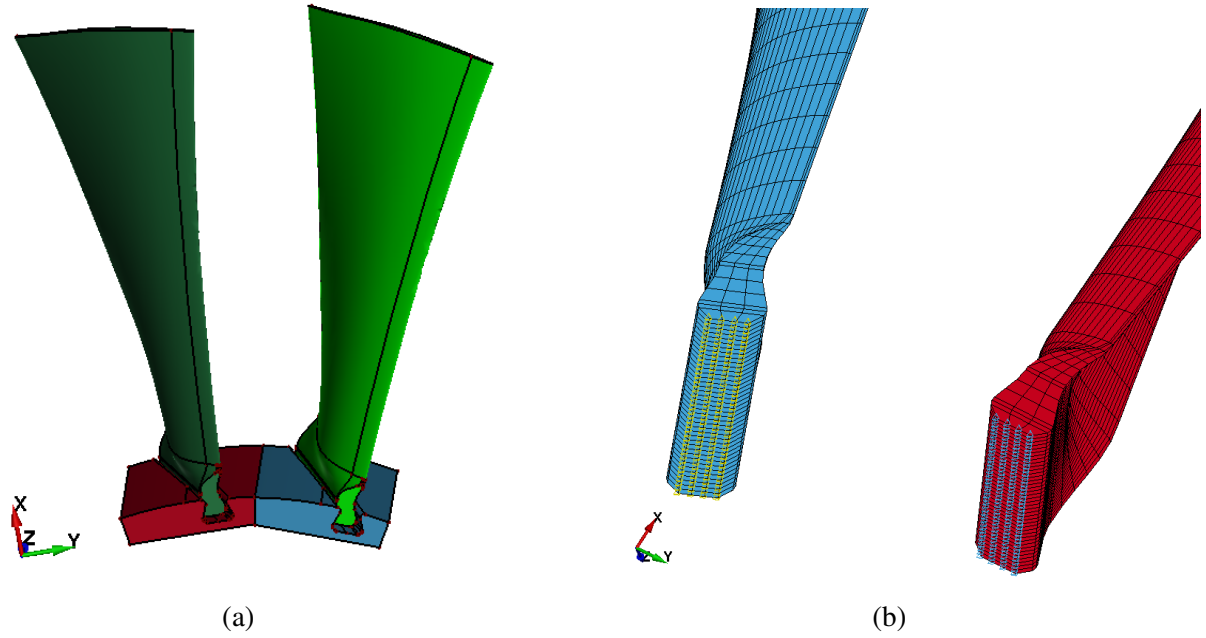

(a) (b)

Figure 3.1: Hub sector geometry representation (a) and location of applied boundary conditions in yellow (trailing blade) and blue (released blade) (b).

Regarding the hub components, they are constrained to rotate only around the positive direction of the z-axis, which coincides with the fan's axis of rotation. This condition is imposed on the blades through a prescribed motion applied at the nodes at the bottom of both dovetails (Fig. 3.1b). Thus, due to the imposed motion at the root, the blades' dovetails and platforms follow this rotational speed until the end time, simulating the incessant rotation of the rotor. In addition to the imposed rotation, an initial velocity is also applied to the rotor components. This rotational velocity around the z-axis continues until the impact or any other disturbance causes the blades to deviate from this condition. The initial rotational speed is 2747 rpm (287.6 rad/s), which is 15% higher than the nominal speed of 2390 rpm. This represents an over-speed condition of the engine, resulting in more energetic impact conditions.

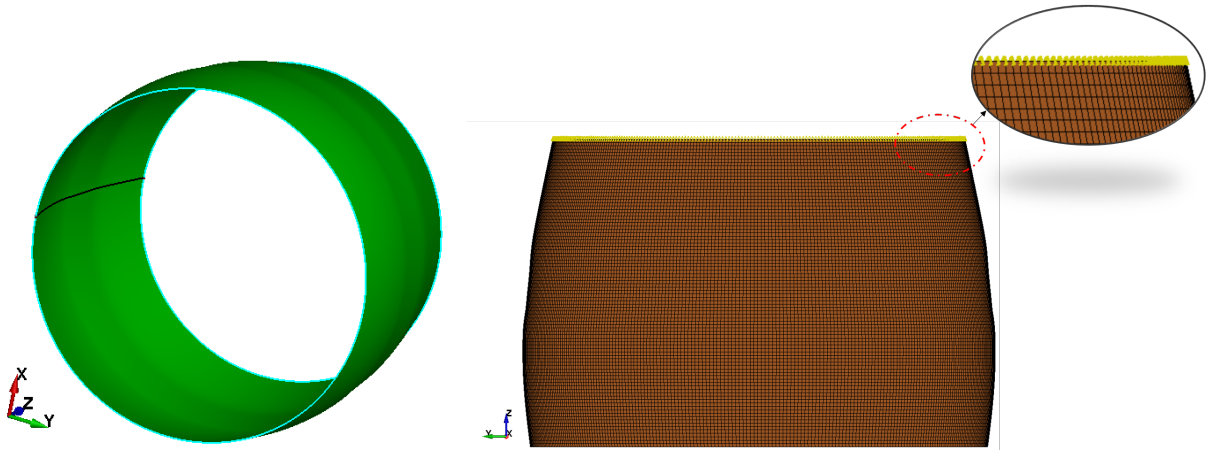

(a) (b)

Figure 3.2: Fan case geometry representation (a) and top view of the applied boundary conditions in yellow (b).

For the sake of simplicity, aerodynamic loads have not been included. Regarding the fan case, the so-called *Single Point Constraint* boundary condition has been applied. This condition constraints all six degrees of freedon in translation and rotation of all nodes at the fan outlet, representing the attachment of the fan case to the rest of the engine. In Fig. 3.2b, the location where this condition is applied is marked in yellow.

Finally, concerning the crack formation, propagation and blade release conditions, these are modeled through the detachment of elements from the upper part of the blade, specifically where the dovetail connects with the aerodynamic surface. This has been done in accordance with the regulation imposed by the FAA [24], which states that the release of the blade must occur at the outermost groove, which in this case corresponds to that area. In the analysis, the crack propagation velocity is assumed to be infinite rather than considering the sound velocity through the material. This assumption is based on the observation that the stresses do not undergo significant changes during the release process [52]. This leads to the simulation of an instant crack propagation in which the blade separates from the dovetail due to the centrifugal force. The exact location can be observed in Fig. 3.3, where how LS-DYNA interface represents the detached elements is shown.

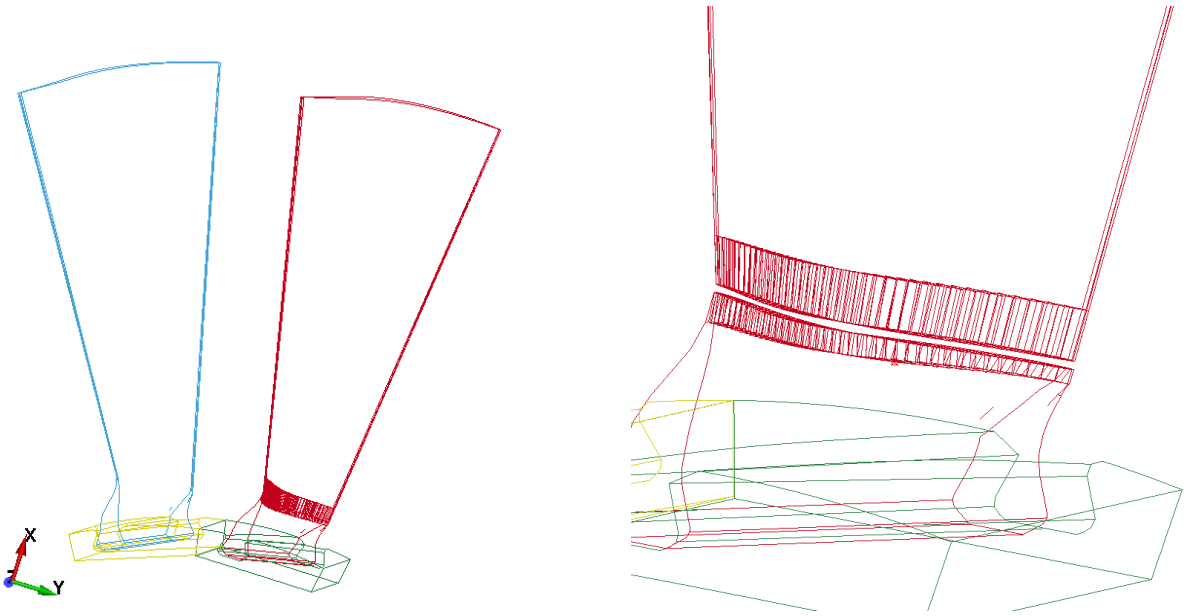

(a) (b)

Figure 3.3: Released blade root elements detachment at t= 0 ms (a) and detail at t=0.3 ms (b).

3.1.2 Element type

In FEA, the accuracy and efficiency of a solution are heavily influenced by the choice and quality of elements employed. One commonly utilized element is the hexahedral element, characterized by eight nodes and six faces. Gaussian integration is used to integrate the polynomial terms of the stiffness matrix of the element. Within this method, the full integration of the element refers to the use of the number of Gaussian points, or integration points, necessary to integrate these polynomial terms exactly (when the element has a regular shape). For the case of the hexahedral element, 2 integration points are needed in each of the three directions to obtain the full integration.

On the other hand, underintegration is a technique that reduces computational costs by employing a one fewer integration point in each direction. Therefore, a single integration point at the center of the element is used. Underintegrated formulations offer a balance between cost and robustness, while fully integrated formulations generally provide more accurate results, they can cause other problems like volumetric locking[1] and are computationally more expensive.

Hexahedral elements excel in capturing very large deformations, where distorted or irregular geometries are commonly encountered, making them suitable for modeling such scenarios. Among the options available, the 8-noded underintegrated brick element (*ELFORM*=1 in *SECTION_SOLID) stands out as the most robust choice offering a constant stress distribution within

[1]Plasticity or volumetric locking consists of the over-stiffening of fully-integrated elements when the material is close to being incompressible, i.e. when its Poisson coefficient (ν) is near or equal to 0.5.

the element (one-point Gaussian integration).

Despite potentially yielding good results for this problem, it is important to note that due to the reduced number of integration points per element, a higher mesh refinement is necessary to capture certain non-linearities. Additionally, this type of element is susceptible to the occurrence of hourglass modes, necessitating proper monitoring and control when employing these elements.

On the other hand, there is another type of 3D element, namely the tetrahedral element. Although tetrahedral elements do not exhibit hourglassing, they tend to suffer from locking tendencies and may not provide as accurate results, making them less preferable than hexahedral elements. This element has deliberately not been used in the present work due to the careful construction of the mesh. However, there are certain geometries that sometimes pose significant challenges when meshing them solely with hexahedral elements, as tetrahedral elements often adapt better to these shapes.

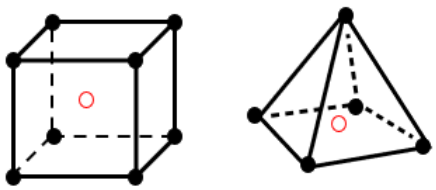

Figure 3.4: Underintegrated hexahedral element (left) and tetrahedral element (right).

Finally, the fan case could have been modeled using quadrilateral shell elements with the thickness of the fan case, as it is a relatively thin structure. However, above a certain thickness and as long as it is not too detrimental to computational time, it is generally recommended that these three-dimensional structures be adequately modeled with solid elements. One of the reasons for this is that, contrary to shell elements, these elements provide a more accurate stress and strain profiles through thickness. Therefore, brick elements have been used and the trade-off between computational efficiency and accuracy has been made in favor of achieving better results.

In summary, the selection of the element type plays a crucial role in the quality of the obtained results and computational efficiency. Thus, the chosen element type for this study is the underintegrated hexahedral element, with appropriate mesh refinement and control of hourglass modes.

3.1.3 Hourglass control

As mentioned before, one of the major disadvantages of using underintegrated elements is the appearance of spurious modes of zero energy called hourglass modes. However, these non-physical deformation modes can be limited and reduced in various ways. One approach is through refinement, as adding more integration points in the form of a higher number of elements allows for better capturing of the deformations experienced by the structure, thereby limiting the trigger for the occurrence of hourglass modes. This effect is reflected in the results presented in subsequent sections.

In addition, as explained in 2.5.6, hourglass mode control algorithms can be employed. Despite the usual recommendation of using viscous-type algorithms for high-velocity phenomena, the results provided by such algorithms have been surpassed by the stiffness-type algorithm. The stiffness algorithm has proven to be much more effective in reducing spurious modes without introducing excessive non-physical effects, which has been monitored through the evaluation of hourglass energy relative to internal energy.

Therefore, for both the blades and the fan case, the *IHQ*=4 formulation has been used, which corresponds to the Flanagan-Belytschko stiffness form (for more information, refer to the theoretical manual of LS-DYNA [26]). An hourglass coefficient (*QM*=*QB*=*QW*) of 0.03 has been employed for the blades, while a coefficient of 0.01 has been used for the fan case. Since this type of hourglass control tends to stiffen the solution, the default coefficient of 0.1 has been reduced to these values, while still ensuring good results. The remaining coefficients involved have been left at their default values, as recommended by LS-DYNA guidelines [16].

3.1.4 Contact algorithm

The type of contact employed is globally defined by the *CONTACT_ERODING_SINGLE _SURFACE card. As detailed in Section 2.5.5, single surface contacts are bidirectional, so there is no need to define master-slave contact pairs, as they apply to all components.

A viscous damping factor (*VD*) of 20% of the critical damping has been applied to reduce vibrations during contact (recommended [16]). Furthermore, the soft constraint option *SOFT*=2 has been used to determine the method for calculating interface stiffness, which in this case is the "pinball segment-based contact". The detection region parameter, *DEPTH*, has been set to 3, which renders an increased accuracy by checking penetration at segment edges, over the default value of 1. Lastly, the number of cycles between bucket sorts, *BSORT*, has been established as 100, which is usually enough for most applications.

Regarding frictional contact, a formulation based on the Coulomb model has been used

(Section 2.5.5). The values of the static and dynamic friction coefficients (μ_s and μ_d) have been obtained from a source provided in the theory manual [26] for dry aluminum-to-aluminum friction interaction. The value of the static coefficient ($\mu_s = 1.05$) has been employed for both coefficients, as it is recommended to avoid undesired instabilities derived from noisy contacts.

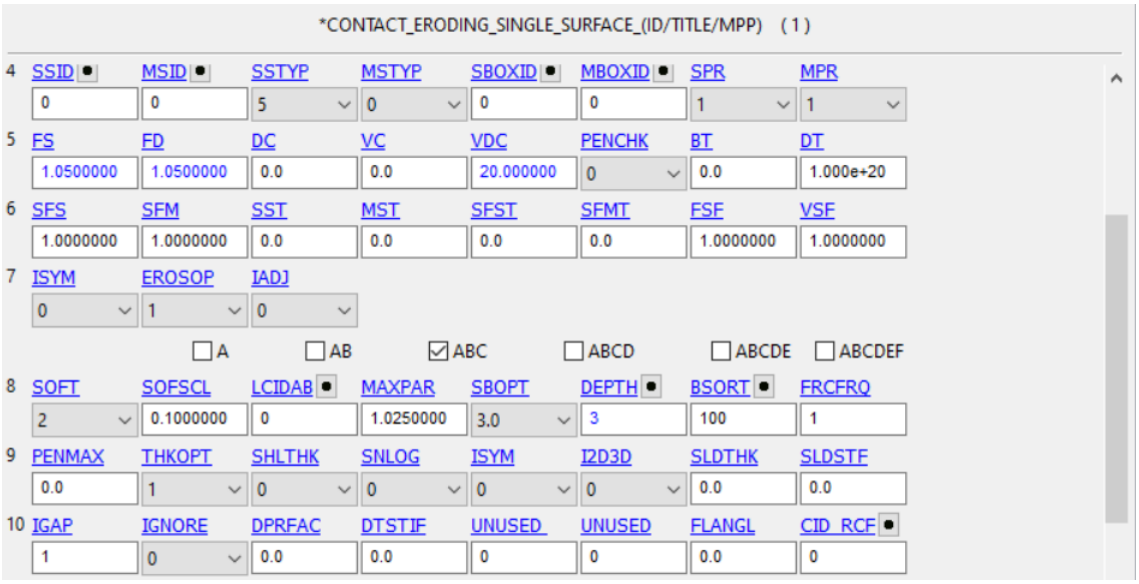

Figure 3.5: *CONTACT_ERODING_SINGLE_SURFACE LS-DYNA card.

It should be noted that this value has been used as a reference for typical values, but it would be advisable to perform friction tests with the materials to be used in order to obtain the real values. Furthermore, a common practice in hard-wall models is to use abrasive materials as the first layer between the blade and the fan case in order to dissipate a greater amount of energy in case of rubbing through the heat generated by friction. Consequently, if this design option was considered, this value would change significantly.

3.1.5 Material numerical model

In this section, the materials used in the different parts of the model and their relevant physical characteristics are presented. Furthermore, the numerical modeling of the aluminum alloys used is described.

Since strict instructions regarding the materials of each part have not been provided, except for the metallic blade, one of the commonly used materials has been assigned to each component. The chosen material is the aluminum alloy Al2024 with a T3 heat treatment. The properties of this material have been assigned to both the fan case and the platforms. The reason for selecting this material is that it is an aerospace grade alloy that is lightweight and strong, while being less

expensive than the material used for the blades, which is another aluminum alloy, AL7075, with a T6 treatment. The relevant characteristics of these two materials are presented in Table 3.1.

Material	ρ (kg/m^3)	E (GPa)	σ_y (MPa)	ν	$\bar{\varepsilon}_f^{pl}$
Al2024-T3	2768	73.04	367	0.33	0.12
Al7075-T6	2800	70.35	493.8	0.33	0.09

Table 3.1: Main material properties of aluminum alloys Al2024-T3 and Al7075-T6 [1].

It is important to mention that these data have been extracted from ANSYS Granta [2] material database, and that this has been the sole source used to provide uniformity to the information employed. Consequently, it is possible to find slightly different values in other data sources, as these values arise from specific tests under certain conditions that may result in these variations. Finally, it should be noted that both the yield strength (σ_y) and the effective plastic strain at failure ($\bar{\varepsilon}_f^{pl}$) refer to the value determined during a static tensile test at $T = 27^o$C and $T = 19^o$C, respectively.

Regarding its numerical modeling, the *MAT_PIECEWISE_LINEAR_PLASTICITY constitutive model has been employed for both materials, with its formulation and characteristics detailed in Section 2.4. In addition to inputting the values provided in Table 3.1 for each alloy, the isotropic hardening curve has been included as well, representing the relationship between effective true stress and effective true plastic strain. This curve consists of eight points, ranging from the yield stress with zero equivalent plastic strain to the failure point. The curves correspond to static tensile tests, and the values have also been obtained from the ANSYS Granta [2] database, which incorporates various sources including JAHM [7] and ASME [3].

Regarding other functionalities offered by this model, such as strain-rate sensitivity or the failure criterion by setting the effective plastic strain at failure, these have not been utilized. The main reason is that these numerical parameters must be modified according to a validated model or experimental results, as the value provided by the tensile test is incorrect due to the high triaxiality of stresses and more complex physics present in this problem. Additionally, failure models and criteria are highly dependent on the mesh. This inherent mesh dependency becomes apparent after the localization of yielding, such as necking in a simple tension test. A finer mesh will result in a higher value of failure strain in a corresponding, correlated failure analysis [16], as can be depicted from Fig. 3.6. In this figure, the ratio between the local and the global failure strain is plotted against the ratio between the element length size with respect to the length of the geometry being meshed.

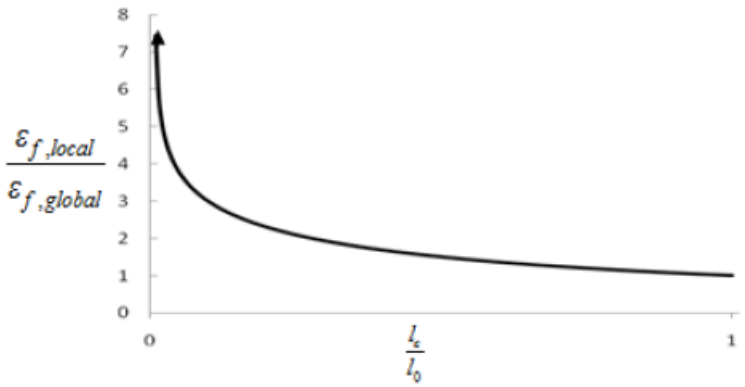

Figure 3.6: Mesh dependency on the local failure strain [16].

This is an intrinsic characteristic of these numerical models and therefore would require model calibration for each of the considered meshes. Not only does it depend on the mesh, but the results also depend on many other factors such as the type of element, the numerical algorithms used, or even the angle at which the impact occurs, thus requiring experimental results from a very similar model to the one simulated, which are not available. Although it poses a limitation in the model, as one of the interesting characteristics under study would be the threshold velocity for fan blade containment, failure has not been included in the main study.

Similarly, introducing strain-rate effects would require a thorough understanding of the material's response and the appropriate modeling parameters that need to be calibrated and fitted to be incorporated into the Cowper-Symonds model (Eq. B.1) to match the finite element calculation with experimental results [37]. However, material sensitivity to strain rate highly depends on its composition and treatment. Certain studies show that Al2024-T3 exhibits low sensitivity to strain rate [14], which is advantageous in this case. Despite the event occurring over a wide range of strain rates (0.001 - 1000 s^{-1}), given the intrinsic insensitivity of the considered material, the non-inclusion of this model can be considered a mild assumption.

Consequently, the addition of these features are proposed as a future part of the development of the model, once experimental results are available. However, in Section 3.5, the simulation results are shown to vary when introducing a failure criterion, as an example and proof of concept, acknowledging that the results are not validated and therefore may not correspond to reality. Regarding the effects of strain rate, by not including them, a more conservative solution is being obtained, as the yield is scaled with the strain rate. This would result in solutions where the fan case potentially withstands higher energy impacts.

It is also important to emphasize that the data used are reference values, and given the sim-

plicity of the LS-DYNA model construction, it is straightforward to replace them with appropriate values for the fan design. The two introduced curves are depicted in Fig. 3.7.

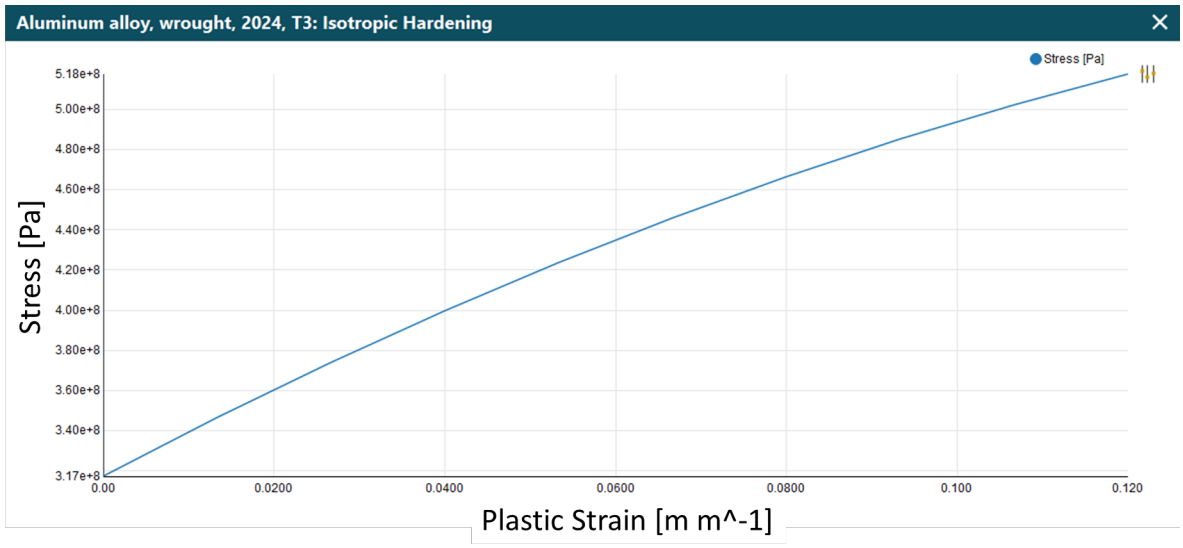

(a)

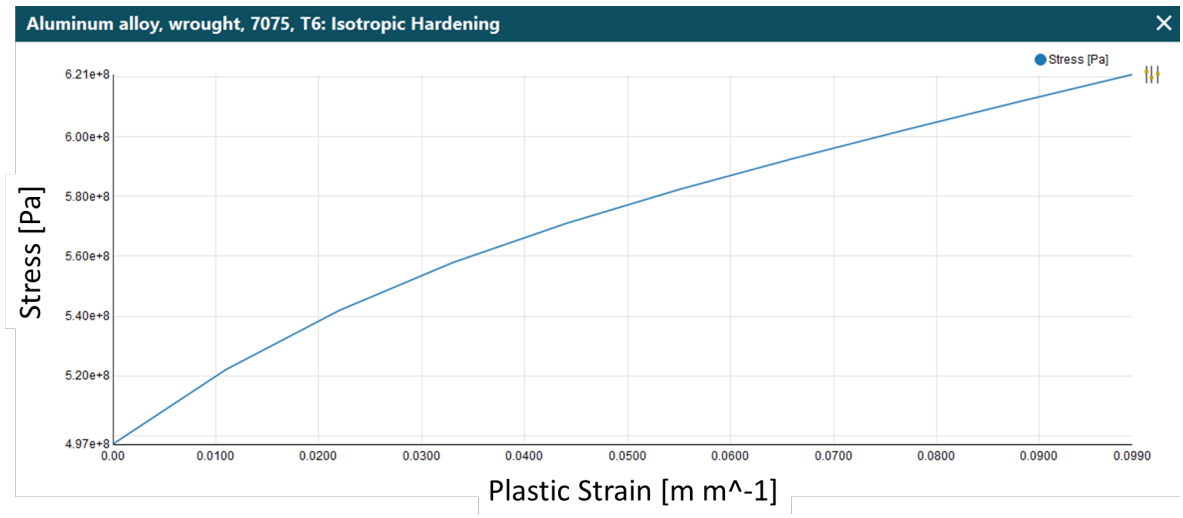

(b)

Figure 3.7: True effective (Von Mises) stress vs. True effective plastic strain isotropic hardening curves for wrought Al2024-T3 at T=27^{o}C (a) and wrought Al7075-T6 at T=19^{o}C (b).

Finally, regarding the platforms, the *MAT_RIGID model is applied. This is a powerful modeling technique that can induce significant CPU savings when applied to those parts where deformation and stresses are not of interest. Basic material characteristics are inputted (Table 3.1). The constitutive model values are used for calculating the interface stiffness during contact with other parts. Similarly, the density is employed for determining the platform's mass and inertia to simulate the dynamic behavior, since its primary function is as an inertial element.

3.2 Mesh Sensitivity Study of Blade Elastic Region

Once the common aspects of the simulations, whose results are presented in this chapter, have been established, the first part of the mesh independence study is detailed. This analysis is a fundamental process in any numerical model construction. The process is typically straightforward and involves progressively refining the mesh, either globally or in specific problematic areas, and studying the convergence of relevant results.

In this specific section, the focus is on choosing the coarsest blade mesh that provides independent results and a uniform stress field. Taking advantage of the need to initialize the blade with pre-stresses (double-precision with implicit integration scheme) before the explicit analysis, the study has been conducted during this process. Since the deformations experienced by the blade in these simulations (Section 2.2.2) remain within the elastic regime, the convergence of results and optimal meshing are ensured only for this region. This is because the convergence of results highly depends on the degree of deformation and distortion that the mesh undergoes. Therefore, a mesh that is optimal for the elastic region may not be optimal for the yielding zone, and even less so at failure. This second phase (plastic deformation zone) is evaluated during the study of the complete model in Section 3.3.

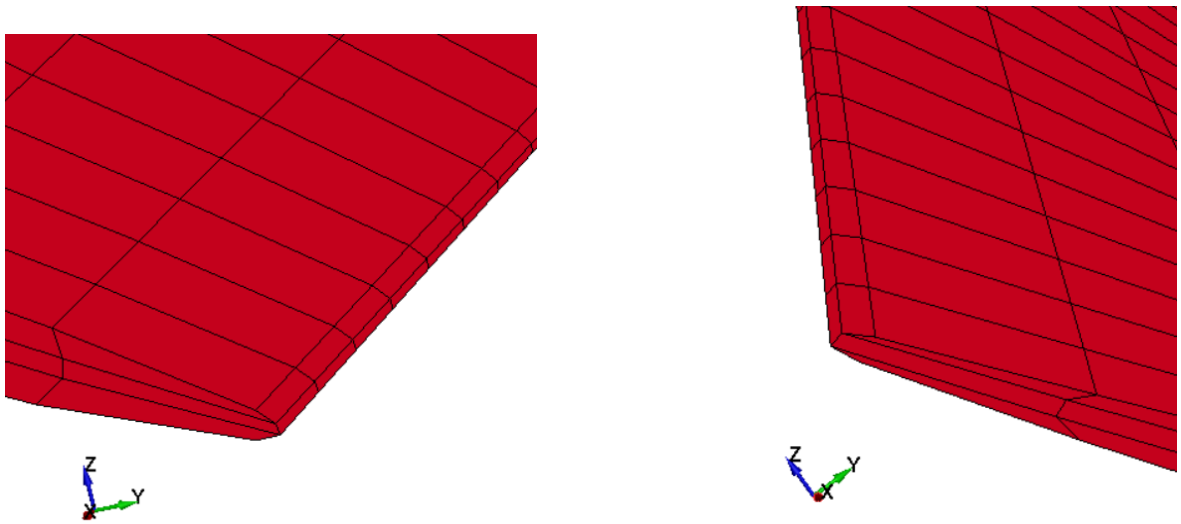

(a) (b)

Figure 3.8: Detail of blade leading edge (a) and trailing edge (b) of Case 1 mesh.

Capturing the precise initial impact of the released blade is crucial in accurately predicting the subsequent transient dynamic loads during a sequence of complex high-speed contact-impact events. To achieve this, the blade mesh should include sufficient detail to accurately represent the blade's aerodynamic shape and the pre-release steady-state stress field. As mentioned earlier, the

software ICEM CFD has been used for the meshing of the blade in order to have greater flexibility in creating a structured mesh. However, small geometric modifications had to be made to the shape of the leading and trailing edges.

These modifications involved transforming the rounded tips that make up these regions into a straight edge, as shown in Fig. 3.8, from which it can be deducted how this small change preserves both the inertia and aerodynamic shape. Apart from simplifying the meshing process itself, this modification also reduces the CPU computation time since due to the Courant condition (2.14) the elements along the leading and trailing edges determine the maximum value of the time step in all simulations.

A total of seven different cases have been considered, each with different mesh sizes and local refinements. Special attention has been given to placing a higher number of elements in areas where larger deformations and stress gradients are expected. These areas include the blade tip and the trailing edge of the blade. All simulations have been performed for both blades, maintaining the same mesh throughout, and all of them with three elements through thickness to capture non-linearities in this direction.

Some of the most relevant characteristics are summarized in Table 3.2. Additionally, in order to avoid overloading the report, detailed information will only be provided for cases 1, 4, and 7.

Case	**1**	**2**	**3**	**4**	**5**	**6**	**7**
Number of elements	1326	3024	5883	7605	9804	12348	17388
Explicit rotation CPU time (s)	190	1037	919	1365	2572	2933	7651
Blade mass (kg)	1.38726	1.39574	1.3983	1.39836	1.39878	1.39904	1.39948
Max. time step (e-08s)	6.368	3.252	2.46	2.374	2.221	2.003	1.593

Table 3.2: Blade mesh sensitivity study cases.

The number of elements mentioned refers to a single blade. The mass of the blade is evaluated to analyze the inertia approximation, which shows minimal variation despite the increase in the number of elements by approximately 13 times from case 1 to case 7. Additionally, the computation time for the explicit rotation is provided as a reference for the final model, along with the maximum time step limited by the smallest elements of the mesh. In Fig. 3.9, blue-colored elements indicate that a small time step is required. Therefore, it can be observed that the elements that have the greatest impact on decreasing computational efficiency are those composing the trailing edge. This is due to the complex geometry of the trailing edge and how the elements need to adapt to it, sometimes resulting in undesired high aspect ratios (aiming for close values to 1), as shown in Fig.

3.10.

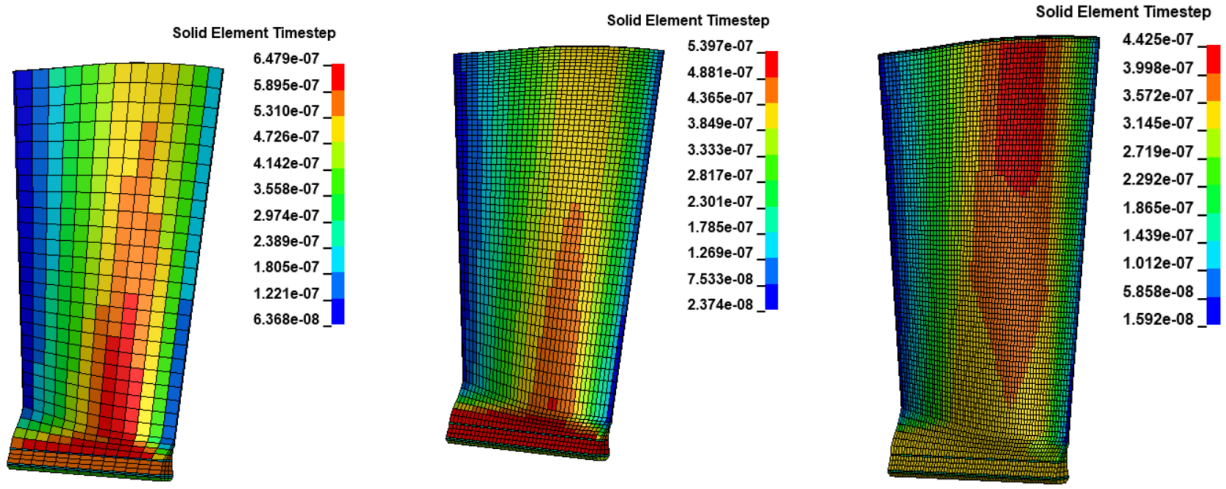

(a) (b) (c)

Figure 3.9: Time step fringe plot of cases 1 (a), 4 (b) and 7 (c).

From Fig. 3.10, it can also be observed that the refinement has progressively become more localized, resulting in improved aspect ratios in the more refined areas. Although case 7 provides better element quality in broader regions of the blade, it also results in a significantly reduced time step. Therefore, case 4 offers a more cost-effective solution with similar quality in critical areas.

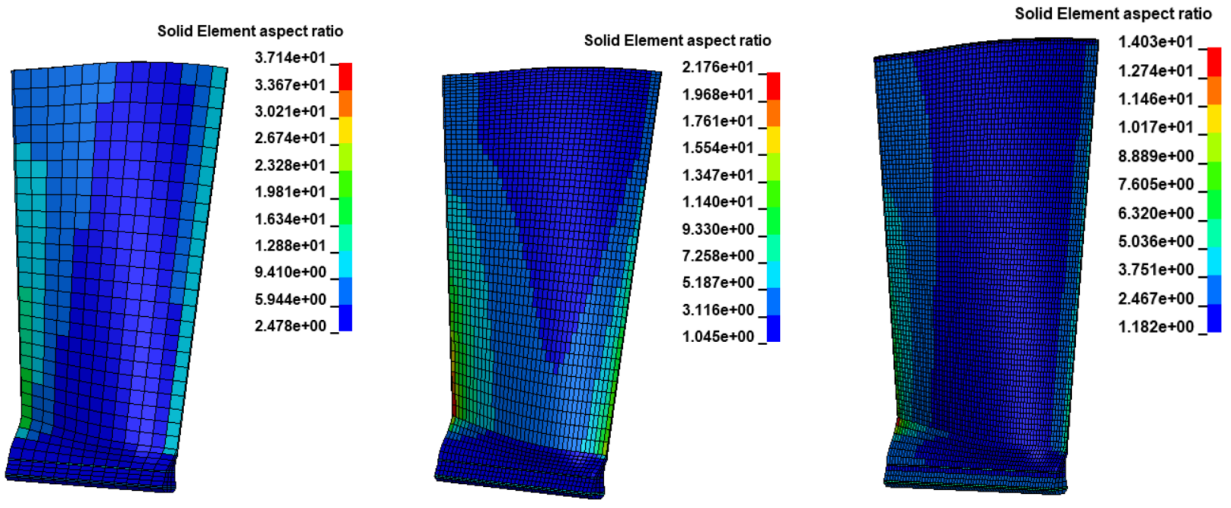

(a) (b) (c)

Figure 3.10: Aspect ratio fringe plot of cases 1 (a), 4 (b) and 7 (c).

Therefore, in terms of the trade-off between element quality, number of elements, and simulation time (Fig. 3.11), case 4 provides the best solution among the considered cases. With

a total time of 22 minutes and 45 seconds and an acceptable quality, the following subsections compare this case with the others in terms of the obtained results.

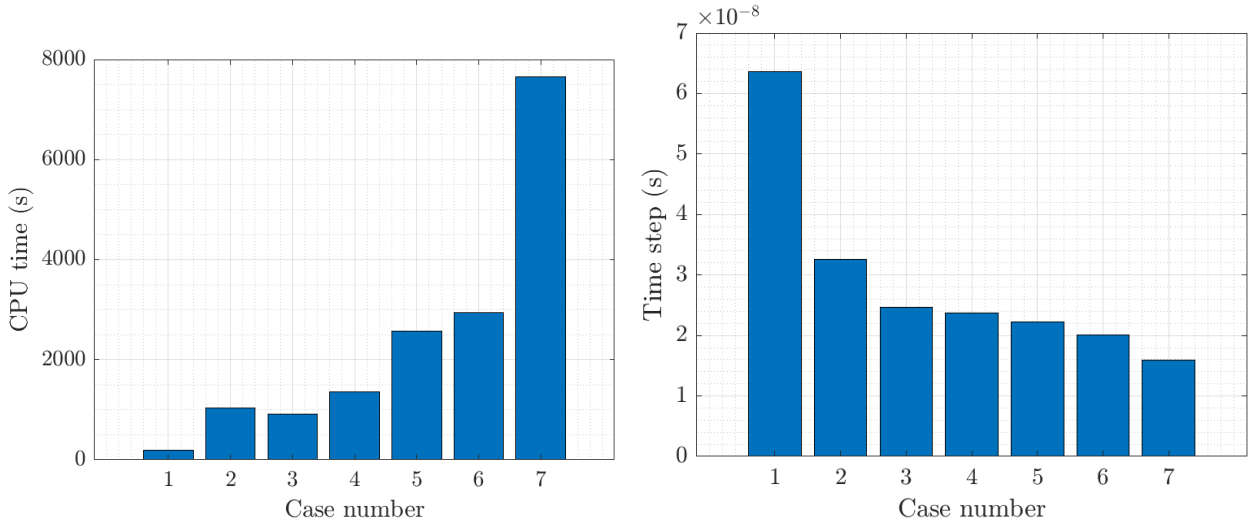

Figure 3.11: Explicit rotation CPU time (a) and maximum time step (b) for the different cases.

3.2.1 Pre-stress

For the convergence study of results in the pre-stress simulations, displacements and effective stresses in both pre-stressed blades are analyzed. As shown in Fig. 3.12, the values of displacements and stresses are very similar in all cases. Maximum Von Mises stress difference from the coarsest (case 1) to the finest mesh (case 7) is 2% with respect to the latter. In the same, a 0.4% difference in maximum displacement values. This indicates that the results are not very sensitive to the specific mesh refinement carried out here.

Despite that, it can also be observed that especially the stress distribution becomes smoother as the mesh is refined. This is an important consideration, especially in this model, as the constant stress element type is used. Consequently, if not refined enough, in regions with high stress gradients, the distribution may appear patchy and exhibit large changes with respect to adjacent elements, not being capable of properly representing the stress distribution.

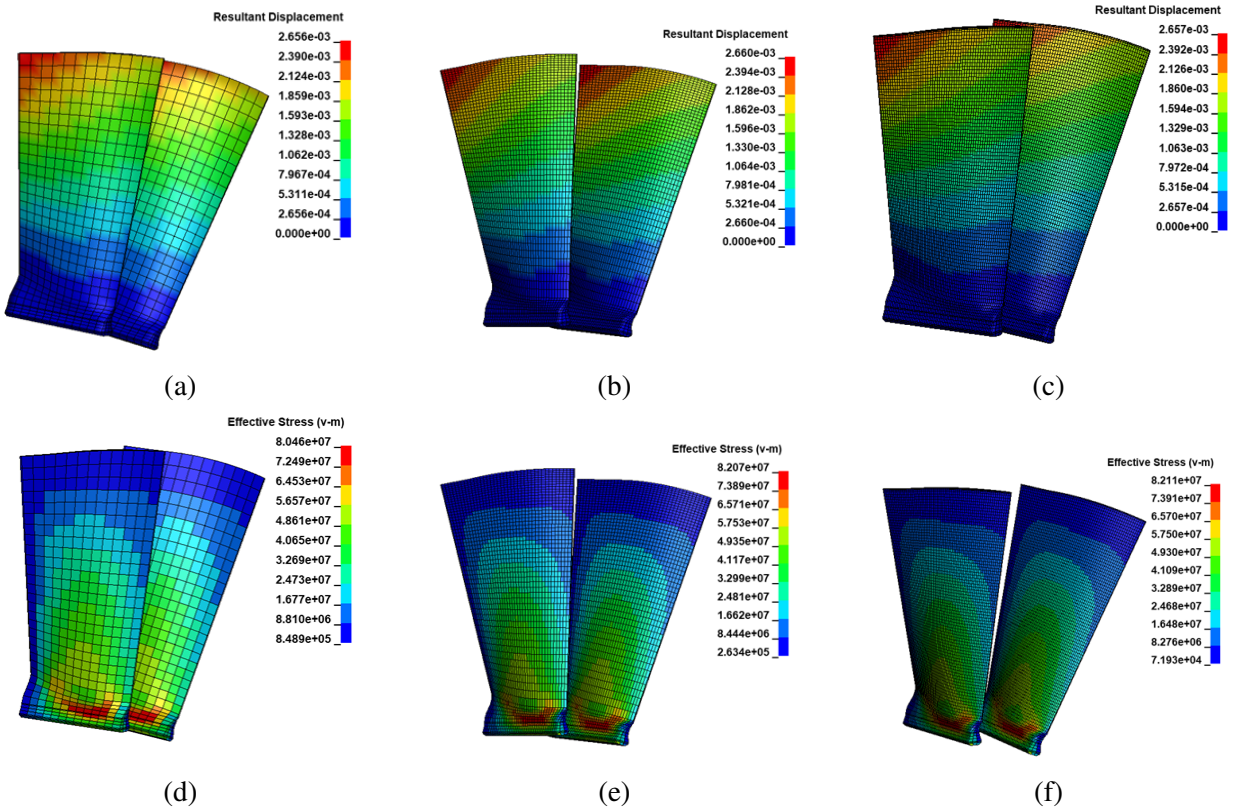

Figure 3.12: Resultant displacement fringe plot of cases 1 (a), 4 (b) and 7 (c) and effective stress of cases 1 (d), 4 (e) and 7 (f).

Thus, it can be concluded that case 4 continues to provide a good solution for displacements and stresses in the elastic region of both blades.

3.2.2 Explicit rotation

Hourglass energy is another important variable to study, which appears as a result of the applied forces by the hourglass control algorithm to counteract hourglass modes of deformation. The reason for this is that one of the techniques used to mitigate the occurrence of these spurious modes of deformation is the local refinement of affected areas. Therefore, it is expected that as the number of elements increases, the energy associated with the hourglass control will decrease towards more acceptable values. In the case of the explicit rotation simulation, the *IHQ*=2 viscous formulation for hourglass control has been used, which corresponds to the Flanagan-Belytschko viscous form [26] with default values. Therefore, it is also expected that achieving acceptable values with this less effective algorithm will imply similar or improved behavior in the complete model with the stiffness type. This will be reflected in the relevant results in Section 3.3.

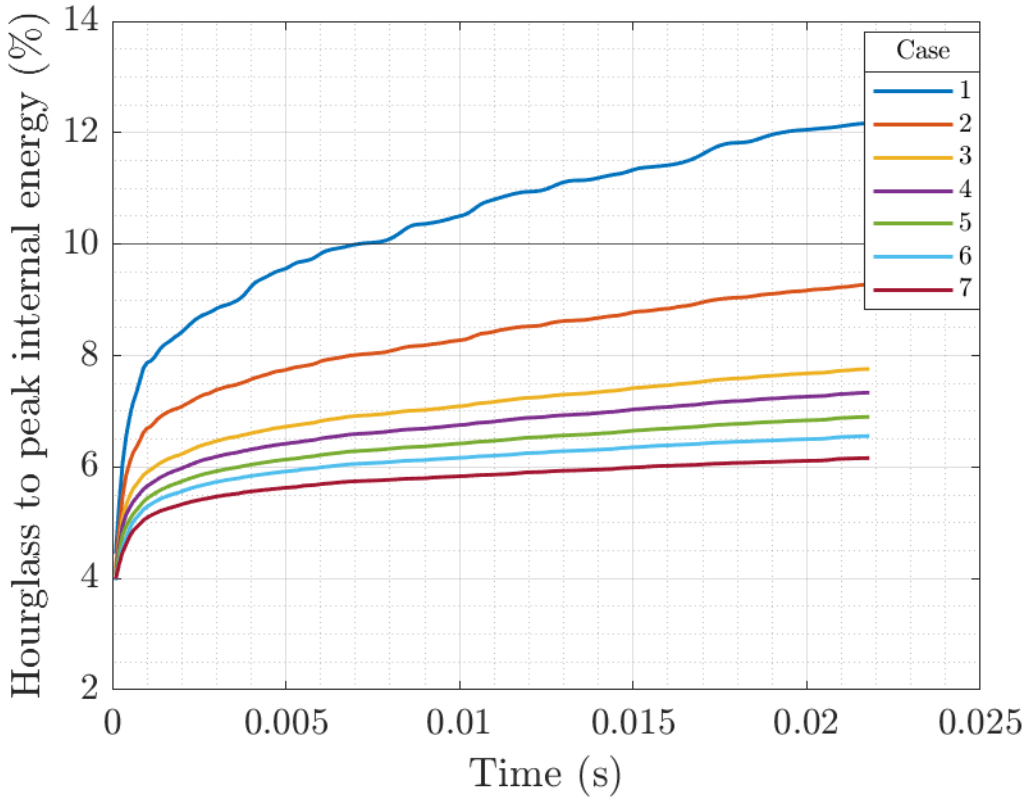

Figure 3.13: Time evolution of the hourglass energy ratio for the different mesh cases.

In Fig. 3.13, it can be observed that starting from the second case, the ratio of hourglass energy to peak internal energy is below the commonly established limit of 10%, which is extensively considered tolerable in most cases. It can also be seen that this ratio gradually increases over time, although its growth rate is reduced with refinement. Specifically, for case 4, the ratio reaches a maximum of 7.33% at t=0.021842 s, and an even lower value is reached at the final equivalent time of the complete model simulation (t=0.01 s).

Additional analyzed results from the explicit rotation simulation are the effective strain fringe plots at the end of the simulation. Fig. 3.14 displays the cases for three of the considered meshes. It can be observed that the variations in value are minimal ($\ll$1%), and the changes in gradients are smoother as the mesh is further refined.

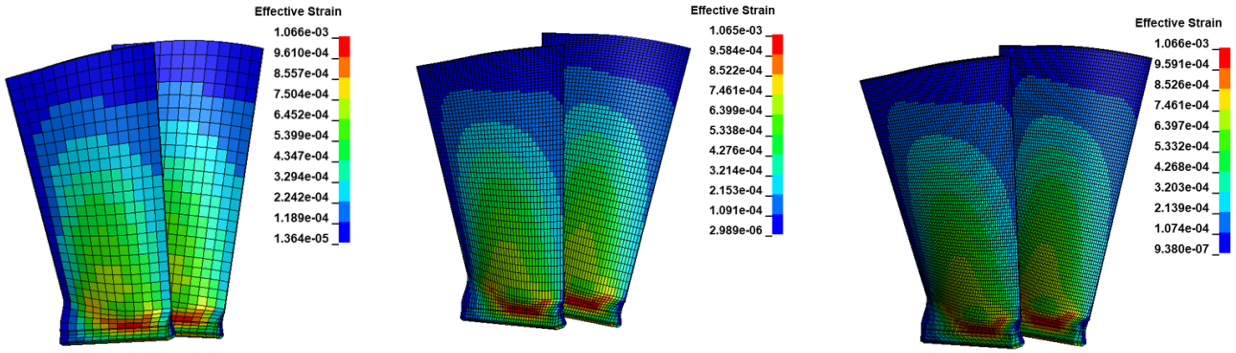

(a) (b) (c)

Figure 3.14: Effective strain fringe plot of cases 1 (a), 4 (b) and 7 (c).

Finally, it should be noted that cases 3, 4, and 5 offer very similar solutions. Therefore, the decision now rests on the trade-off between result quality and computation time. While case 5 almost doubles the CPU time with little relative improvement, there is only a difference of around 7 minutes between cases 3 and 4. Thus, it is more advantageous to choose case 4.

3.2.3 Conclusion

To verify that similar results are obtained for the cases of interest, a comparative analysis is conducted. The key parameters, such as displacements, stresses, and other relevant variables, are evaluated for all of them. The results show a high degree of similarity between all cases, especially 3, 4 and 5, indicating that the chosen mesh and refinement strategy have effectively captured the behavior of the system.

The displacements of critical points, such as the blade tip and trailing edge, are found to be consistent in both cases, with minor differences attributed to the mesh refinement. Similarly, the stress distribution in the blades exhibits similar patterns and magnitudes for both cases, indicating that the mesh refinement does not significantly affect the stress predictions.

Furthermore, additional performance indicators, such as computational time and resource utilization, are compared. It is observed that case 4 outperforms case 5 in terms of computational efficiency, with a negligible loss in result quality. This highlights the advantage of choosing case 4 as the preferred option.

Overall, the verification analysis confirmed that case 4 provides a reliable and efficient solution for capturing the elastic behavior of the blades while minimizing computational resources.

3.3 Mesh Sensitivity study of Hard-wall Containment Model

This section of the report focuses on the mesh sensitivity study of the complete Hard-Wall Containment model. The proposed model offers the capability to handle large strains and simplicity in its implementation. It serves as a starting point for modeling the complex multi-material systems with large strain behavior, although further development is required for improved accuracy, mesh calibration, and advanced constitutive modeling beyond the scope of this study.

Throughout the study, the meshes related to the platforms and blades remain unchanged, while the fan case undergoes refinement in each case with a more detailed mesh. To provide consistency across all cases, the number of elements through the thickness is maintained at three, which is the minimum necessary for capturing non-linearities with the underintegrated hexahedral elements. Note that the influence of the number of elements through the thickness is assessed in Section 3.4.

The thickness dimension of 6 mm for the fan case has been chosen based on the logical design considerations of the fan case architecture. It has been selected as a starting point for further investigation and analysis. In subsequent studies, the thickness dimension is varied to examine its effect on the results and to explore different design scenarios.

A total of eight cases are considered, where the level of refinement is determined by the element size, ranging from 30 mm to 5 mm. The quality of elements and the lowest characteristic length are evaluated for each case. To ensure that the model accurately captures the physics of the problem, global energies are analyzed and compared with typical expectations of a generic FBO event. Visual reproduction of the simulation is also compared to validate the model's representation of the problem. Component-level energies are studied to assess the validity of the results numerically and identify any deficiencies in the model.

Furthermore, various checks are performed to evaluate hourglass spurious modes of deformation and contact behavior. Finally, a detailed analysis of stresses and contact loads is conducted to corroborate the findings and conclusions drawn from the observed tendencies.

Throughout this section, the presented images that depict crucial events in the simulation or visual aids of what it is being explained, correspond to the selected case, namely Case 6. The justification for choosing this particular case unfolds progressively, providing a comprehensive analysis of the mesh sensitivity study's findings and their implications for the complete hard-wall containment model.

Overall, this section aims to investigate the mesh sensitivity, validate the model's physics, and provide insights into the behavior of stresses, loads, and contact in the complete Hard-Wall Containment model. All simulations have been performed with a computer with Intel(R) Core(TM)

i9-10900K CPU @ 3.70GHz processor and 128 GB of installed RAM, and similar computation conditions.

3.3.1 Fan case mesh

This section focuses on the meshing process of the fan case component and the rationale behind the used method. It is crucial to create a sufficiently detailed mesh for this structural element as it is the main subject of study and its deformation is of utmost importance for the safety and integrity of the engine. However, due to its size, creating a fine mesh to accurately represent the nonlinear deformations it undergoes requires a significant number of elements. Mesh construction is a process that relies heavily on experience, and final decisions often emerge from trial and error. As there is no established method, various possibilities have been considered in this study.

One issue to consider is the interpolation of the fan case's cylindrical surface by the linear segments that make up the elements. This can potentially induce rubbing between the blade tip and the fan case after none or mild deformation, since the clearances are very small for aerodynamic reasons ($\sim$ 1 mm). To avoid this, a highly refined circumferential mesh would be required. However, due to computational power limitations and time constraints, the simulation speed plays a significant role and this approach has been disregarded.

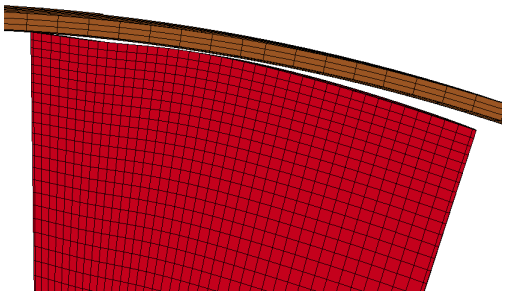

Figure 3.15: Fan case section (6 mm) illustrating the small clearances between the blade and the fan case.

Another challenge is ensuring that the mesh is fine enough to accurately reproduce a smooth distribution of contact forces. Creating an appropriate mesh for the problem at hand can greatly enhance simulation characteristics and results accuracy. A coarse mesh can lead to high and dynamic contact forces, since contact is defined by segments, and contact forces are resolved at the nodes. Thus, a highly-refined uniform mesh where contact pairs occur will result in smoother force calculations.

However, the issue lies once again in the computational capabilities and what the progressive refinement of the overall fan case mesh supposes in this sense, as depicted in Fig. 3.16. The figure

illustrates that as the element size decreases, the relative changes become larger, exponentially increasing the computation time.

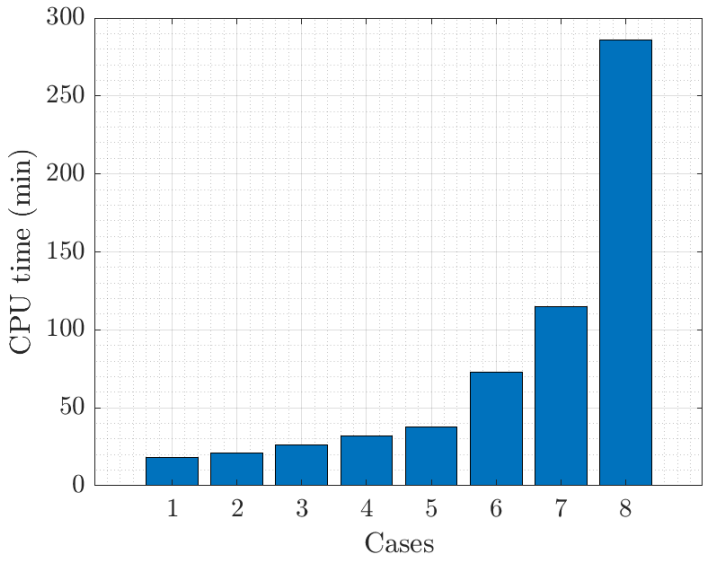

Figure 3.16: CPU time of the fan case mesh considered cases.

One considered solution to avoid an excessive increase in the model size was to locally refine the area of the fan case where contacts occur. This region is shown in Fig. 3.17. This study was conducted by maintaining a relatively coarse mesh (20 mm element size) for the rest of the fan case and progressively refining the problematic zone from the chosen element size (10 mm, Table 3.3) down to 2 mm. This configuration involves dividing the fan case into two parts, which need to be joined as a single piece in a certain way. LS-DYNA achieves this through so-called “tied-contacts”, which are discussed in Section 2.5.5.

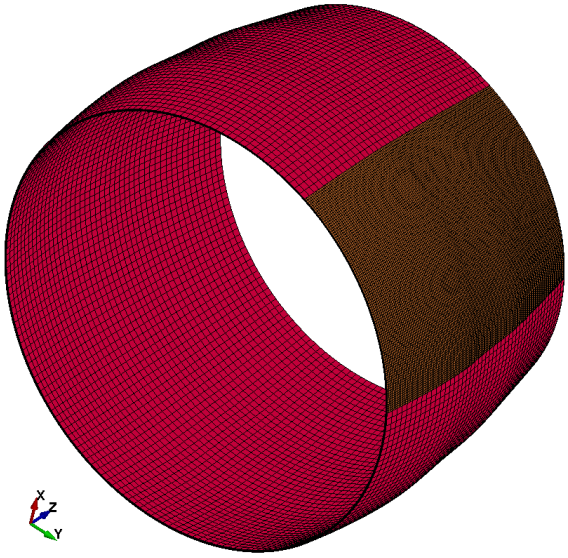

Figure 3.17: Fan case mesh model with locally-refined sector.

However, using these contacts with an off-set is not strict enough to maintain the two parts together (Fig. 3.18a), and using them with the kinematic constraint option imposes such strict conditions that simulation time sharply increases from 1 hour and 3 minutes to 7 hours and 42 minutes, and hourglass modes become prominent at the junction area (Fig. 3.18b).

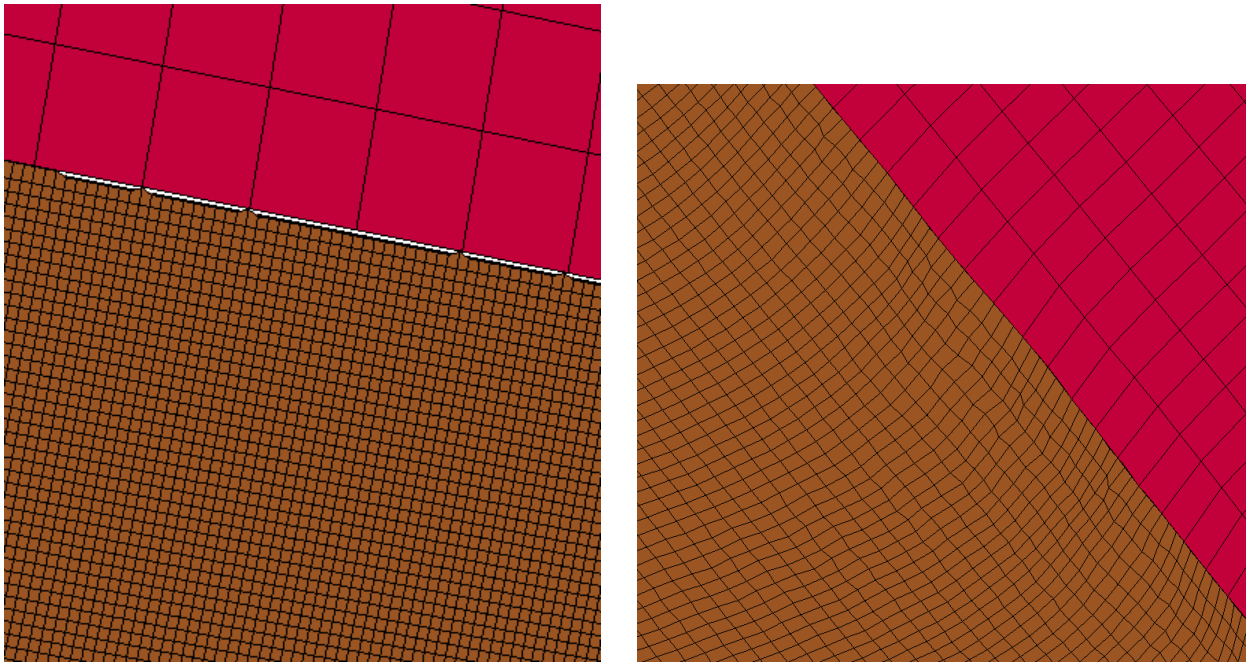

(a) (b)

Figure 3.18: Detail of the refined sector and the coarsely meshed part of the fan case joint using *CONTAC_TIED_SURFACE_TO_SURFACE_OFFSET (a) and *CONTAC_TIED_SURFACE_TO_SURFACE (b).

Therefore, despite the potential advantages in handling the contacts, this meshing technique has been discarded due to the additional complications it entails, and the fact that its relative benefits can be surpassed by accepting longer simulation times in the model under consideration. The characteristics of the finally evaluated meshes are summarized in the table below.

Case	**1**	**2**	**3**	**4**	**5**	**6**	**7**	**8**
Number of elements	12369	17760	27600	38070	48861	108927	171000	436254
Element size (mm)	30	25	20	17	15	10	8	5
CPU time (min)	18	21	26	32	38	73	115	286
Fan case mass (kg)	63.2639	63.2737	63.2817	63.2857	63.2881	63.2928	63.2942	63.2957

Table 3.3: Relevant characteristics of the Hard-Wall Containment model mesh sensitivity study.

In summary, the mesh sensitivity study of the fan case highlighted the challenges of creating a finely detailed mesh while considering computational limitations. Various approaches, including local refinement and tied-contacts, were considered but ultimately deemed impractical due to added complexities and increased simulation time. Thus, the decision was made to globally refine the fan case mesh, ensuring a balance between accuracy and computational efficiency.

3.3.2 Succesion of events during FBO

The purpose of this section is to provide a holistic view of the FBO simulation and highlight the behavior and response of the system under study. For that reason, various key moments of the simulation are presented to provide the reader with a physical understanding of the events and enhance the overall flow of the report. It is important to note that the results showcased in this section correspond to Case 6, which has been selected as the final choice based on the aforementioned considerations and analyses.

By visually representing critical moments in the simulation, such as the blade separation and subsequent interactions, the reader can gain insights into the physical phenomena occurring during the FBO event. These visual representations serve to complement the numerical data and analysis, allowing for a more comprehensive understanding of the simulation results.

The analysis begins with an examination of the global energies, which represent the sum of all components in the simulation. The study of global energies is crucial as it ensures the absence of spurious results during the numerical simulation and serves as a means to validate the physical

phenomena observed, confirming that the results are within the expected magnitudes. To better understand the significance of each energy variable within the LS-DYNA environment, a brief explanation is provided:

- **Kinetic energy**: This energy accounts for the work done due to the motion of nodes with certain velocities. Its value is proportional to the nodal mass and the square of its velocity. While not of primary numerical interest, this variable is thoroughly examined in the analysis of the fan case thickness effect in Chapter 4.

- **Internal energy**: This energy encompasses the strain elastic energy stored and the work done by permanent deformation (dissipated). Typically, other energies are compared to the internal energy as it represents the energy associated to the mesh and is the only physically related effect associated with deformations that should ideally be present (if there were no hourglass or contact energy).

- **Friction energy**: When friction is introduced in the model, this energy represents the work done during sliding between interfaces. It corresponds to the energy dissipated through friction and heat generation in the actual event. During simulations, it is desired for this energy to be positive and exhibit a smooth evolution.

- **Contact energy**: The contact energy should ideally not exceed 5% of the peak internal energy. This is due to the penalty method used by the contact algorithm, which relies on the use of virtual springs. As a result, opposing surfaces experience a displacement interference that generates a driving force to keep them separated. This force performs work, resulting in positive contact energy. However, this energy is not physically meaningful in the simulation, as it represents an increase in the potential energy of the contacting parts that would have been associated in reality with their physical deformation upon contact or kinetic energy.

- **Energy ratio (*ER*)**: This is the ratio between the total energy and the initial total energy plus the external work. Its evolution over time indicates how well the energy balance (ER=1) is maintained. The desired values are maximum deviations of 1-2% from 1. When the ratio exceeds unity, it indicates artificially introduced energy, which may be due to phenomena such as instabilities or penetrations.

The last two variables are not utilized in this section but are analyzed during the mesh convergence study. Additionally, the explanation does not include hourglass energy, as it has been discussed repeatedly throughout the report (refer to Section 3.2).

Note that all plots showing time are in *s*, since this is the unit used, but during the discussion *ms* is used to facilitate reading. Therefore, from Fig. 3.19, it can be observed that the onset of

events occurs approximately at 0.2 ms when the blade clears the gap between itself and the fan case by separating from its root due to centrifugal force. This is the first impact between the blade and the fan case, especially occurring at the leading edge zone of the blade tip. Generally, this initial interaction is not usually the most energetic, as observed in the graph.

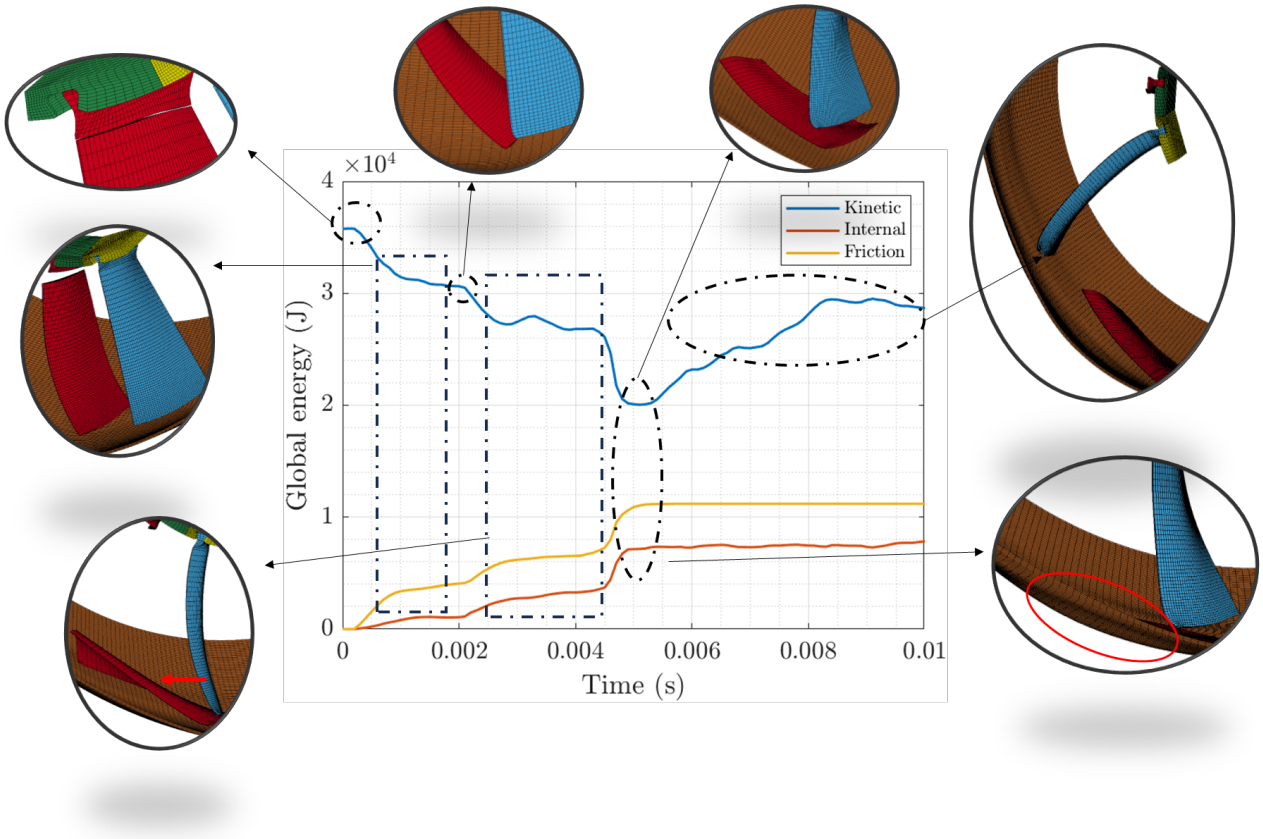

Figure 3.19: Case 6 global energies and key events.

When the blade is released, its velocity is tangential to the fan case (FC). Once the tip makes contact, the velocity starts to change direction. Both the overall energy graph and the blade-specific energy graph in Fig. 3.20 show a decrease in kinetic energy, primarily due to the released blade. During this initial impact, the upper part of the blade would break if the failure were included in the model. Both blades start with a kinetic energy of 14,000 J, a value within the expected range using a simplified calculation to estimate it.

$$KE_{blade_0} = \frac{1}{2} m_{blade} (\omega x_{cg_{blade}})^2 + \frac{1}{2} I_{z_{blade}} \omega^2 = 14107 J, \tag{3.1}$$

where $x_{cg_{blade}} = 0.4781212$ m is the center of gravity of the blade and $I_{z_{blade}} = 0.0213$ kg m^2 is its moment of inertia around the z axis.

The next key point occurs when the released blade (RB) comes into contact with the trailing blade (TB)[2], as the latter has followed the initially imposed trajectory with minimal disturbances. This happens around t=2.199 ms, until which both the kinetic energy and internal energy of the TB remain constant. From this point until the next key moment, around t=4.5 ms (represented by the second rectangle in Fig. 3.19), interchanges of kinetic energy, internal energy, and friction between the two blades and between RB and FC take place. During this period, the pressure surface of the TB feeds kinetic energy to the RB through its motion, transmitting it through the contact and propelling it from the tip towards the FC. Friction between the parts increases during these moments, leading to plastic and elastic deformations in all deformable components.

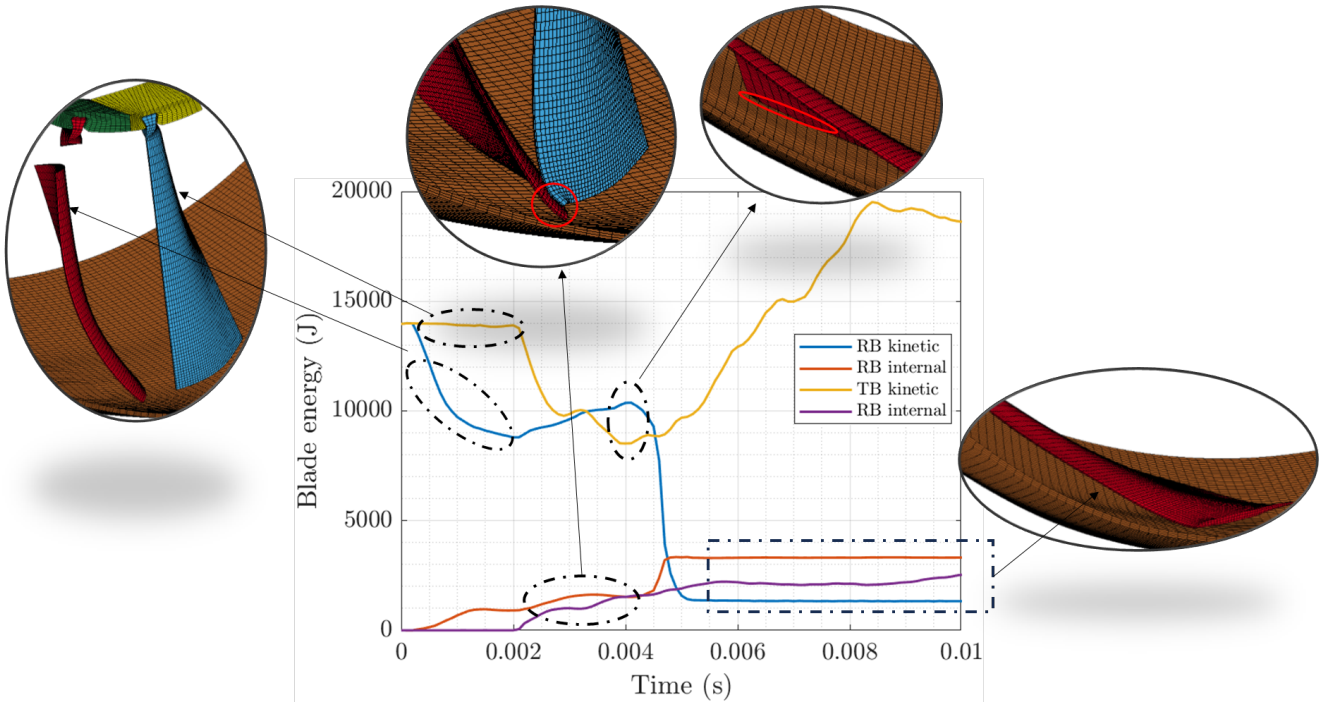

Figure 3.20: Case 6 blade energies and key events.

In Fig. 3.21, it can be observed that both the kinetic and internal energy of the FC gradually increase over time until the third key point (t=4.5 ms). At this moment, there is a global decrease in kinetic energy due to the sharp drop of the RB's velocity, as it is the moment when the trailing edge of the RB impacts the FC (third snapshot from the left in Fig. 3.20) and eventually the rest of the blade (fifth snapshot from the left in Fig. 3.19). From t=4.5 ms to t=4.89 ms, the FC experiences an approximately eight-fold increase in internal energy and up to four-fold increase in kinetic energy. All of this is reflected in the vibrations and resulting forces transmitted to the rest of the engine. Therefore, this is the most energetic impact and the one that, if it were to occur, could puncture the RB into the FC.

[2]These terms, i.e. FC, RB and TB, are instinctively used during the report to refer to the fan case, the released blade and the trailing blade, respectively.

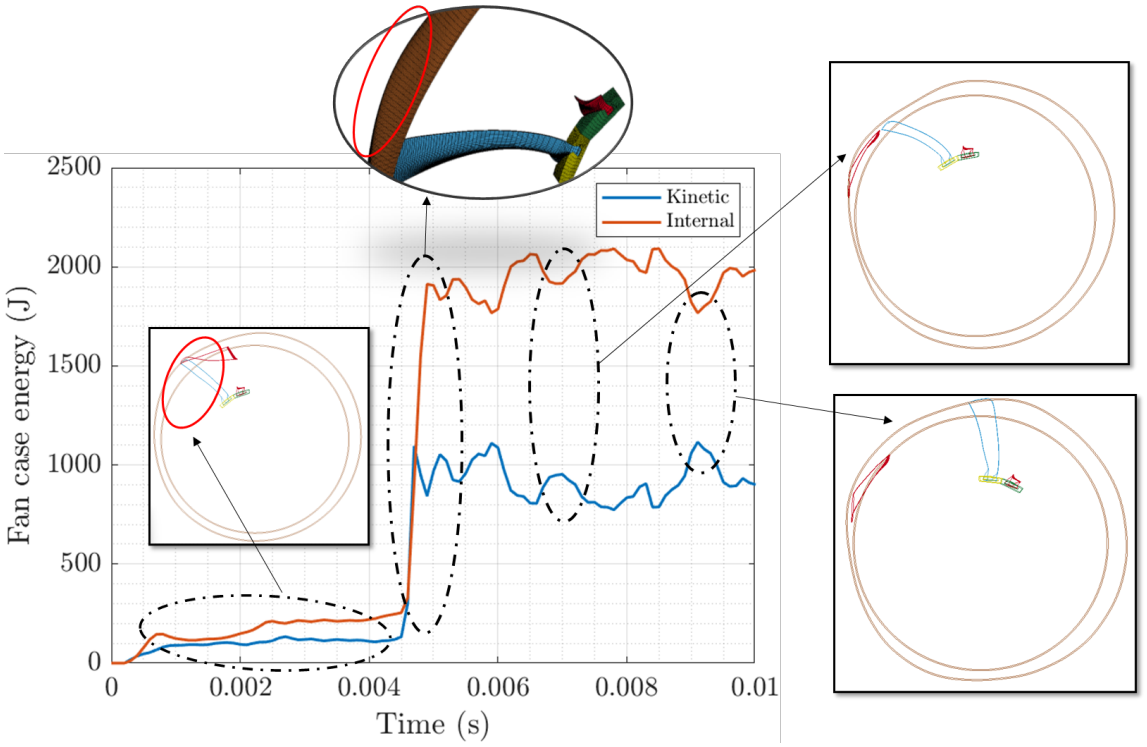

Figure 3.21: Case 6 fan case energies and key events.

From this moment, the blade's velocity is significantly reduced, and its direction is reversed towards the motor axis. At t=5.2 ms, the blade reaches its minimum velocity of 30 m/s, compared to a value of 136 m/s at the start. As a result of the reverse of direction, it separates from the FC and it is no longer in contact with it, similar to the TB, and the deformation and friction energies remain nearly constant. In this last part of the simulation (last dashed ellipse from the left in Fig. 3.19), the TB recovers and even surpasses its initial kinetic energy due to the motion induced by the rotor. The recovery of the elastic strain also plays an important role in the TB's increase in kinetic energy.

As for the FC, it can be deduced from the last two dashed ellipses from the left of Fig. 3.21, that the impact has caused nodal vibrations on the component, resulting in elastic deformations of the nodes that have acquired that velocity. Since no aerodynamic forces or damping have been introduced, it is expected that this pattern would remain constant over time if the simulation were run for a longer duration.

It is important to note that the sequence of events is slightly different if failure is considered, as some interactions do not occur. Furthermore, these results can vary significantly if the remaining blades and additional components are included, so the conclusions drawn are based solely on this simplified model.

Finally, a comparison is shown between the initial and final deformed configurations.

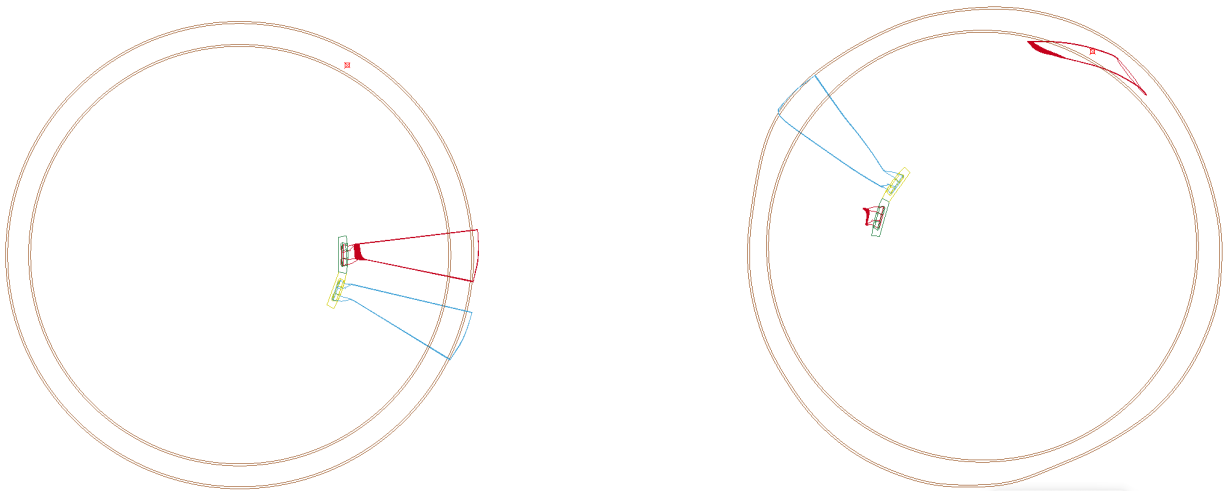

(a) (b)

Figure 3.22: Hard-wall containment model schematic at t=0 ms (a) and t=10 ms (b).

A more quantitative study of some of the aspects discussed in this section is carried out in Chapter 4 to evaluate the effectiveness of the proposed designs.

3.3.3 Analysis of results

Next, the results of the convergence study itself are presented. In addition to the study of global energies, component-level analysis, and other variables such as plastic deformation or stresses, the behavior of the model is also evaluated through visual analysis. This is particularly useful for identifying penetrations during contacts or non-physical modes of deformation such as hourglassing.

Although the graphs display data for all cases, only cases 2, 4, 6, and 8 are used for visual representations and other details. The purpose of this is to reduce the overall content of this report and only showcase the results that are considered most representative.

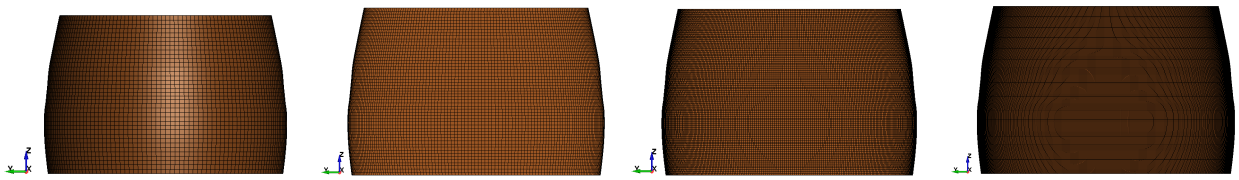

(a) (b) (c) (d)

Figure 3.23: Fan case meshes of cases 2 (a), 4 (b), 6 (c) and 8 (d).

Firstly, in order to study the resolution efficiency of the LS-DYNA model, the distribution of tasks as a percentage of the total CPU time provided by the software has been analyzed.

Approximately 55% of the time is allocated to element processing, while the contact resolution ranges from 35% for coarsely-meshed models to around 25% for finer meshes. From these data, it can be inferred that as the mesh is improved, a better distribution of contact forces emerges, making it easier for the system to resolve them. In other words, the simulation becomes more efficient.

On the other hand, another global aspect to consider is the value of the time step limited by the contact algorithm. This value is based, like the determination of the global time step, on the requirement that the time step should be smaller than the inverse of the highest frequency in the entire mesh. However, in this case, this frequency is calculated using the interface stiffness and the corresponding nodal mass. Therefore, LS-DYNA loops through all surfaces where contact has been defined in order to find the minimum value for this time step. The aim is to match this value with the global time step to ensure contact stability. If these two values differ significantly, contacts can become destabilized, leading to contact "pushing" that might destroy the stability and accuracy of the model.

In the current case, the minimum contact time step is 4.25e-08 s, while the global time step ranges from 2.36e-08 to 2.43e-08 s, falling within the same order of magnitude. This is sufficient for the contact algorithm being used. However, if, for example, the "tiebreak" type algorithm were to be used, this value should be much closer, and the scaling factor of the global time step, TSSFAC, could be adjusted to achieve that.

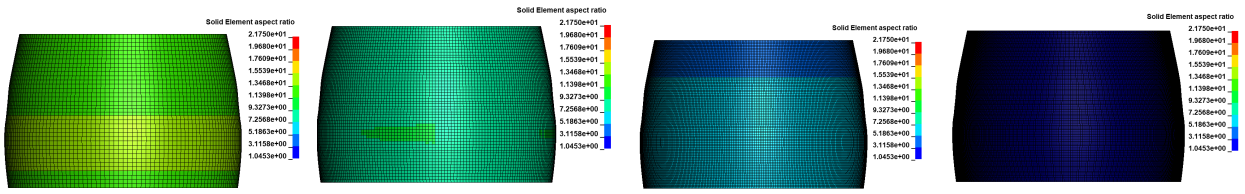

(a) (b) (c) (d)

Figure 3.24: Fan case meshes' aspect ratio of cases 2 (a), 4 (b), 6 (c) and 8 (d).

Note that in all cases the maximum time step is not limited by the elements of the fan case, but by those at the leading and trailing edges of the blades. Therefore, the refinement of the fan case do not affect the computation times by reducing the time step, but in the number of elements to process. On the other hand, regarding the element quality, it significantly improves as the meshes are refined, as depicted in Fig. 3.24.

Global system

Once the common simulation foundations are ensured, the convergence of the global kinetic and internal energies is studied, and their evolution is shown in Fig. 3.25a and Fig. 3.25b. As observed,

the kinetic energy converges effectively from case 4 onwards. The maximum difference between cases 6 and 7 is 0.6%, while between case 7 and case 8, it is around 1.01%. Considering the relative difference in the number of elements between these cases, with case 7 having 57% more elements than case 6 and case 8 having 155% more elements than case 7, it can be stated that case 6 sufficiently represents the kinetic energy of the simulation.

Regarding the internal energy, greater variation can be observed between the cases, particularly in the post-impact vibration zone. However, the more refined cases do not exhibit significant differences among themselves. The maximum difference between case 6 and case 7 is 2.4%, and between case 7 and case 8, it is 7.3%.

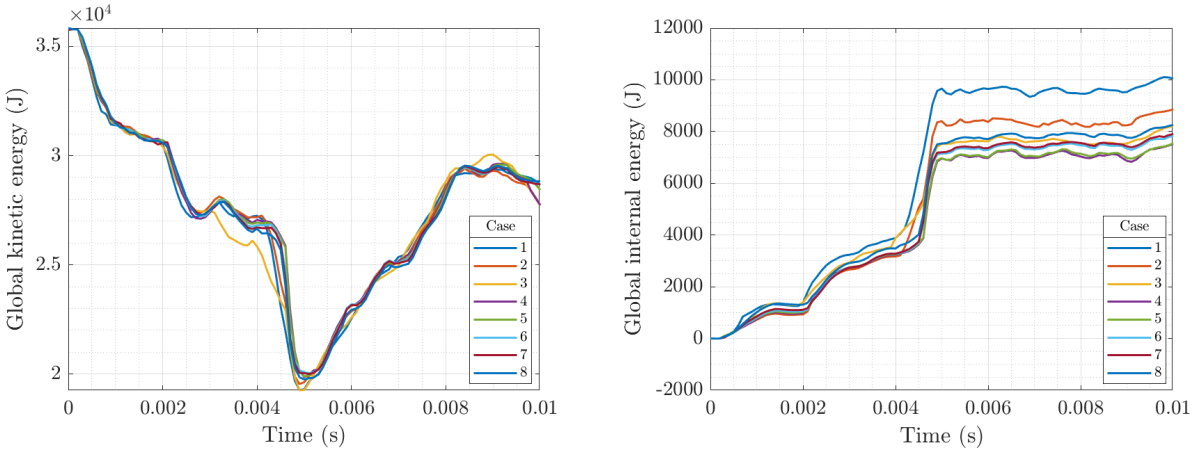

(a) (b)

Figure 3.25: Kinetic (a) and global (b) energies evolution of the complete model mesh sensitivity study.

To conclude the study of physical global energies, the behavior of the friction energy is examined. From the graph in Fig. 3.26, it can be observed that the convergence ratio increases as the mesh is refined. Additionally, starting from approximately Case 5, the obtained values are very similar, with maximum differences of 0.0875% between Cases 6 and 7, and 1.4% between Case 7 and 8.

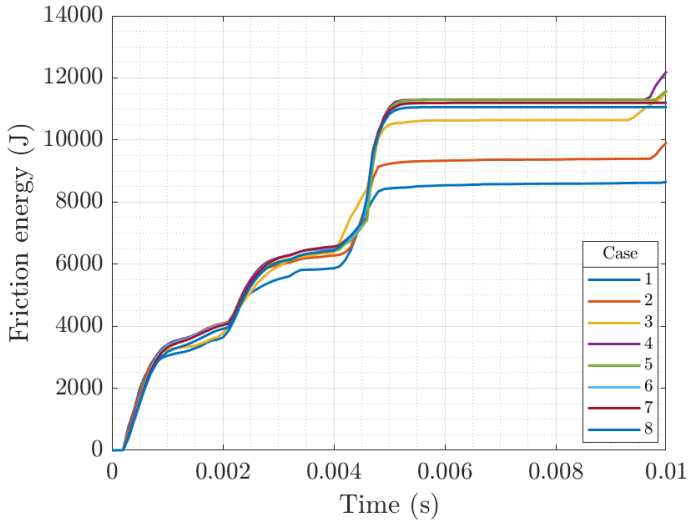

Figure 3.26: Friction energy evolution of the complete model mesh sensitivity study.

The only disparity worth discussing is the slight increase in the later stages of the simulation experienced by Cases 2, 3, and 4 (see Fig. 3.26). Upon studying the evolution of the contact forces, it has been observed that due to the deformation of the FC in those cases, starting from approximately 9.7 ms, there is rubbing between the TB and the FC, as seen in Fig. 3.27. In contrast, this does not occur in the more refined cases.

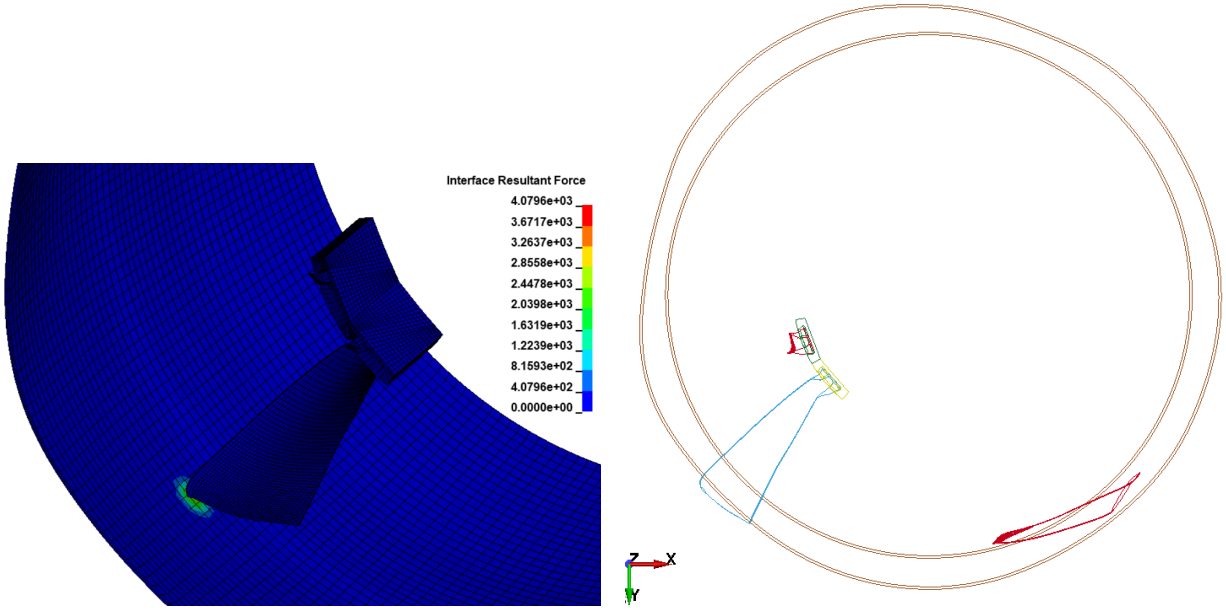

(a) (b)

Figure 3.27: Case 4 interface resultant force fringe plot (a) and schematic deformed complete model layout (b) at t=9.7 ms.

Regarding the energy ratio (Fig. 3.28), its values remain below the recommended limits throughout the entire simulation. Additionally, it can be observed that the greatest deviation occurs during the moments of impact between the RB and the FC. The explanation for this phenomenon is provided along with the FC energy converge study (later in this section).

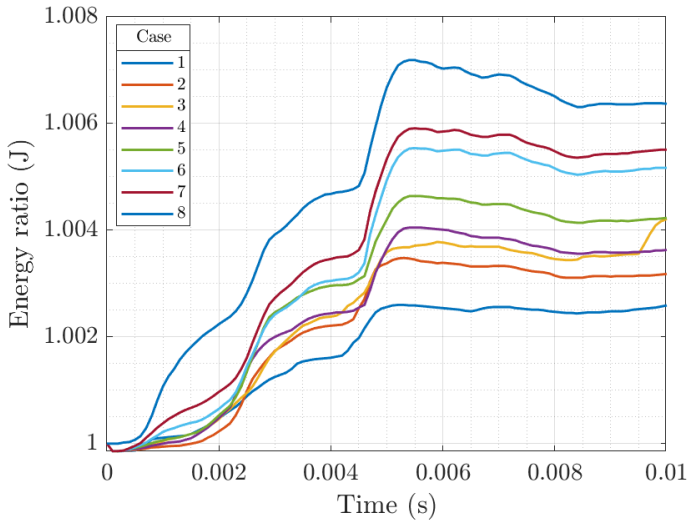

Figure 3.28: Energy ratio evolution of the complete model mesh sensitivity study.

For monitoring and controlling hourglass modes, several techniques have been employed. On one hand, displacements have been scaled in the visual representation of the solution to detect mild to moderate hourglassing that may not be visible with the default resolution. Since a very low hourglass factor has been used, it is important to ensure that, besides not introducing excessive non-physical energy, the value is sufficient to control potential spurious deformations.

Indeed, no zone with the characteristic mode of hourglass deformation has been found. Additionally, the evolution of the energy provided by the control algorithm has been monitored, and as indicated in Fig. 3.29a, ratios have been calculated with respect to the maximum internal energy in each case. The obtained results are in line with expectations. With refinement, the hourglass energy is significantly reduced globally. All values are well below the commonly adopted maximum limit of 10%.

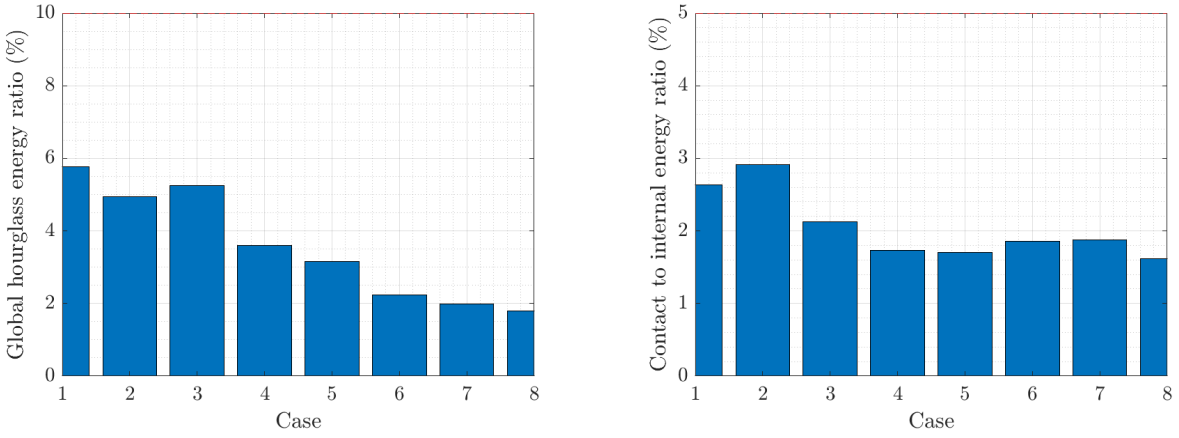

(a) (b)

Figure 3.29: Hourglass energy (a) and contact energy (b) to peak internal energy of the complete model mesh sensitivity study.

The contact energy follows a similar trend, being notably lower for finer meshes. Fig. 3.29b reflects how the software is able to resolve contacts more easily as the mesh resolution increases. The reason for this is that there are fewer localized contact loads, resulting in smoother nodal forces and displacements, and consequently less work being done. The maximum tolerable ratio for a generic case is usually around 5%.

Therefore, it can be observed that Case 6 presents good values for both, with a 2.24% hourglass ratio and approximately 1.8% for the contact ratio.

Blades

This brief section is dedicated to studying the behavior of the blades for the different cases considered. Although not subject to refinement in this part, the variation in the FC mesh also affects the obtained results for the blades. Since both blades follow a similar convergence pattern, only the data extracted from the RB is presented, as it requires special attention due to its role in the event.

Firstly, it can be observed that the evolution of kinetic energy is easily followed by all cases. Except for the moments immediately prior to impact, where it takes a bit longer to converge, they all collapse into the same curve. Maximum differences are around 0.1% between Cases 6 and 7, and 0.4% between 7 and 8. Moving on to internal energy, it has more difficulties in converging. However, among the cases of interest (6, 7, and 8), there is a maximum difference of 2.85%. Thus, for this range of refinement values, it can also be considered mesh-insensitive.

Lastly, it can be observed that the hourglass energy is vastly reduced and smoothed with refinement, reaching values below 2% of the peak internal energy of the blade.

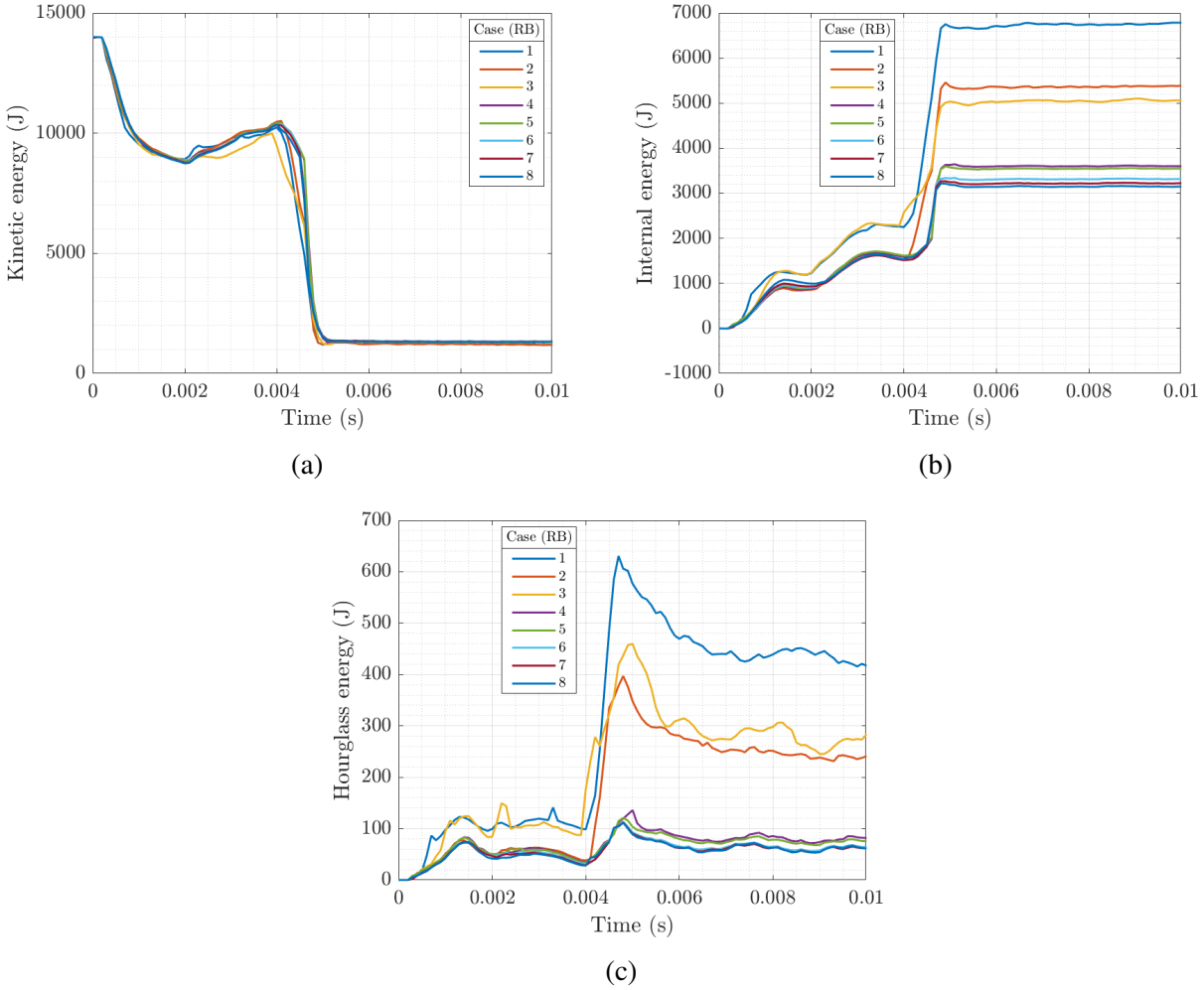

Figure 3.30: Released blade kinetic energy (a), internal energy (b) and hourglass energy (c) evolution for the complete model mesh sensitivity study.

Overall, the blades follow the expected patterns, and the obtained values fall within acceptable ranges.

Fan case

To conclude the mesh sensitivity study of the complete model, this section presents the data extracted from the simulations for the fan case component. Similarly to the previous cases, the corresponding energy graphs are discussed, and additional results are presented in case of obtaining unexpected or undesired behaviors.

Firstly, in Fig. 3.31a, the convergence of the fan case's kinetic energy can be studied. As in the previous cases, this variable seems to be relatively insensitive to mesh variations in the model. Although there is some dispersion in the free-vibration part, the data indicates that the maximum

deviations between cases 6 and 7 are 4%, and between cases 7 and 8 are 1.4%. It can also be observed that they follow a similar pattern in terms of shape.

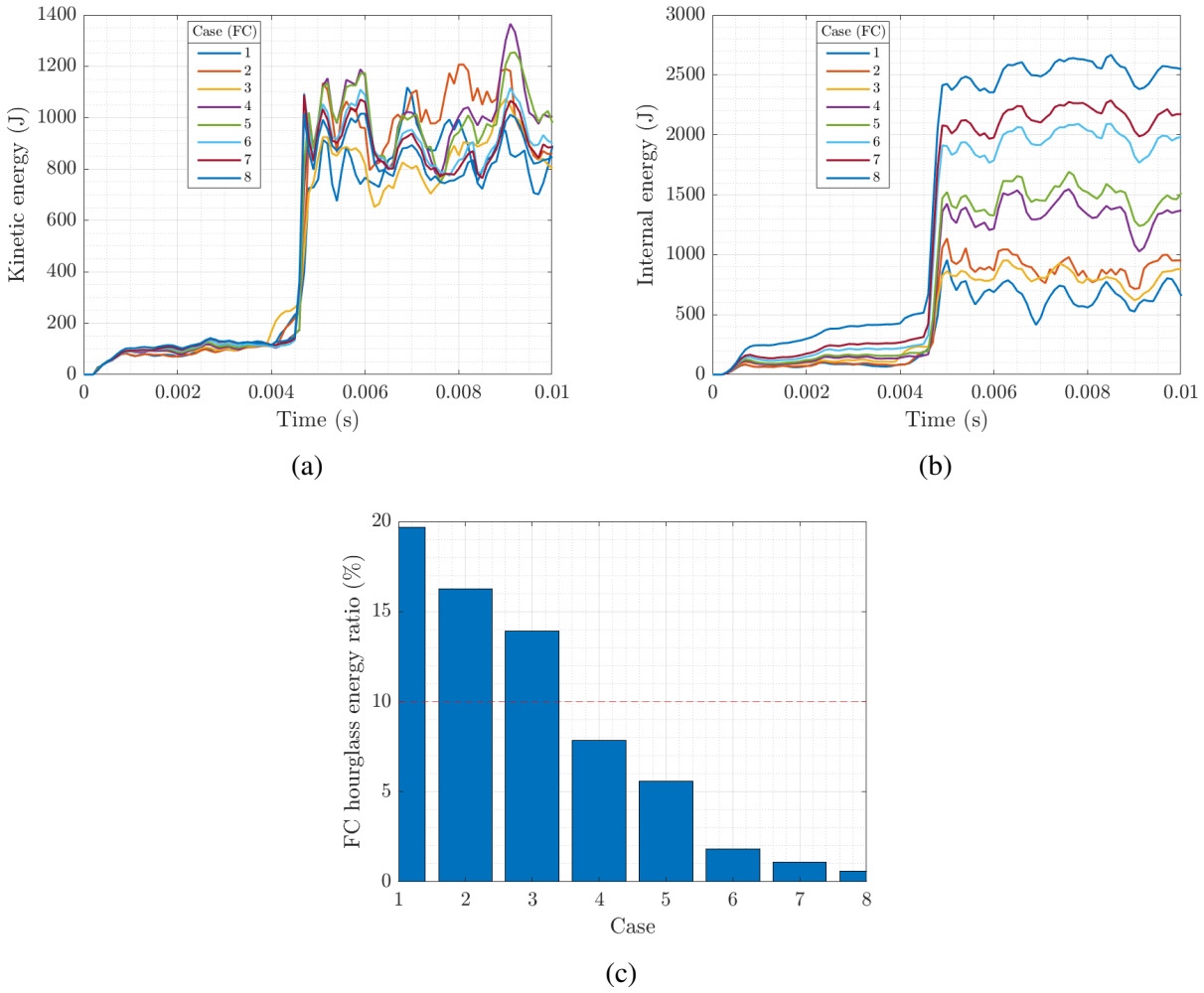

Figure 3.31: Fan case kinetic energy (a), internal energy (b) and hourglass energy ratio (c) evolution for the complete model mesh sensitivity study.

Regarding the hourglass modes, Fig. 3.31c shows that it is only from case 4 onwards that the obtained values fall below the admissible limit. Given the dimensions of the FC and the types of forces it is subjected to, where the impact is reduced to a small fraction of its surface, it is possible that these conditions trigger the appearance of these spurious modes to a greater extent. However, the reduction trend of hourglass modes is steep from the beginning, and the chosen case 6 only presents around 2%.

Next, Fig. 3.31b shows the evolution of the internal energy. In this case, it can be deduced from the figure that convergence is not achieved. The trend is as follows: as the mesh is refined, the internal energy increases, especially in the most critical instant where the blade completely

impacts the fan case and its velocity is reversed. Quantitatively, the maximum differences are 7.8% between cases 6 and 7, and 13% between cases 7 and 8. Although the vibration responses seem to follow the same shape, indicating similar computation of frequencies, the magnitude of the value around which they oscillate (maximum plastic deformation achieved) is significantly increased. This scaling of internal energy can be attributed to the forces causing the derived deformations.

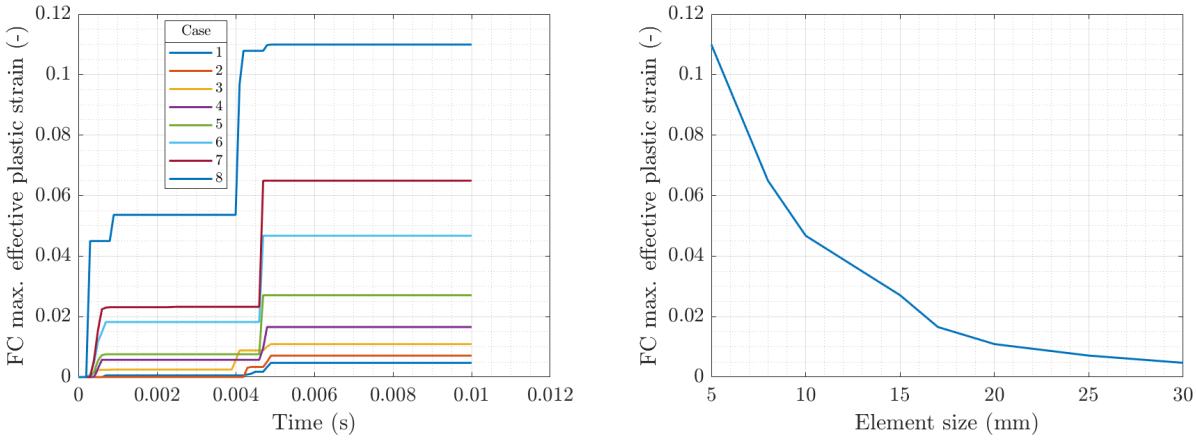

(a) (b)

Figure 3.32: Fan case maximum effective plastic strain time evolution (a) and as a function of the element size (b).

To study in more detail the phenomena leading to the non-convergence of the fan case's internal energy, the graphs in Fig. 3.32 are presented. In these plots, it can be observed that as the element size is reduced (or the number of elements increases), the maximum effective plastic strain of the component exponentially increases. Furthermore, Fig. 3.32a follows a very similar shape to the FC internal energy, also showing this predicted divergence in the plastic strain. This confirms the reason for the increase in internal energy.

A plausible explanation for this behavior is the high localization of contact forces during the second impact of the RB on the FC. Fig. 3.33 represents the resulting contact forces in a section of the FC for the indicated critical times. On one hand, the top row corresponds to Case 4, where it can be observed that the contact force values are higher, but the affected area also occupies a larger surface. On the other hand, the bottom row represents the same for Case 6, and in this case, the forces decrease in magnitude but the surface is much more localized.

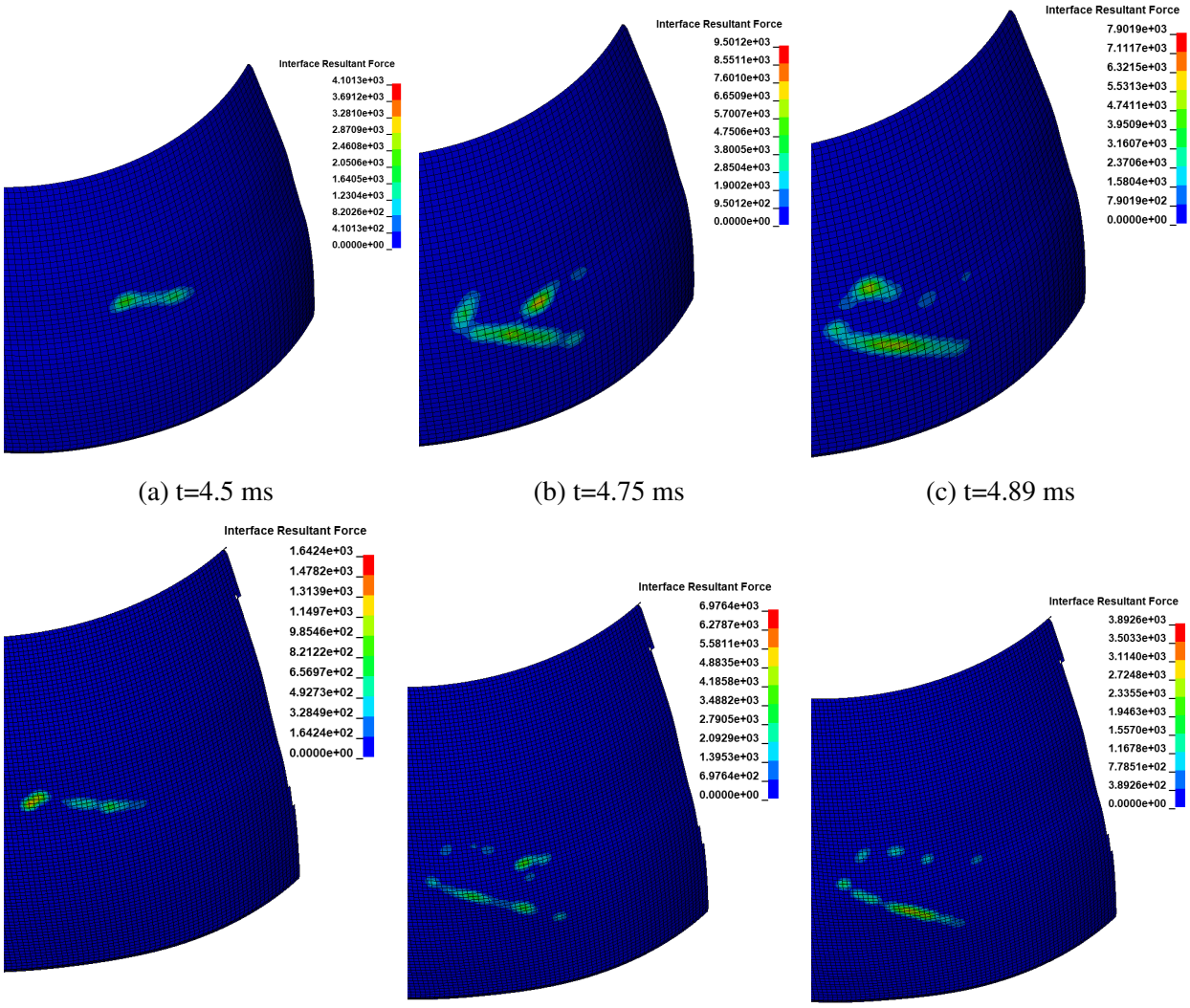

(a) t=4.5 ms (b) t=4.75 ms (c) t=4.89 ms

(d) t=4.5 ms (e) t=4.75 ms (f) t=4.89 ms

Figure 3.33: Case 4 (a), (b), (c) and case 6 (d), (e), (f) interface resultant loads at indicated times.

Therefore, this contact interaction may be leading to a stress singularity. Concentrated forces in FEA are widely undesirable as they can lead to these convergence problems and in most cases they require extremely fine meshes to properly distribute the load amongst several nodes. As mentioned in Section 3.3.1, the possibility of locally refining the areas affected by this surface force concentration has been considered, but it has not resulted a practical solution for the present work.

As a consequence, it has been decided to accept this limitation for the constructed model, acknowledging that a much finer mesh would be necessary to resolve the contact forces in that area, and leaving this task for future improvements.

3.3.4 Conclusion

In conclusion, considering all the factors discussed in this section of the mesh sensitivity study, Case 6 has been identified as the optimal mesh option. The comprehensive convergence analysis, encompassing global energy parameters, component-level behaviors, and visual assessments, supports this selection.

The quantitative analysis of energy parameters demonstrates that Case 6 exhibits stable convergence with minimal deviations compared to other mesh configurations. Additionally, the visual analysis helps identify potential issues such as contact penetrations and hourglass patterns, ensuring the model's accuracy in capturing the desired physics.

Furthermore, Case 6 offers a favorable trade-off between model rigor and computational efficiency. It strikes a balance between capturing the necessary details and minimizing CPU time, making it a practical choice for simulations. Despite the acknowledged deficiencies in the model, it can serve as a benchmark for conducting preliminary studies, providing valuable insights and guiding further improvements.

The findings from this study lay the groundwork for enhanced modeling performance and more reliable predictions in subsequent analyses.

3.4 Model Improvement

This section introduces a new phase of the study aimed at improving the accuracy of the predictions of Case 6 without significantly compromising computational resources. The focus lies on optimizing the element density distribution across the thickness of the fan case. The objective is to evaluate the relative advantages of three different configurations: Case 6 with three elements, along with cases employing four and five elements, respectively.

Furthermore, this section explores the impact of introducing failure as a proof of concept and assesses the potential implications on the results when elements experience erosion upon failure occurrence. These investigations provide valuable insights into the behavior of the model under failure conditions.

The primary goal of this section is then to develop a simulation model that is sufficiently tailored for the intended analyses. Emphasis is placed on computational speed while maintaining a robust yet streamlined numerical approach. This strategic focus enables swift simulations, facilitating the study of various design aspects and facilitating prompt model modifications.

The forthcoming analysis presents the findings and observations derived from this section,

contributing to the enhancement of the simulation model.

3.4.1 Consideration of fan case thickness refinement

As previously mentioned, the use of underintegrated elements entails several advantages but also some drawbacks, including the need for additional refinement in certain areas. The purpose of this refinement is to better capture certain modes of deformation, as a single integration point per element may limit this capability when deformations are highly nonlinear. Hence, both the blades and the fan case consist of at least three elements throughout their thickness.

Given that the fan case is the structural element under investigation, the potential benefits of introducing more elements in this direction towards an accurate representation of results are to be examined. Table 3.4 provides a summary of the data related to the element count and computation time for each case. The cases are labeled according to the number of elements through the thickness, hence case 3, 4, and 5. It is observed that for case 4, with 33% more elements, the computation time increases by only 9 minutes.

Case	**3**	**4**	**5**
Number of elements	108927	145236	181545
CPU time (min)	73	82	100

Table 3.4: Model improvement cases 3, 4 and 5 characteristics.

Deterioration in element quality is another factor to consider since refinement in the transverse direction leads to thinner elements and, consequently, higher aspect ratios. In case 4, the aspect ratio remains similar to that of case 3 (around 5), but for case 5, it falls within the range of AR=5-7.

As for the global energies, the three cases yield very similar results, hence their presentation is deemed unnecessary. The three curves collapse into one, indicating that no significant variations in the global system are obtained from one case to another.

On the other hand, the study of fan case energies can be performed using Fig. 3.34. From this plot, it can be inferred that the most notable differences are observed in the vibration zone, where even the pattern slightly changes. This can be attributed to an improved representation of radial stiffness of the fan case through the introduction of more elements, as its mass remains invariant for all three versions.

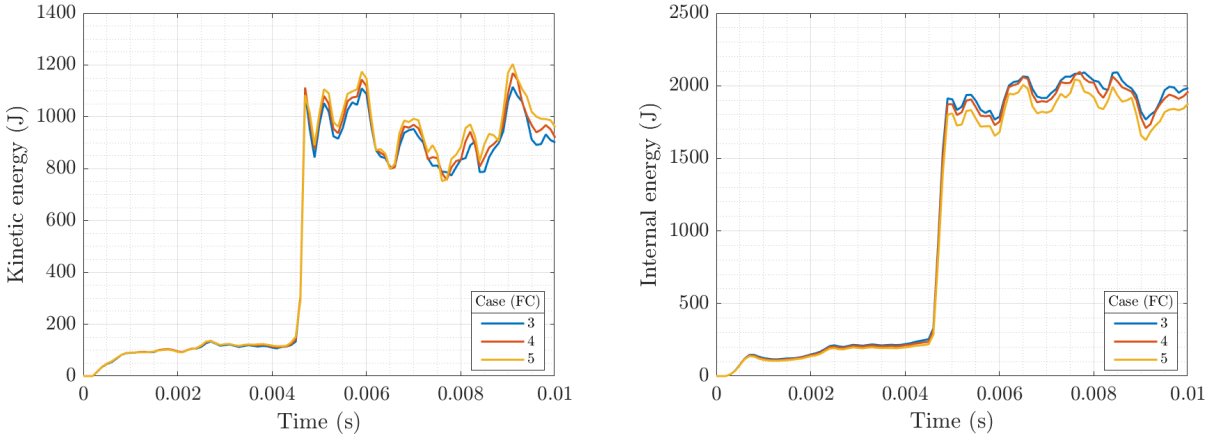

(a) (b)

Figure 3.34: Fan case kinetic energy (a) and internal energy (b) evolution for the complete model mesh improvement.

Quantitatively, the maximum difference observed, between case 3 and 5, is 5.6%, and between case 3 and 4, it is 0.4%. This indicates that, at least within the range of elements considered for cases 3 and 4, the results are not highly sensitive to the mesh density.

Regarding non-physical energies, a slight increase in the hourglass ratio, especially in the fan case, and a slight decrease in the contact ratio are observed. In both cases, these are mild evolutions that neither provide a significant advantage nor a detriment to the results under consideration.

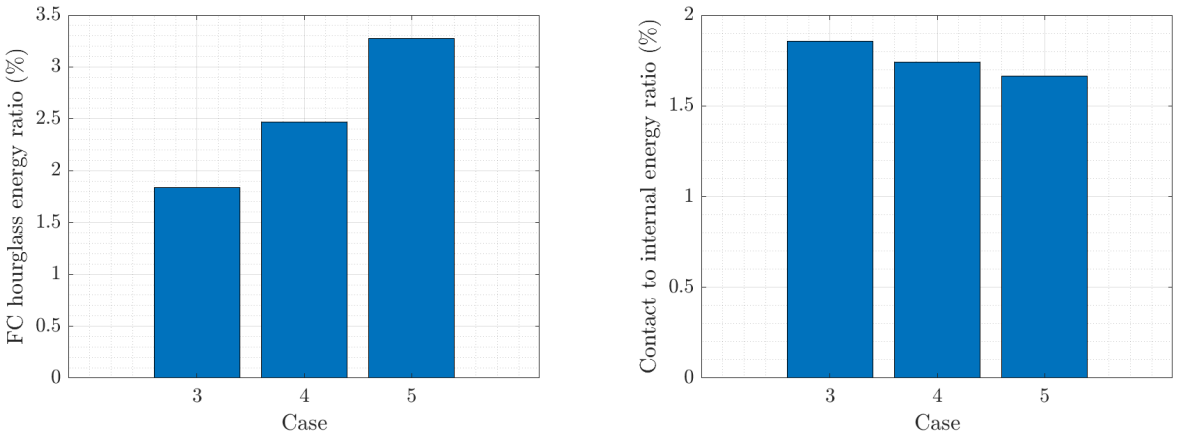

(a) (b)

Figure 3.35: Fan case hourglass ratio (a) and global contact ratio (b) for the complete model mesh improvement.

Finally, the results corresponding to the deformations experienced by the fan case are presented. The objective is to assess whether the predicted trends towards change in displacement

representation are being met. Fig. 3.36 presents a representation of the bulge and other deformations caused by the second impact of the blade at the most critical instant (t=4.9 ms). It can be observed that as more elements are added, more elements deform in the highly loaded regions, where the bulge occurs. Therefore, as anticipated, the displacement distribution changes significantly, while the difference in values between cases 4 and 5 is not extremely pronounced.

During the analysis, it is observed that the stress state in the same region undergoes minimal changes when adding elements through the thickness. Thus, it can be concluded that the most noticeable difference lies in the representation of displacements in the most deformed regions.

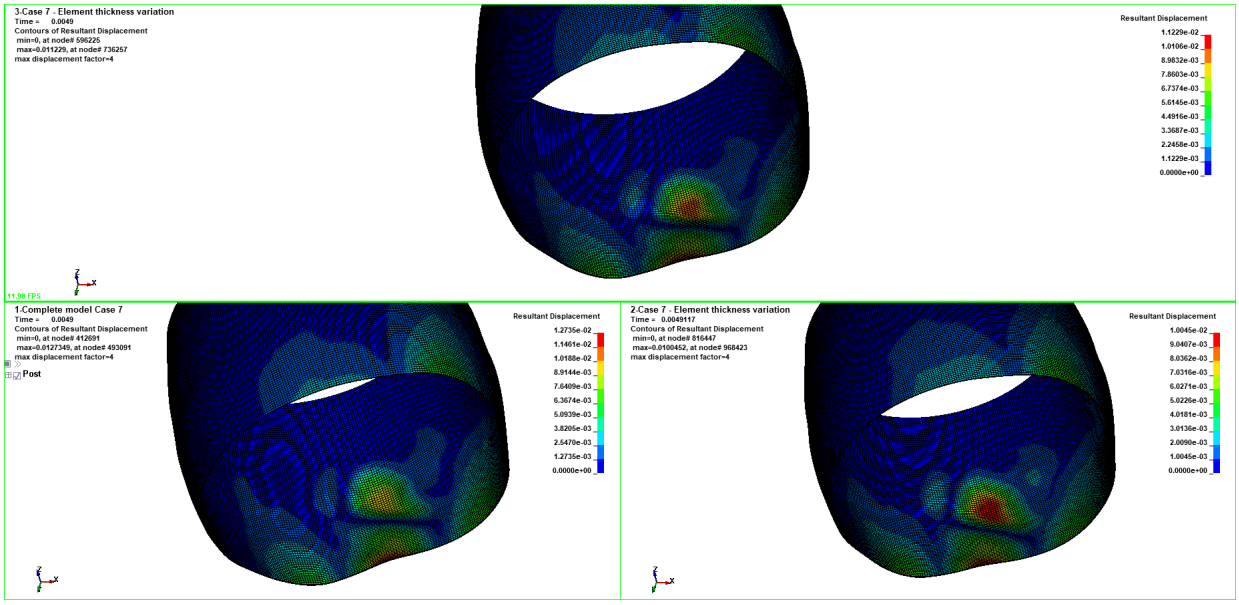

Figure 3.36: Case 4 (above), case 3 (left-bottom corner) and case 5 (right-bottom corner) displacements representation. The displacements have been amplified x4 and the results are for t=4.9 ms.

From the presented results, the conclusion can be drawn that, despite not exhibiting dramatic differences, the case with four elements through the thickness is optimal in this scenario. It provides a greater detailed mesh compared to the minimum element count of 3, without a substantial increase in CPU time. Furthermore, it does not excessively deteriorate element quality, and given the prospect of altering the thickness magnitude of the fan case, introducing more elements could further worsen its quality, as well as potentially affect the time step, further reducing it.

Furthermore, considering that deformations expected for smaller thicknesses will have a higher nonlinear component, it is anticipated that having an additional integration point available to represent them might be advantageous in such cases.

Finally, it is important to emphasize that the obtained results are not validated, and therefore, no comments can be made regarding the accuracy with which the model predicts the deformations

and stresses of the actual system. This discussion is based on numerical knowledge, trend analysis, and data interpretation. Thus, it serves as a proposal for further in-depth analysis, incorporating the necessary validation and verification of results through experimental tests.

3.4.2 Conclusions

In conclusion, the study focused on evaluating the effects of refining the mesh through the thickness of the fan case with 3, 4, and 5 elements. The objective was to identify the optimal number of elements that balances computational efficiency and accurate representation of results.

The results indicated that increasing the number of elements in the FC thickness led to improved results distributions, particularly in regions with higher loads where bulging occurs. While the analysis of stress states in the FC region showed minimal changes, the distribution of displacements varied significantly as more elements were added. Therefore, it can be deduced that the most noticeable difference between the cases lies in the representation of displacements in highly deformed regions.

Considering the trade-off between computational efficiency and element quality, the choice of 4 elements through the FC thickness emerged as the optimal configuration. This choice provided a better refinement compared to the minimum of 3 elements, without jeopardizing the quality of the solution, as the aspect ratio remained similar to that of the 3-element case.

It is important to note that the results presented in this study are based on numerical analysis and trends, and they have not been validated against experimental data. Therefore, further validation and verification efforts are necessary to confirm the accuracy and reliability of the selected mesh configuration.

To sum up, the decision to use 4 elements through the FC thickness strikes a balance between computational efficiency and element quality, offering an improved representation of deformations without compromising the overall simulation speed. This choice provides a suitable model for studying various design scenarios and allows for easy modifications.

3.5 Failure

To conclude this chapter, the results of the model that includes failure are presented. The introduction of this feature is achieved through the material model, specifically the effective plastic strain to failure. This represents a failure criterion that, unlike failure models, does not couple stresses and damage. Therefore, it is useful when the focus is on "**when**" failure occurs rather than "**how**" it occurs. When an element reaches the established limit, it is removed from the mesh.

The effective plastic strain at which a metal fails depends on the type of loading. For example, the shear strain for failure is usually lower than tensile strain, and metals do not fail under moderate hydrostatic pressure. Other factors that can influence failure behavior include temperature, test geometry, and strain rate [16]. Due to the triaxiality, complexity, and scarcity of the event being simulated, there is no reliable numerical parameter available. Consequently, the failure point of the introduced constitutive model's tensile failure is employed as the criterion. For the Al2024-T3 this is $\bar{\varepsilon}_{pl} = 0.12$ and for Al7075-T6 is $\bar{\varepsilon}_{pl} = 0.099$

It should be noted that the employed material model can predict compression failure if the specified value is reached, which is unrealistic and should be considered as a limitation.

3.5.1 Results

To illustrate the differences, the results corresponding to case 6 with 3 elements through the FC thickness are shown. Snapshots of the simulation with failure are included to complement the explanation of the graphs. In general terms, similar patterns are obtained, except in certain sections where failure occurs.

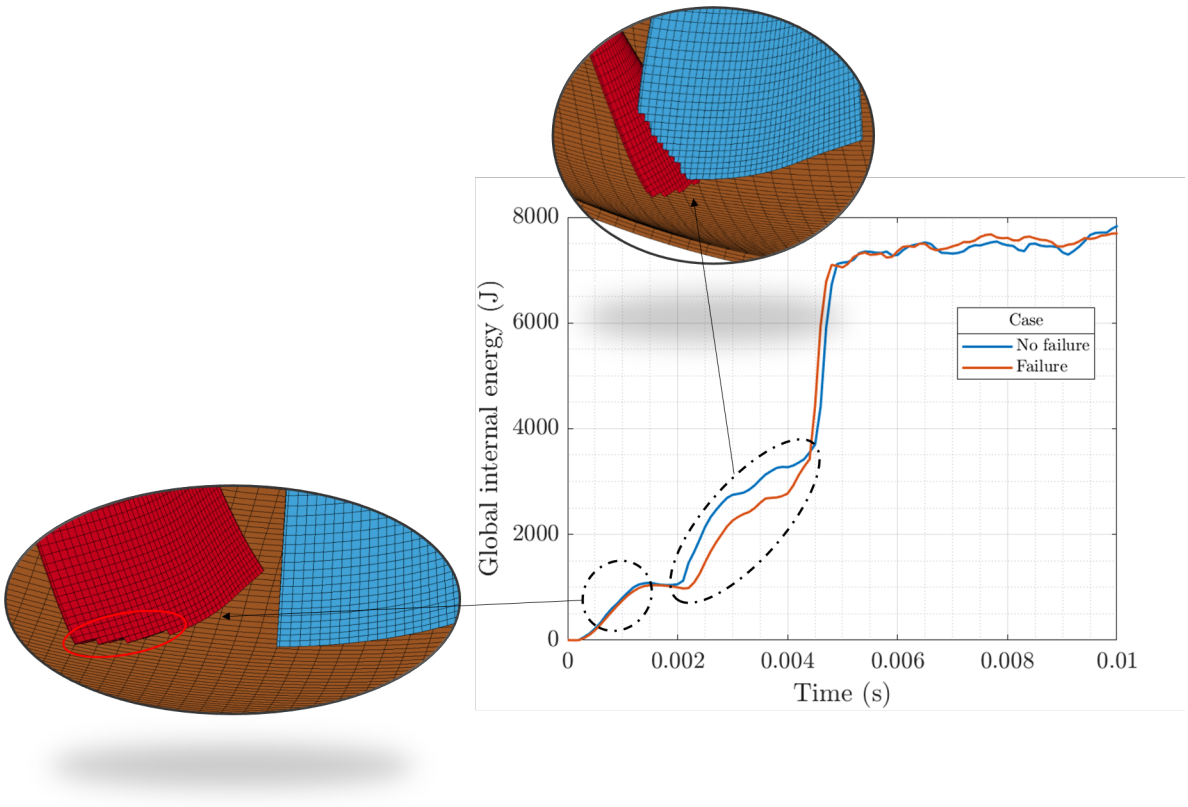

Figure 3.37: Internal energy's time evolution for case 6 with and without failure.

Firstly, Fig. 3.37 shows the differences in internal energy between both cases. In the initial

moments after the first impact, the internal energy is slightly lower than in the non-failure case. A potential reason for this, which applies to the rest of the related results, is that when failure is reached, the element is removed, and that can result in some springback in the neighboring elements. Consequently, the stored energy in the mesh is lower, and the behavior of the simulation can vary.

During the period when the TB pushes the RB, due to the same reasons, smaller deformations are attained. It should be noted that this process is particularly aggressive for the TB, as the simulations without failure exhibit significant deformations occurring at its tip.

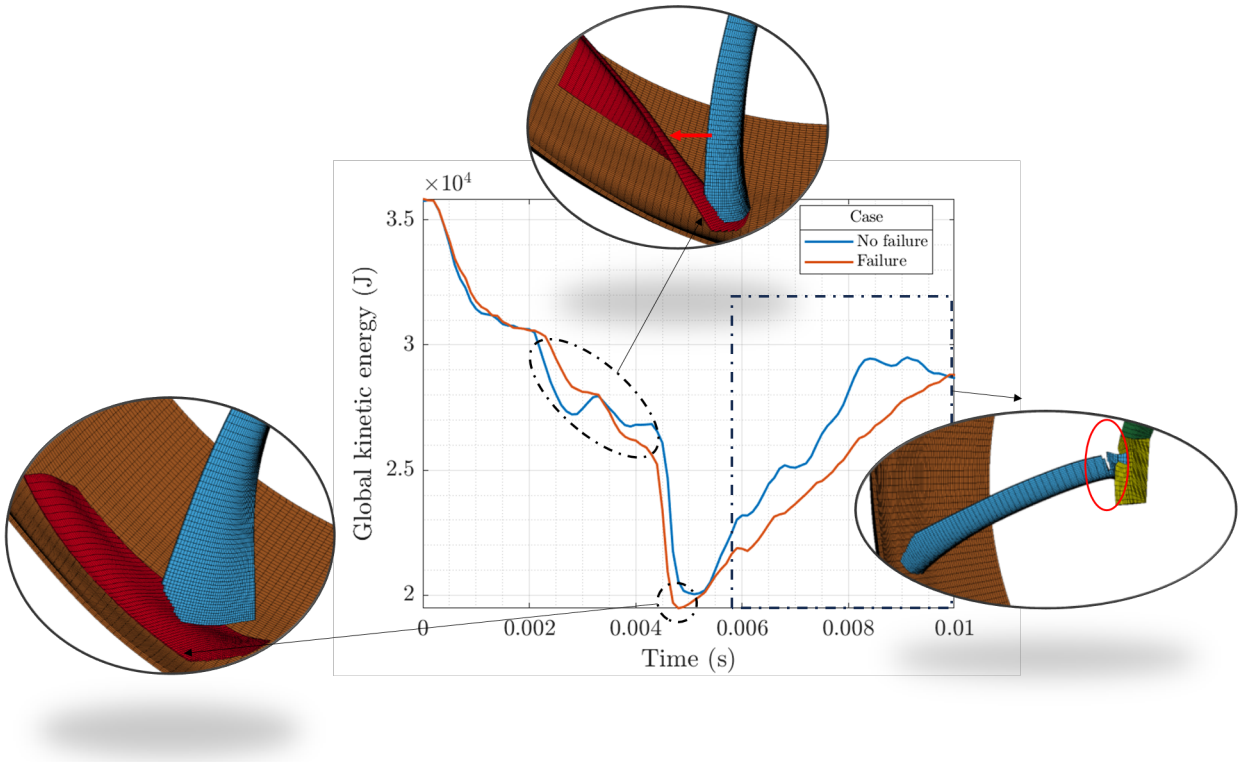

Figure 3.38: Kinetic energy's time evolution for case 6 with and without failure.

Regarding kinetic energy, this variable appears to differ more from the baseline case. During the first phase indicated in Fig. 3.38, in the case of failure, the TB acts more forcefully, reducing the RB's velocity by trapping its tip between the TB and the fan case, resulting in a lack of the initial increasing trend. As for the second impact, it occurs slightly earlier, and the minimum kinetic energy (t=4.7 ms) is lower.

Lastly, there is a change in the physics of the problem as, in the latter part of the simulation, the TB starts to fracture at its root due to the previous impacts and interactions. This is definitely something to consider, as the loss of the other blade can trigger even more catastrophic effects.

Regarding the other energies, such as friction, contact, or FC hourglass energy, they all exhibit similar values and trends, so they have not been included in this explanation.

Finally, the final state of the model and the deformations in the bulge area are shown. Fig. 3.39 and Fig. 3.40 depict the differences in displacements and stresses between the two models.

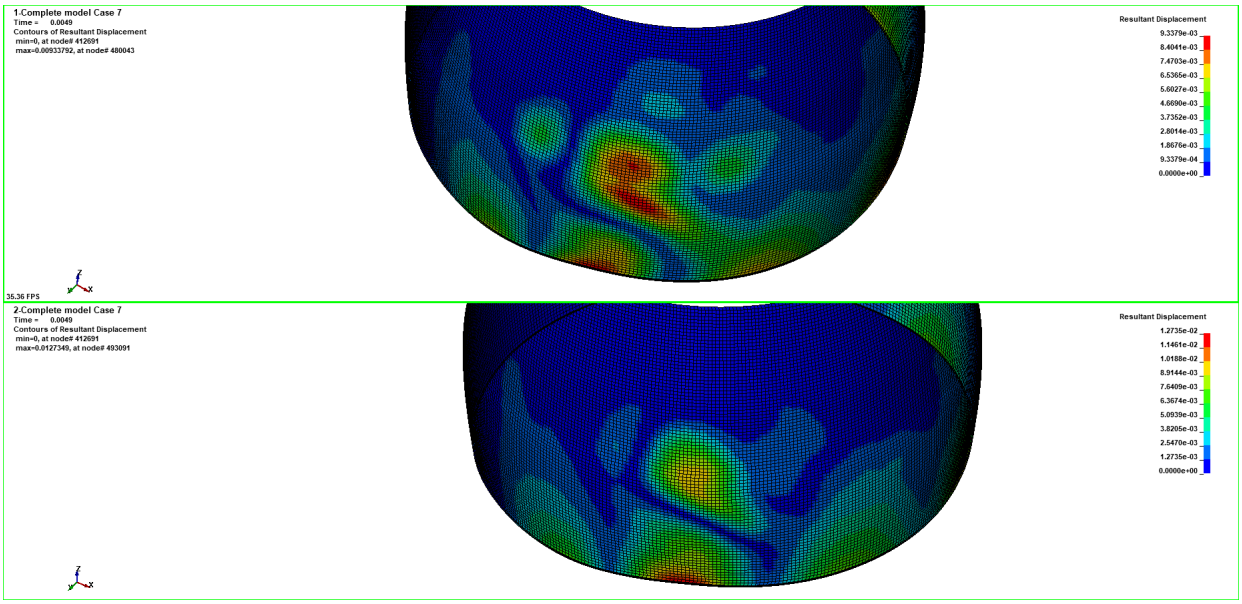

Figure 3.39: Resultant displacement fringe plot for case 6 with failure (top) and without failure (bottom) at t=4.9 ms.

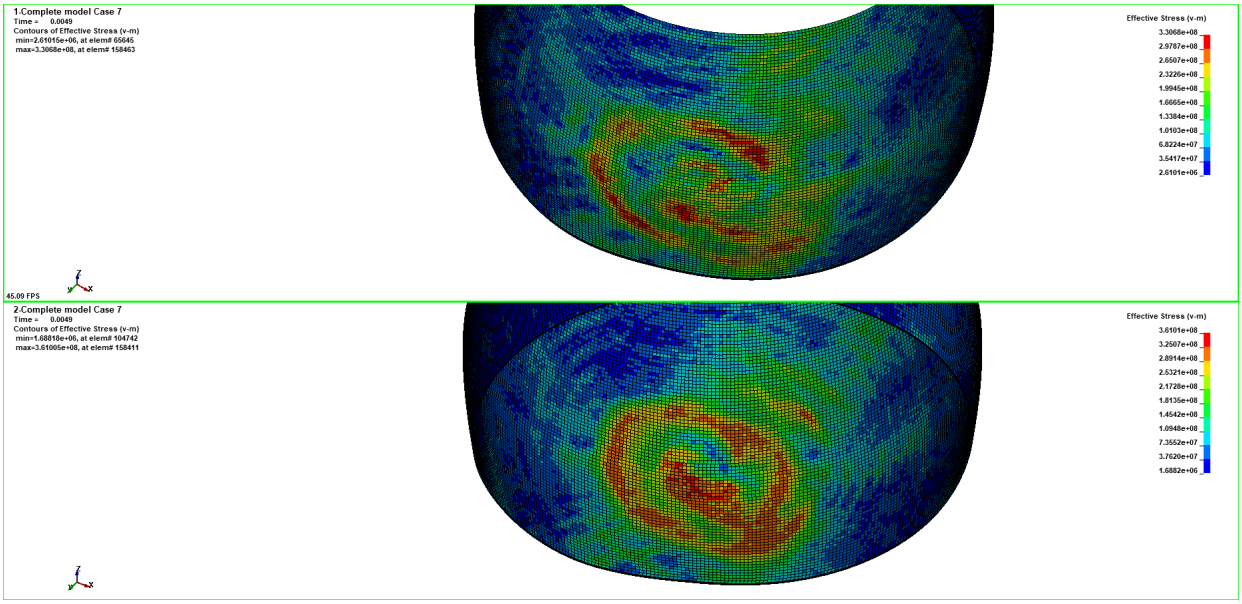

Figure 3.40: Effective stress fringe plot for case 6 with failure (top) and without failure (bottom) at t=4.9 ms.

Ultimately, Fig. 3.41 includes a result from the mesh sensitivity study for the model with

failure. In this figure it can be seen that as the mesh becomes more refined, i.e. the element size becomes smaller, the volumetric fraction of elements removed after failure becomes smaller. This behaviour is in line with expectations because as the element size is reduced, the failure is localised to a greater extent, and the volume of eroded elements is also smaller due to their reduced size, resulting in a lower volumetric fraction of failed elements. Therefore, it can be deduced that it is difficult to confirm the convergence of results on the basis of the available data, which are not conclusive.

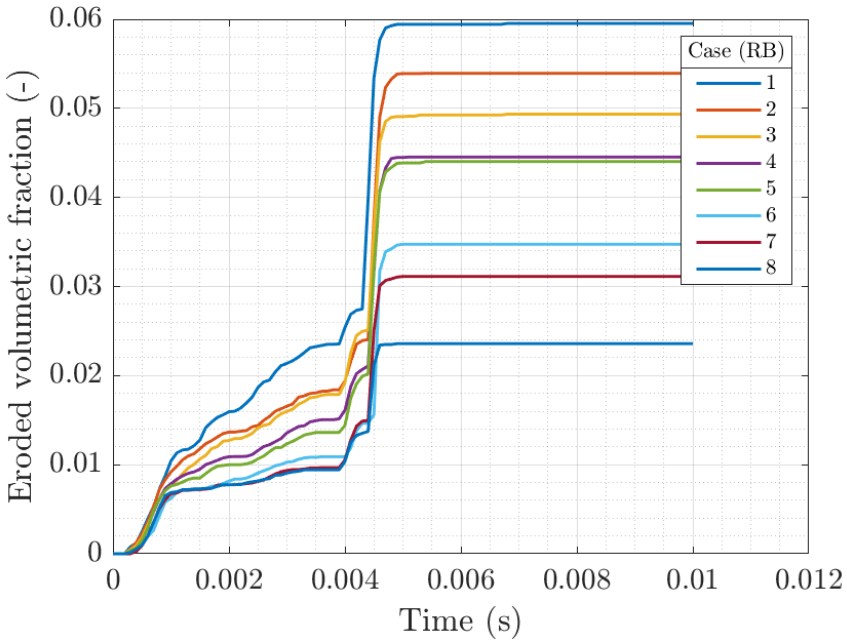

Figure 3.41: Mesh sensitivity study of blade volumetric eroded fraction of elements evolution with time.

Thus, this section has demonstrated the possibility of constructing a sound model by considering a simple failure criterion. However, the accuracy of the obtained results relies on the calibration and tuning of the model with respect to the real system. Consequently, as mentioned above, the correct inclusion of the failure criterion would require a more exhaustive and systematic study and empirical data for comparison.

3.5.2 Conclusion

In conclusion, the results presented in this section demonstrate the feasibility of incorporating failure into the model. By introducing the effective plastic strain to failure of the tensile test as a failure criterion, the model is able to capture the occurrence of failure in the structural components.

By comparing the results of the model with failure to the non-failure case, noticeable dif-

ferences were observed. In terms of internal energy, the presence of failure led to slightly lower values due to the removal of elements when failure occurred. Deformations during the interaction between components were also reduced, especially for the blades experiencing failure, resulting in a modified energy transferring pattern.

Kinetic energy exhibited differences between the cases, with the failure case showing a decreased minimum kinetic energy during the second impact. Moreover, the simulation highlighted the occurrence of fracture in the blade root due to previous interactions, emphasizing the importance of considering the potential cascading effects of blade loss.

The final analysis focused on the comparison of displacements and stresses in the bulge region, revealing variations between the models. These findings further emphasize the impact of failure on the structural response and provide valuable insights into the behavior of the system under failure conditions.

It is essential to acknowledge that the results obtained from the model are not validated. While the model provides a reasonable approximation, it is crucial to consider its limitations, for which it may not align with real-world behavior. Future work should involve rigorous validation and verification using experimental tests to ensure the model's reliability in predicting deformations and stresses in real-world scenarios.

In summary, this section serves as a "proof of concept" for incorporating failure into the model using a simple failure criterion. While the model shows promising results, its accuracy relies on further refinement and advancement of its features. By considering the suggested mesh sensitivity study, it is evident that refining the mesh leads to improved failure predictions, highlighting the importance of element size in capturing the failure behavior accurately.

Chapter 4

Fan Case Dimensioning and Optimization

This final chapter focuses on the process of dimensioning the fan case, which is the ultimate objective of this MSc thesis. The design objective is centered around optimizing this component to minimize its mass while ensuring its structural integrity. In Section 4.1, the analysis process and the characteristics of different model variations are detailed.

Subsequently, trends in behavior are evaluated (Section 4.1.1), and a thorough assessment of the simulation quality is conducted (Section 4.1.2). Finally, the chosen optimal case is presented in Section 4.2, and relevant results for subsequent design considerations are analyzed, including deformation levels, containment capacity, and forces transferred to the rest of the engine after impact.

4.1 Design Variations for Fan Case Thickness

The study has been carried out by varying the thickness of the fan case of the model chosen in Chapter 3, i.e. Case 6 with four elements through thickness. The variations were made in 0.5 mm decrements up to 2 mm, resulting in a total of 9 cases, including the baseline with its initial 6 mm thickness. The rest of the simulation conditions were kept the same as the baseline model unless otherwise stated. Table 4.1 presents the FC thickness values for the different cases along with the mass of this component. As mentioned before, the mass will be a crucial factor in the selection of the recommended final model.

Case	1	2	3	4	5	6	7	8	9
Fan case thickness (mm)	6	5.5	5	4.5	4	3.5	3	2.5	2
Fan case mass (kg)	63.2829	57.9915	52.6947	47.4031	42.1163	36.8345	31.557	26.2388	21.018

Table 4.1: Fan case thickness variation design cases' characteristics.

It is important to note that since this is a highly simplified model, the decisions made and the resulting recommendations only apply to this case. Therefore, it is essential to emphasize that the obtained results and conclusions may vary significantly when compared to the real model or a more advanced analysis.

For example, the inclusion of a greater number of blades or a failure model could potentially change the design given that the events would occur differently. Hence, the value of this study lies in proposing a logical and efficient methodology to evaluate the containment capability of a fan case design, rather than solely relying on quantitative results.

4.1.1 Introduction to design cases

In this work, the effectiveness of the fan case is evaluated based on three aspects:

1. Speed of the released blade before and after impact.
2. Level of deformation.
3. Containment capacity.

Firstly, the aim is to maximize the decrease in speed of the released blade due to the impact. Additionally, it is necessary to study the degree of deformation experienced by the fan case, as it is crucial for maintaining its structural integrity. Especially for thinner cases, it is possible that the fan case does not fail after impact but deforms in a way that its interaction with the rest of the blade cascade results in an even more severe FBO event. Lastly, the fan case's ability to contain the blade within the engine, thus avoiding further damage to other structures, is evaluated.

Therefore, the first variable to evaluate is the temporal evolution of the rigid-body velocity of the released blade for the different design cases, as shown in Fig. 4.1. This graph highlights the behavioral differences among the different models and serves as the initial criterion for identifying the optimal case.

It is important to note that in this speed measurement, the rotational velocity of the dovetail

of the released blade, which remains attached to the platform, is also included. Nevertheless, this variable is still useful as it is solely employed for comparative purposes. As observed, most cases, from 6 mm to 3.5 mm, collapse along the same curve. However, it is from case 7 (3 mm) onwards that certain relative advantages start to appear.

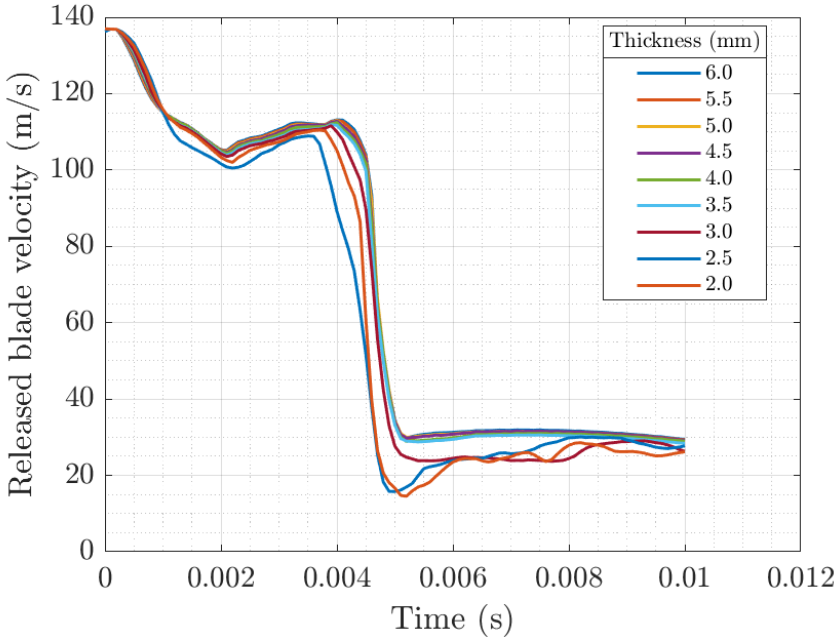

Figure 4.1: Rigid-body velocity time evolution of the released blade for the different design cases.

Analyzing the trends, this graph indicates that the thinner the FC, the greater the reduction in the speed of the released blade. The relative reductions in comparison to the initial velocity are 78.69%, 81.2%, 88.4%, and 89.3% for cases 6, 7, 8, and 9, respectively.

This is a positive aspect since reducing the thickness also results in a reduction in the FC mass, which, starting from case 7, is over 50% less than the baseline case. It can be anticipated that the reason for this behavior is that the thinner the fan case, the less rigid the structure becomes, allowing for greater deformations and thus dissipating a larger amount of energy through this mechanism. This conclusion is supported by subsequent results presented.

As a result, more attention is focused on cases 7, 8, and 9 during the subsequent analysis, as they offer the most promising relative advantages.

4.1.2 Numerical evaluation

The numerical evaluation of the results for the presented cases is carried out in this section. Similar to previous studies, the evolution of energies is analyzed, and the quality of the results provided by

the numerical model is assessed. It is important to note that the numerical model analyzed in the previous chapter, which was deemed satisfactory, may yield different results when varying certain characteristics, such as the fan case thickness.

Fig. 4.2 illustrates the behavioral trends of the different cases through the most relevant global energies in this study. As anticipated, the kinetic energy is lower for the latter cases, with noticeable differences starting from case 7. Consequently, there is an increase in internal energy, which represents the elastic and plastic deformations of the overall system. It can be observed that cases 8 and 9 exhibit the most significant deviations.

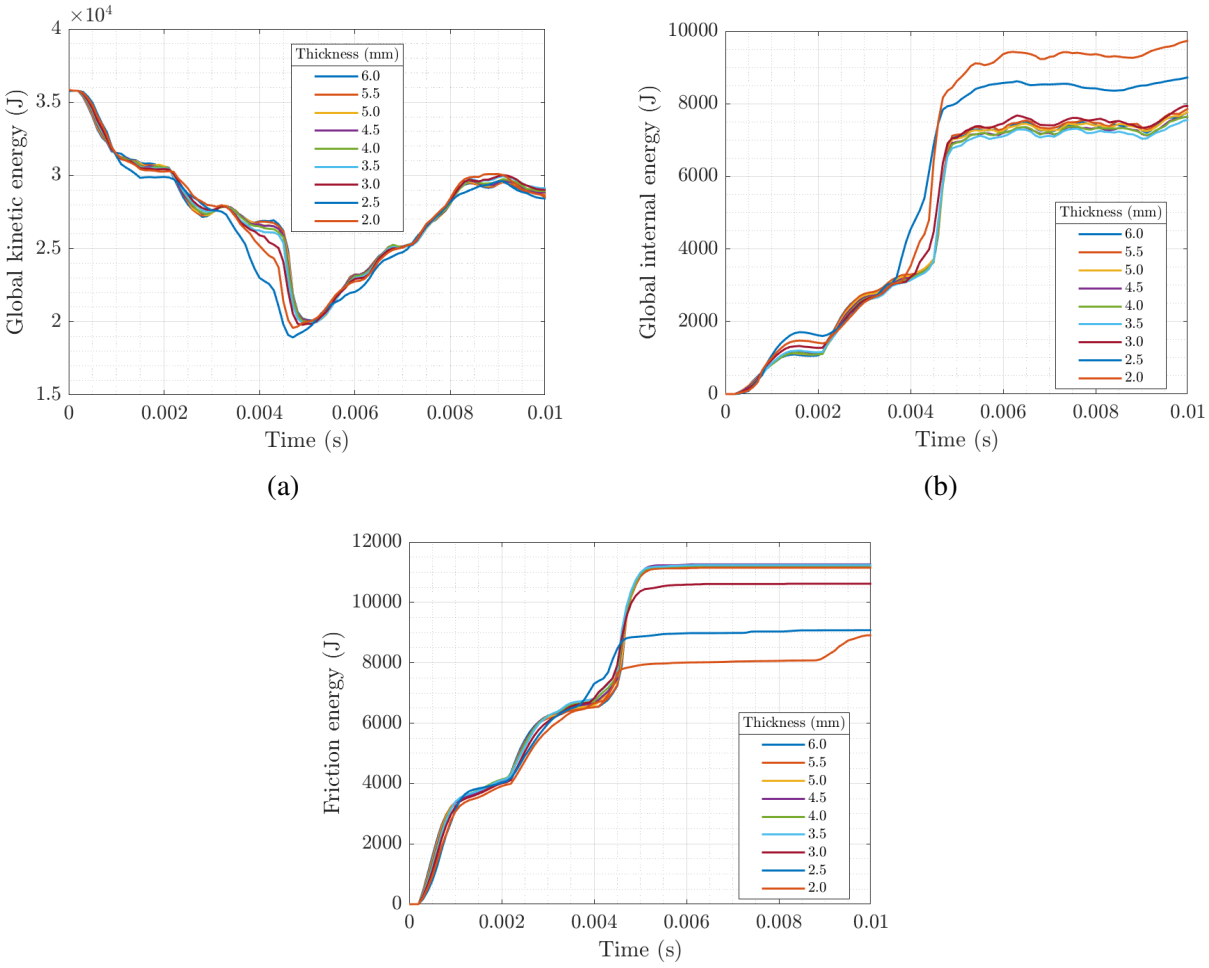

Figure 4.2: Global kinetic (a), internal (b) and friction energies time evolution for the different design cases.

Furthermore, concerning the friction energy evolution, it is apparent that as the fan case becomes thinner, the final accumulated value is lower from case 7 onwards. Additionally, in the final moments of case 9, there is a sudden increase in friction energy. This is due to the trailing

blade tip rubbing against the highly deformed fan case. This confirms the importance of not excessively reducing the thickness to avoid such chain reactions.

Since the most significant deviations occur in the internal energy, a detailed study of the component-level internal energy is also conducted. Fig. 4.3 shows that it is in the case of the fan case where the additional deformations compared to the baseline occur. Certain differences can also be observed in the two blades, but the fan case experiences the most severe deformations.

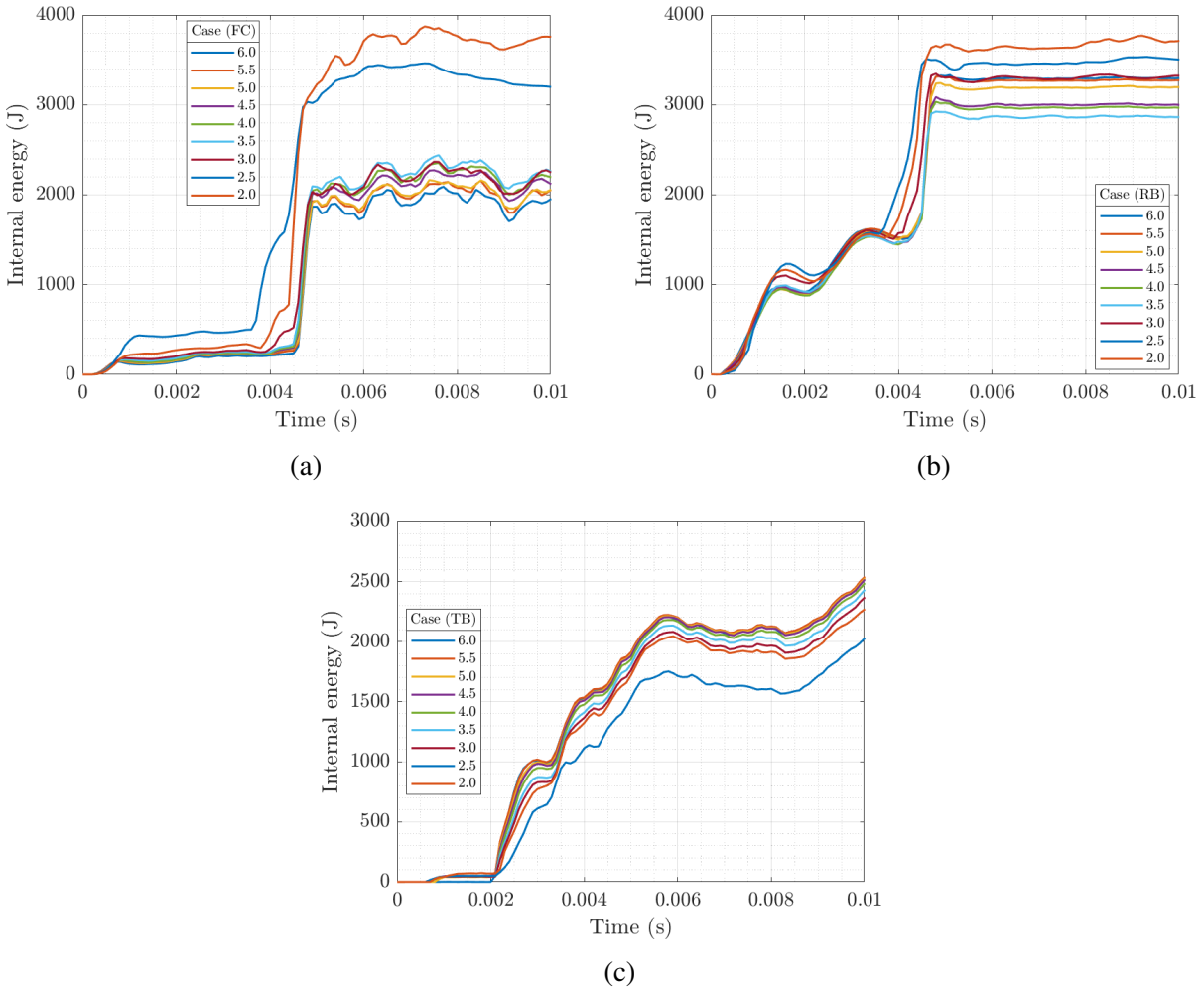

Figure 4.3: Global kinetic (a), internal (b) and friction energies time evolution for the different design cases.

The magnitude of these deformations is illustrated in Fig. 4.4. Case 8 appears to be the least favorable option among the three considered. The fan case undergoes excessively pronounced deformations, indicating a lack of structural integrity. This issue could potentially be addressed by introducing stiffeners. However, it would also result in additional weight, necessitating a careful evaluation of the trade-offs. As for case 9, the sequence of events seems to be slightly more

advantageous for the fan case. However, the rubbing effect at the end needs to be taken into account as an undesirable outcome.

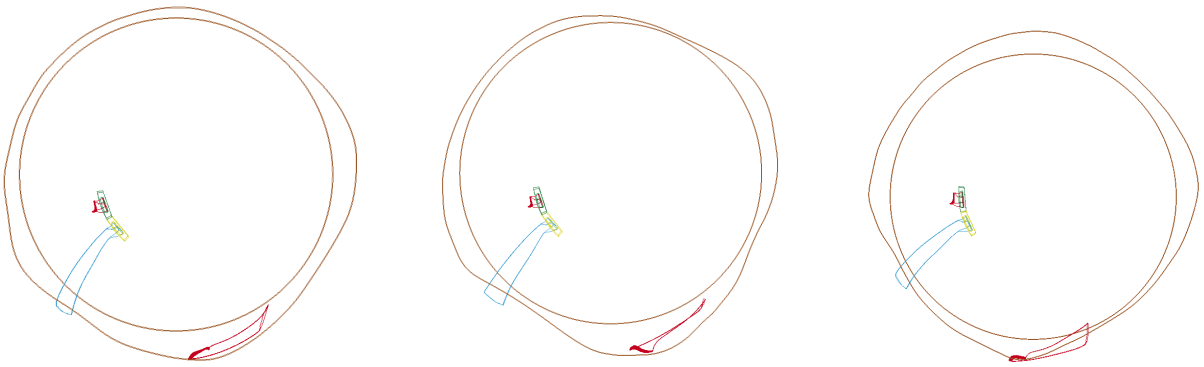

(a) (b) (c)

Figure 4.4: Schematic deformed design models cases 7 (a), 8 (b) and 9 (c) at t=8.7 ms.

In numerical terms, it was expected that varying a parameter that alters the sequence of events and the magnitude of loads would lead to different behavior compared to the baseline case. The model is particularly affected in terms of hourglass energy as the fan case becomes thinner. Once again, this is an expected effect since the deformations incurred are more pronounced and localized. Fig. 4.5 illustrates the evolution of the hourglass ratio for both the overall simulation and specifically for the fan case. In both cases, case 7 appears to reach a limit concerning the acceptable values of this variable, with a global value of 5.48% and 9.46% for the fan case.

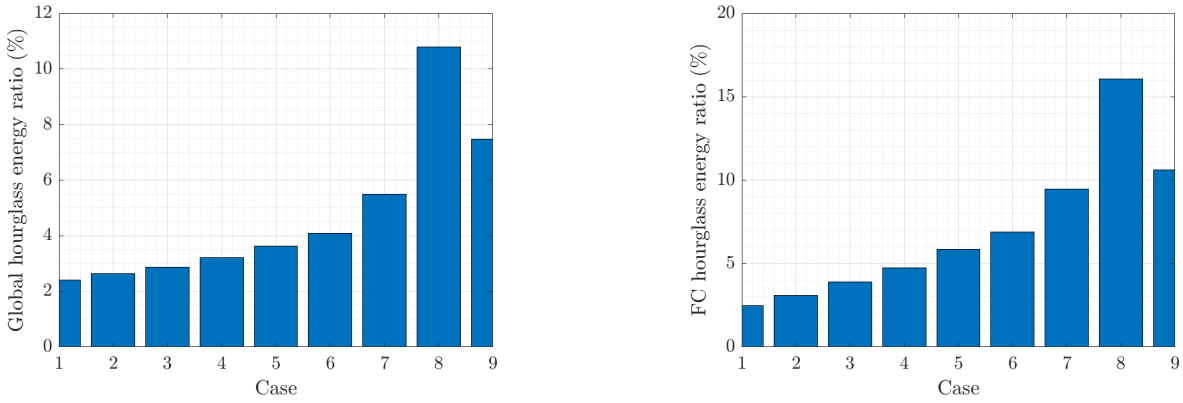

(a) (b)

Figure 4.5: Global (a) and fan case (b) hourglass energy to peak internal energy ratio for the different design cases.

Regarding case 8, once again it is demonstrated that it is not the optimal solution for this numerical study. Globally, the hourglass energy represents slightly over 10% of the peak internal energy, and for the fan case, it accounts for 16%.

It should be noted that for the analysis of lower thicknesses, a reassessment of the baseline numerical model would be necessary. From case 9 onwards, the quality of the results could be compromised with the current numerical parameters employed.

Therefore, based on the results, everything indicates that the optimal design case in this scenario is case 7. This model exhibits the greatest relative advantages compared to the baseline, both in terms of reducing the velocity of the released blade (81.2%) and lightening the fan case (50.13%). Furthermore, it represents a threshold on the thickness range that introduces structural integrity issues after the impact, which, in this case, is from 2.5 mm onwards. Consequently, it can be concluded that the optimal thickness for the fan case lies between **3 mm and 2.5 mm**, excluding the latter.

4.1.3 Conclusions

In conclusion, the study involved varying the thickness of the fan case to evaluate its impact on performance. Nine cases, including a baseline case with 6 mm thickness, were analyzed by decreasing the thickness in increments of 0.5 mm up to 2 mm. The mass of the FC was a crucial factor in the final model selection. The results were evaluated based on the reduction in velocity of the released blade, the containment capability, and the level of deformation.

The temporal evolution of the released blade's velocity indicated that thinner FCs resulted in slightly greater reductions. This was advantageous as it also reduced the FC's mass, with case 7 showing over 50% mass reduction compared to the baseline. Thinner fan cases were less rigid, allowing for greater deformations and dissipation of more energy. Cases 7, 8, and 9 showed promising results due to their relative advantages.

In terms of energy analysis, thinner cases exhibited lower kinetic energy but higher internal energy, especially cases 8 and 9. The friction energy decreased with thinner fan cases, except for an increase due to rubbing in case 9. Deformation analysis revealed that the FC experienced the most severe deformations compared to other components, particularly in case 8. Case 9 showed a more favorable sequence of events, although rubbing needed to be addressed.

The study highlighted the challenge of hourglass energy as the FC became thinner, reaching a limit in case 7. Therefore, the optimal FC thickness range was determined to be between 3 mm and 2.5 mm, excluding the latter. Case 7 was recommended as it achieved the greatest advantages, including a substantial reduction in the released blade's velocity (81.2%) and a significant weight reduction of the FC (50.133%). This study provides a logical and efficient methodology for evaluating fan case designs, but it should be applied cautiously to other models and more advanced analyses.

4.2 Selected Case Study: Analysis of Results

In this section, the obtained results of the chosen case study, Case 7, with a fan case thickness of 3 mm, are presented. Firstly, the energy transfers between the different components involved in the impact are analyzed. Snapshots of the simulation are provided to visually illustrate the sequence of events.

Next, as part of evaluating the design's effectiveness, the containment capacity of the selected fan case is examined. This is done by studying the effective plastic strain in the fan case. Additionally, relevant results from a similar simulation that includes the mentioned failure criterion in Section 3.5 are included for illustrative purposes. The reason for this is that the containment capacity relies on the fan case's resistance to penetration or puncture, and since failure is not considered, the evaluation can only be qualitative based on reasoning.

Lastly, the results related to the transfer of loads to the rest of the engine after the impact are presented. These forces are evaluated through the boundary conditions at the fan case outlet, which simulate the attachment to the rest of the engine. This information can be valuable for the design of subsequent engine stages.

4.2.1 Energy transferring

Understanding the energy transfers during impact interactions is important from the perspective of optimizing the major source of energy dissipation. In this case, the objective is to transfer the kinetic energy of the released blade to other forms of energy, such as internal energy of the fan case or the blade itself, or transform it into frictional energy that would be dissipated as heat in reality. Based on the obtained results, which are generally consistent with FBO events, the conclusion can be drawn that the impact occurs in two phases:

1. **Initial (*lower-energy*) impact**: The tip of the released blade strikes the fan case, after which it is struck by the trailing blade, propelling its root towards the fan case.

2. **Complete (*higher-energy*) impact**: The released blade first impacts its trailing edge root, creating a significant and concentrated contact load against the fan case. Finally, the leading edge also impacts its surface and the edges of the blade become in contact with the fan case.

In general, it is the second impact that causes the most damage to the fan case and therefore represents the event where a larger portion of the released blade's kinetic energy is reduced and transformed into one of the mentioned forms. This trend is clearly observed in the temporal evolution of the released blade's kinetic energy. Fig. 4.6 represents this variable along with the main energy sinks to which it is transferred, i.e. fan case's internal energy, blades' internal energy

and friction energy. The black dashed line corresponds to the baseline case for comparison, while the colored lines represent the chosen case. This allows observing the behavior of these energies with respect to the fan case thickness.

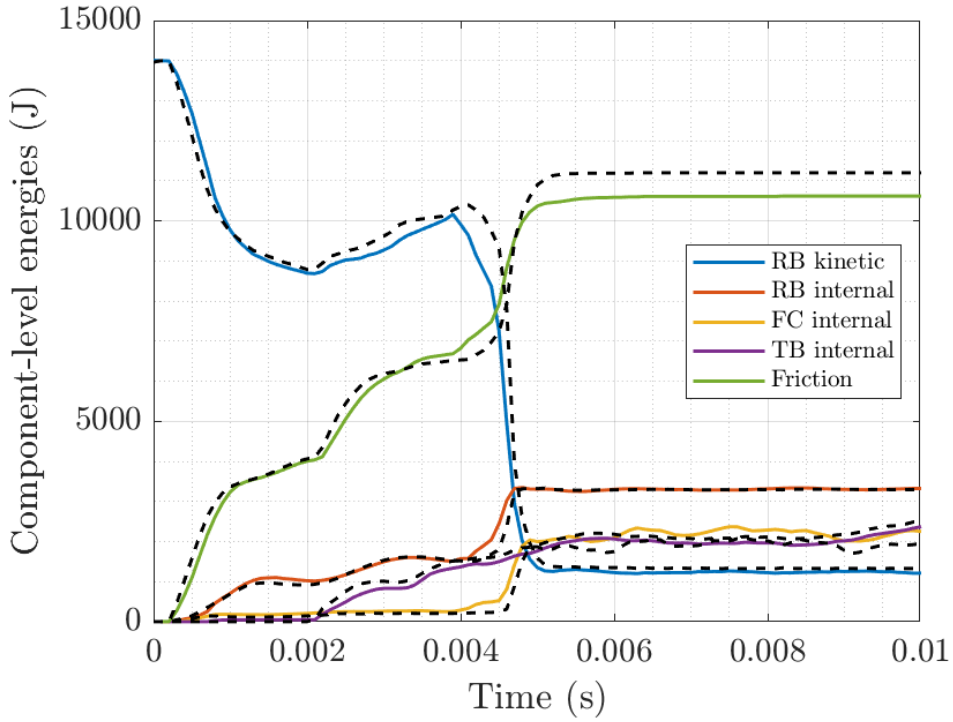

Figure 4.6: Fan case, released blade and trailing blade's internal and kinetic energies and global friction energy time evolution for the 3 mm (colors) and the 6 mm thickness configuration (dashed-black).

Compared to the baseline case, the kinetic energy of the released blade is more reduced to a certain extent, the energy transferred to friction is also decreased, while the internal energy of the released blade is very similar to the initial case. Regarding the internal energy of the fan case, it is slightly higher, as expected, since greater deformation occurs in thinner fan cases. Lastly, it appears that the trailing blade undergoes less deformation for the 6 mm case than for the 3 mm case.

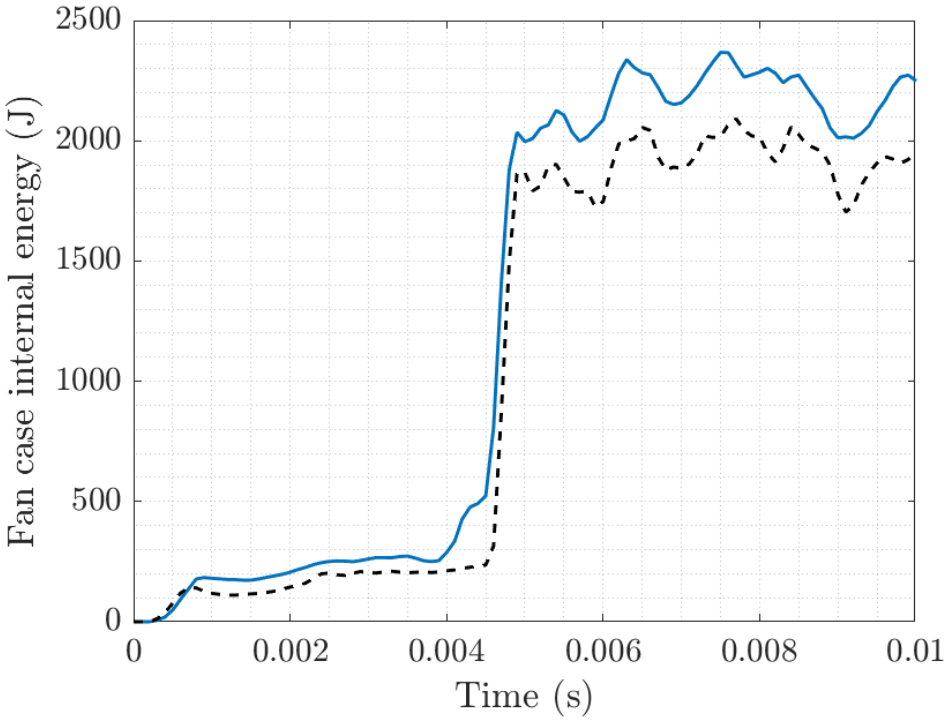

Figure 4.7: Fan case internal energy evolution for the 3 mm (blue) and the 6 mm thickness configuration (dashed-black).

Next, the two phases of the impact are studied in more detail. It can be observed from Fig. 4.6 that the first drop in kinetic energy of the released blade occurs approximately from 0.2 ms (when the blade tip makes contact with the fan case) to 21 ms when the released and trailing blades also come into contact. During this region, there is a decrease of approximately 37% of the initial released blade's kinetic energy. A significant portion of this energy, around 80%, is dissipated through the friction between the fan case and the released blade, which are the only parts in contact. Additionally, around 20% is transformed into internal energy within the released blade due to the deformations it undergoes during this phase. Finally, the fan case experiences slight deformation but does not act as a primary source for reducing the released blade's velocity. This fan case internal energy is around the same magnitude of its kinetic energy, reason for which it has not been introduced in the graph, being even less representative.

It should be noted that these values are estimates based on event observation and plot analysis. The values are not exact since the curves are not monotonically increasing, which means that some estimated reductions in kinetic energy for the released blade may actually correspond to other energy transfers between components, e.g. the fan case's internal and kinetic energy interchange. Nevertheless, the estimated values are useful for a general assessment of the event's performance and provide relevant conclusions.

Regarding the second phase of impact, which occurs between 3.9 ms and 5.2 ms, it represents the largest drop, accounting for approximately 65% of the initial kinetic energy. It is important to note the small increment due to the resultant released blade's acceleration caused by the trailing blade pushing it against the fan case. In this case, the majority of the kinetic energy is also transferred to friction, primarily concentrated in the interactions between the blade and the fan case, although there may be smaller contributions from other contacts.

The next contributing factors are the deformations suffered by the released blade and the fan case until the end of the impact, where they remain at this maximum value. Each contribution represents around 20% of the total drop. Finally, the TB's internal energy has some contribution, especially in the early moments when it is in contact with the released blade, but it remains insufficient to be considered a significant mechanism. Similar reasoning for the FC's kinetic energy.

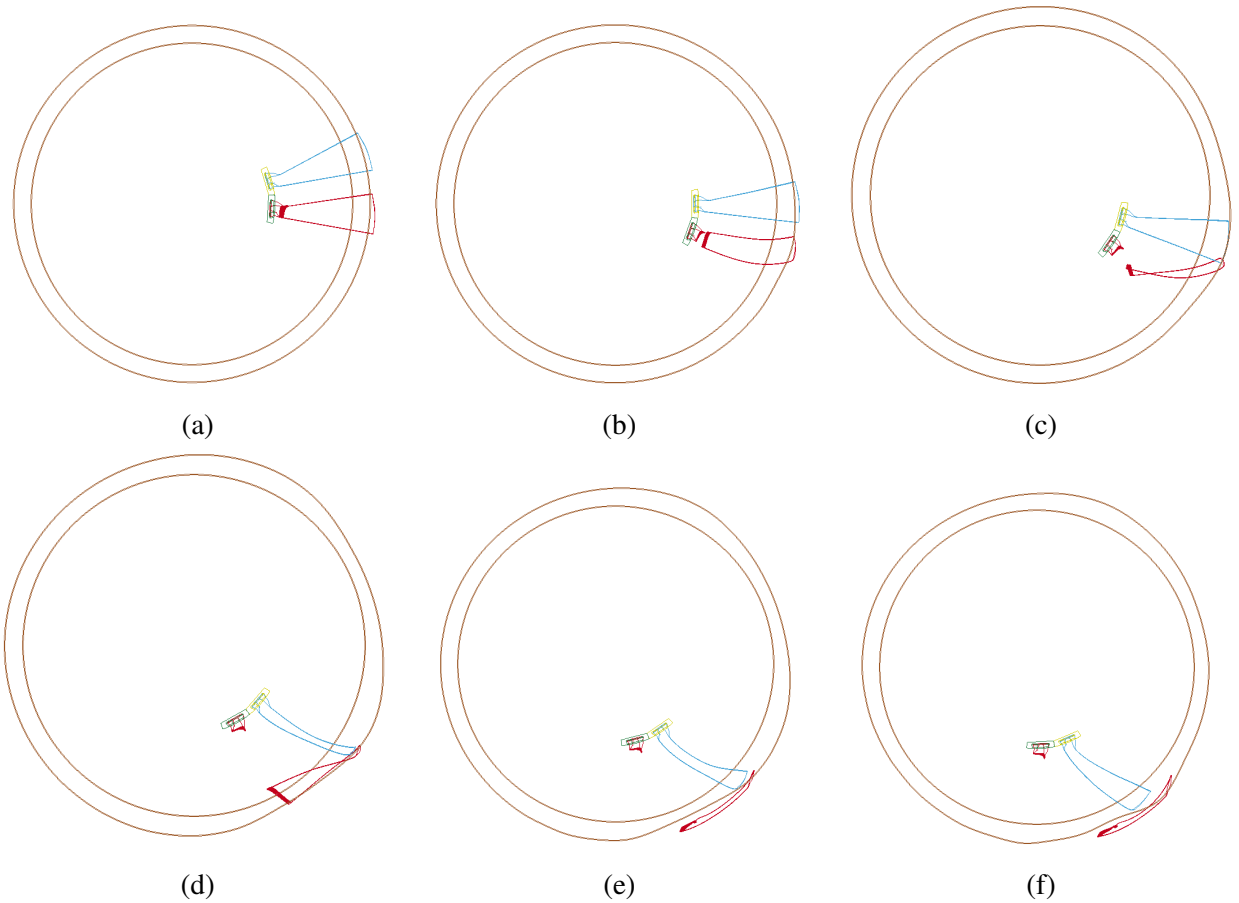

Figure 4.8: Schematic deformed optimal design model during the first impact phase at t=0.2 ms (a), t=1.2 ms (b) and t=2.1 ms (c) and second impact phase at t=3.9 ms (d), t=4.6 ms (e) and t=5.2 ms (f).

Fig. 4.8 presents a series of snapshots depicting the two impact phases for the selected design case. Additionally, Fig. 4.9 includes two additional significant moments: (a) the propulsion of the

RB by the TB towards the fan case, and (b) the RB breaking contact with the FC due to the reversal of its velocity direction towards the motor axis.

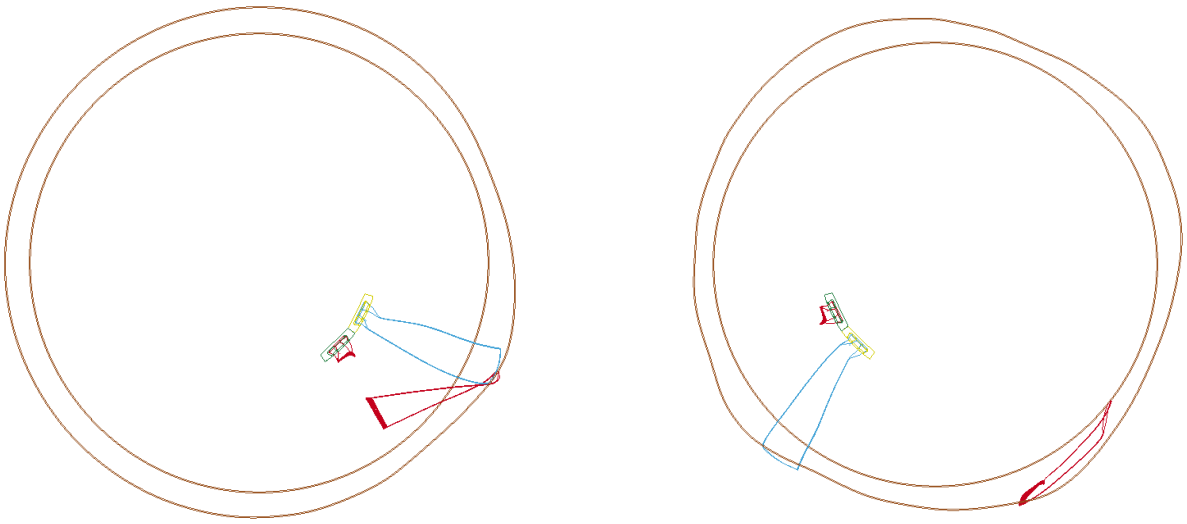

(a) (b)

Figure 4.9: Schematic deformed optimal design model at t=2.8 ms (a) and t=9.4 ms (b).

From these results, it can be concluded that friction is one of the main mechanisms for dissipating the released blade's kinetic energy and, therefore, mitigating the severity of the impact. Despite being reduced with decreasing fan case thickness, as more energy is transferred to other forms (such as internal energy of the fan case), it remains the main mechanism. Therefore, in the present case, it is important to assign high relevance to friction for mitigating the harmful effects of FBO events.

It should be noted that the results obtained, and therefore the main conclusions drawn, may vary if the parameters influencing the friction calculation are changed. An example of this is the friction coefficient for the Coulomb model used. As indicated above, in this case the relevant one provided by the LS-DYNA developers, $\mu_s = \mu_d = 1.05$, has been used. However, according to other sources [25], this parameter may range between 0.3 and 0.6. Thus, it can be intuited that in case of using any value between these indicated, the frictional energy would be lower than the one determined in this case. Therefore, it can be concluded that these results are highly dependent on the parameters introduced and that the conclusions drawn about the role of friction are reduced to the extent of this work and do not necessarily resemble the real case.

The second mechanism of energy transfer appears to be the deformation of the released blade. It is commonly observed that the blade tends to break into three parts upon impact [16], or sharply bends [57], further reducing its kinetic energy. Therefore, this mechanism should be taken into account to prevent the different fragments from causing damage to other components.

Lastly, among the mechanisms worthy of consideration, is the deformation of the fan case. This transfer becomes more significant as the rigidity of the fan case structure decreases, allowing for greater deformations. As the fan case becomes thinner, it behaves more like an agent that "traps" the released blade rather than one that resists and deflects it, approaching the expected behavior for the soft-wall containment architecture.

4.2.2 Containment capability evaluation

The next phase of the study focuses on evaluating the containment capability of the fan case for the released blade during the FBO. In a more advanced numerical analysis, this would be accomplished by studying the structural failure in relevant areas through the observation of erosion of elements. However, since progressive damage and failure is not a feature included in this model, an alternative approach has been employed. This consists of studying the predicted effective plastic strains after impact and estimate if the chosen case possesses this capability or not. The rationale behind this is that the chosen material failure criterion in the model is based on this variable, and therefore it represents the "closeness" to failure. Nevertheless, in order to exemplify some statements of the discussion, results from a variation of the present case that includes the mentioned tensile failure criterion in Section 3.5 are included.

The effective plastic strains after impact are particularly studied in two locations:

- The small impact area of the blade tip against the fan case during the first impact phase.
- The larger zone affected by the second phase of impact.

Both the interior and exterior parts of the fan case are examined to assess whether the impact could cause partial or total blade penetration.

Fig. 4.10 and Fig. 4.11 display the mentioned zones at times at which the maximum values are reached. This allows observing the deformations in the fringe plot at the scale of that instant.

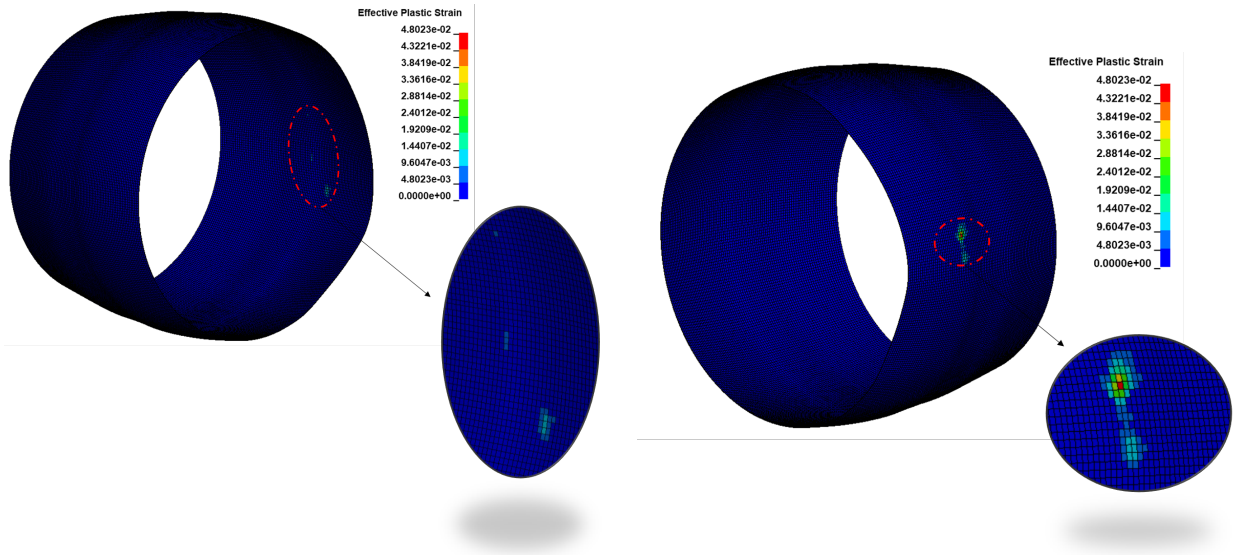

(a) (b)

Figure 4.10: Effective plastic strain fringe plot at t=3 ms of the inner (a) and outer (b) surface of the fan case.

During the first phase of impact, as shown in Fig. 4.10, the strains are relatively low. Given that the effective plastic strain to tensile failure of the Al2024-T3 material composing the FC is 0.12, it can be confirmed that the values are still far from failure. This aligns with the previous assertion regarding the relative severity of the two impact phases, with the first phase causing less damage to the FC.

Another aspect to consider is the stress concentration leading to these strains in such small areas. This can be observed especially on the exterior surface of the fan case, which consistently exhibits higher deformations in all cases.

Regarding the second phase of impact, Fig. 4.11 illustrates the highest plastic strains attained, with a total value of 0.087, still below the tensile failure threshold. From the figure, it can be inferred that the affected area is more extensive, but there are still zones with higher levels of plastic strains. The most heavily loaded point corresponds to the location where the trailing edge root of the RB impacts the FC.

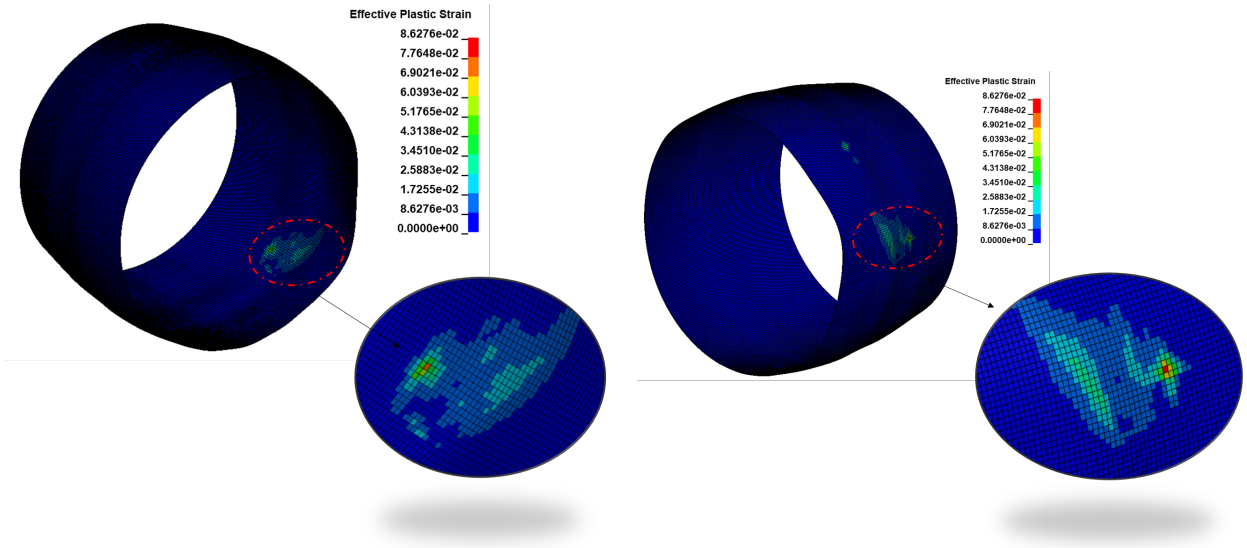

(a) (b)

Figure 4.11: Effective plastic strain fringe plot at t=3 ms of the inner (a) and outer (b) surface of the fan case.

Additionally, despite the significant triaxiality of stresses found throughout the simulation, it can be reasoned that the fracture mechanism suffered by the outer part of the fan case would primarily be under tension. This is due to both the boundary conditions and the mode of application of the main loads (similar to those experienced in a simple bending flexural test). Therefore, it was deemed interesting to include the tension-based failure criterion, albeit without calibration or validation of the model, simply as a comparative representation in case element erosion is allowed after reaching the failure strain.

Fig. 4.12 provides a representation of the plastic strains after the second impact. It can be observed that the affected area is slightly more extensive, with smaller gradients between neighboring elements. Additionally, the maximum values attained are approximately half of those in the model without failure. Hence, it can be deduced that the application of a failure model would result in the prediction of a less severe impact and consequently lower stress and deformation results. This is because, prior to extensive deformation, the element fails and is removed, leading to fewer interactions and lighter components.

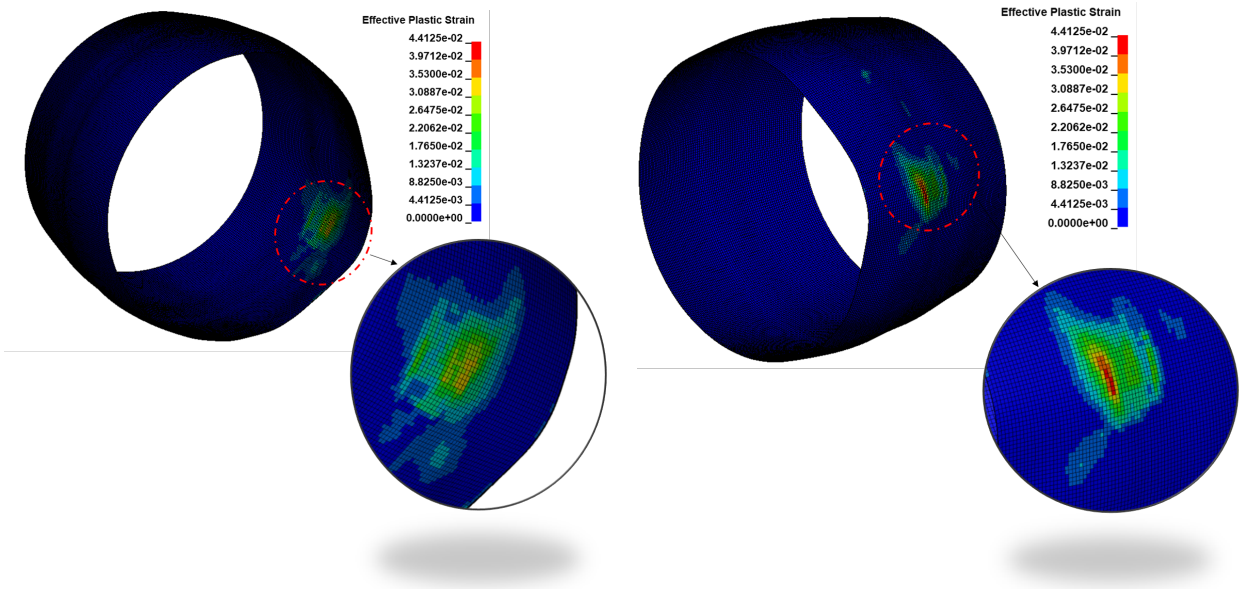

(a) (b)

Figure 4.12: Effective plastic strain fringe plot at t=6 ms of the inner (a) and outer (b) surface of the fan case with failure criterion included.

Despite the evident differences, the sequence of events remains similar to the model considered here, and thus the concentration of plasticity where the root impacts on the FC can also be observed. Lastly, cases 8 and 9 have been evaluated with the addition of the tension-based failure criterion, and even for these cases, the plastic strains do not reach the failure threshold. Although this assessment has no real implications since the model is far from being validated, it is interesting as an object of trend analysis.

Therefore, despite not being able to make absolute statements regarding the containment capability of the FC, the obtained results allow to conclude that this simplified model would be able to effectively contain the blade within the engine. To make a more informed assertion, it would be necessary to calibrate the results with experimental data for the chosen mesh and numerical characteristics.

Consequently, with this analysis, the evaluation of the effectiveness of the model based on the three aforementioned criteria, i.e. velocity reduction, level of deformation, and containment capability, is concluded.

4.2.3 Load derivation assessment

To conclude, the following section presents the results obtained regarding the forces transmitted to the rest of the engine. As observed repeatedly during the analysis, these forces result from the

vibration experienced by the fan case after the impact of the released blade. Additionally, since no dissipative or damping effects have been considered, these forces would persist in this model without reduction in magnitude over time.

The magnitude of these reaction forces is evaluated through the outlet boundary condition of the fan case, applied using the Single Point Constraint method. This condition simulates the attachment of the fan case to the rest of the engine structure, including its connection to the aircraft wing. Consequently, estimating these loads is a crucial aspect of the first phase analysis of the FBO event since they are included in the subsequent implicit analysis to assess the out-of-balance condition for longer times.

To analyze the obtained results, the magnitudes of the resultant force and the axial force (along the z-axis) are presented (Fig. 4.13). The magnitude of the two forces increase over time, with the resultant force oscillating around a mean value of 130.94 kN, while the axial force oscillates around a much lower value of 1.49 kN.

On the one hand, the figure shows that around 4.4 ms, the resultant force experiences a sudden increase in magnitude due to the impacts occurring between the detached blade and the fan case. On the other hand, even with also a notable increase from the impact onwards, the axial force grows more progressively from the beginning of the simulation.

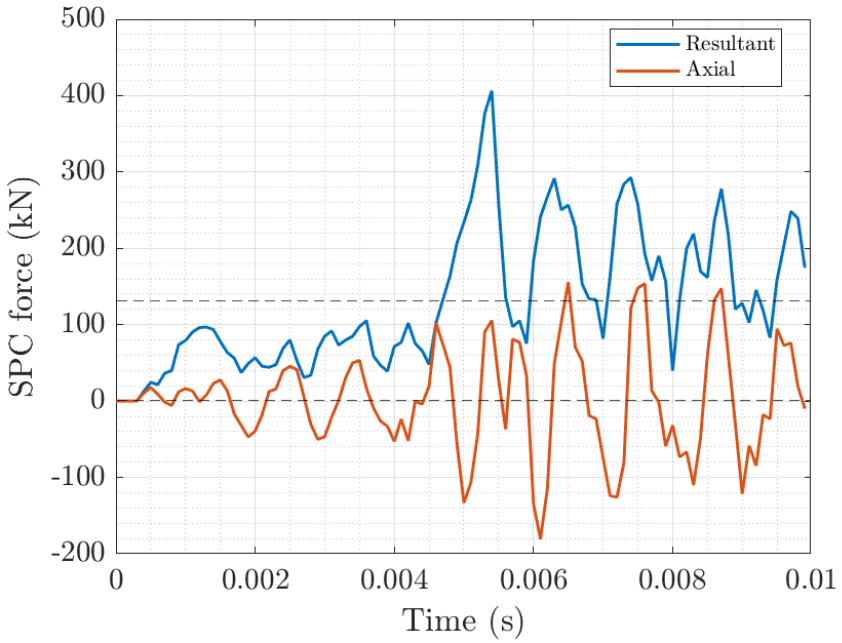

Figure 4.13: Resultant and axial forces time evolution at the outlet boundary.

The maximum value reached in the axial component is 180.94 kN, directed towards the inlet.

As for the maximum oscillatory value of the resultant force, it reaches a magnitude of 405.54 kN and occurs just after the completion of the second phase of the impact.

Regarding the effect of the fan case thickness on these results, the time-evolution of the forces has been analyzed for each considered case. In general, the plots in Fig. 4.14 show that, as the fan case thickness decreases, the resultant force transmitted to the rest of the engine decreases, while the vibration pattern remains fairly the same, with some more notable variations for the thinner fan cases. It can be seen that the most pronounced reductions in the resultant reaction force occur for the chosen fan case thickness, 3 mm, and below, potentially implying structural advantages and overall weight reduction.

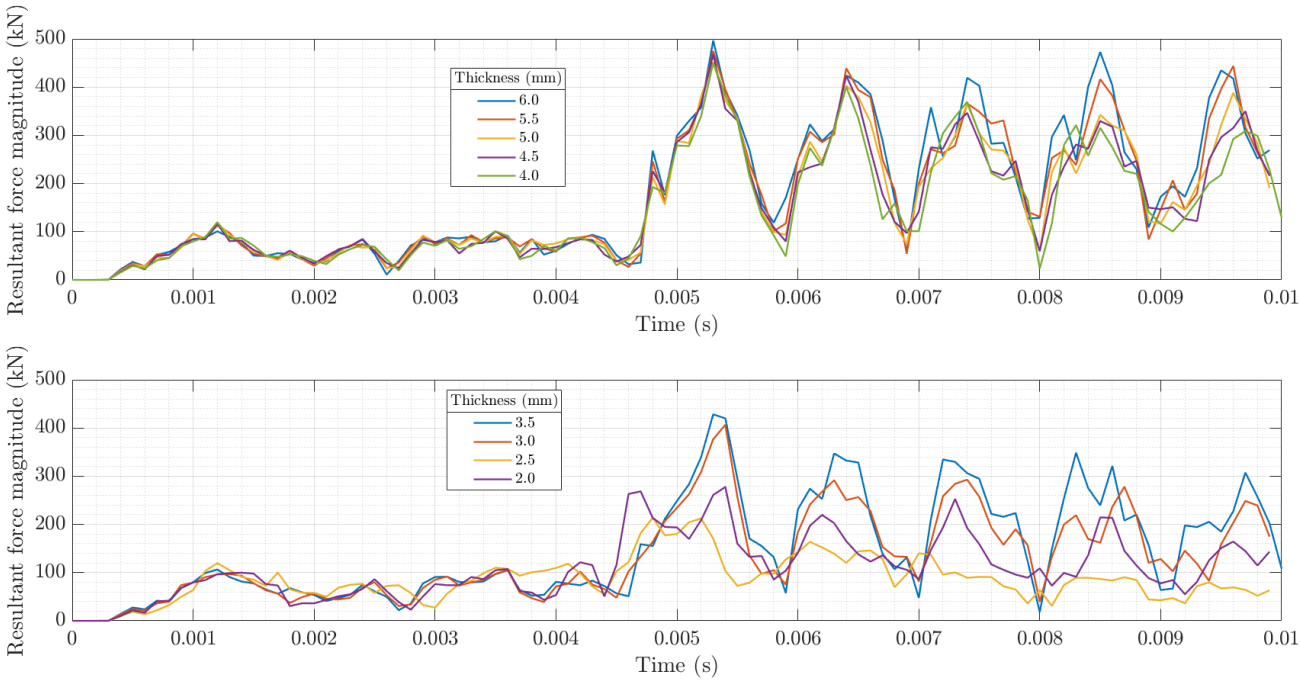

Figure 4.14: Resultant reaction force magnitude at the outlet boundary for the different thickness cases.

Finally, a similar trend is observed for the axial force, Fig. 4.15, with even more significant changes in this case, especially in the function shape for the thinner cases. One possible reason for this is that a more flexible system allows greater deformation in the middle part of the fan case. Therefore, the displacements of the fan case at areas other than the impact are lower, reducing the severity of the response forces at the attachment point. This results in a positive effect for the followed objective of minimizing mass through thickness reduction.

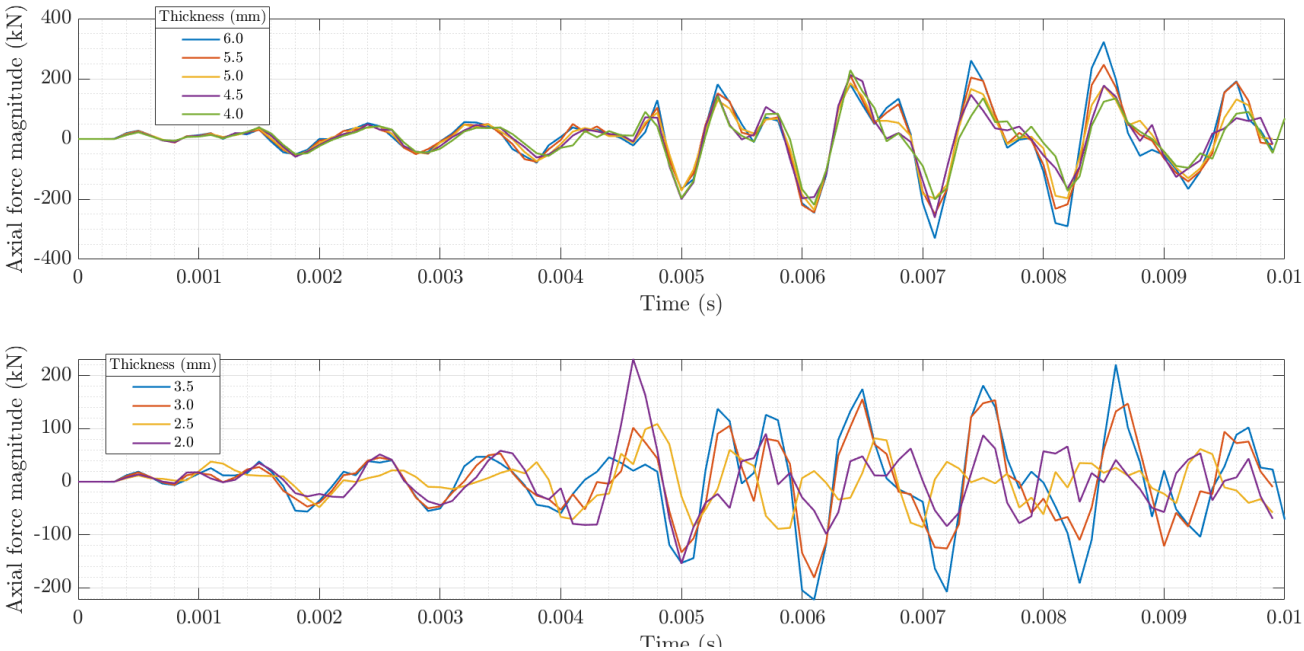

Figure 4.15: Axial reaction force magnitude at the outlet boundary for the different thickness cases.

4.2.4 Conclusions

In conclusion, the analysis of energy transfers in the context of FBO events highlights the importance of understanding and optimizing the major source of energy dissipation. The objective is to transfer the kinetic energy of the released blade to other forms of energy, such as internal energy or frictional energy, in order to mitigate the severity of the impact. The impact occurs in two phases: the initial impact and the complete impact.

The results indicate that the second phase of impact causes the most damage to the fan case, leading to a larger reduction in the released blade's kinetic energy and its transformation into other forms. Friction between the fan case and the released blade plays a crucial role in dissipating energy, even though it decreases with decreasing fan case thickness. The deformation of the released blade also contributes to reducing its kinetic energy. It is important to note that these conclusions are drawn from the simplified model under study. In the real case, where all the blades are included, the interaction of the released blade with them can greatly change the observed results and, therefore, its derived conclusions.

The study of effective plastic strains in the fan case provides insights into its containment capability. The plastic strains observed during the impacts are below the failure threshold of the material, indicating that the simplified model would be able to effectively contain the blade within the engine. However, further calibration and validation of the model with experimental data are necessary to make more accurate assessments.

The forces transmitted to the rest of the engine after the impact are evaluated through the analysis of the time evolution of the magnitude of the reactions at the SPC applied on the engine aft. The resultant force and axial force show increasing magnitudes over time. The resultant force experiences a sudden increase after the completion of the second phase of impact, while the axial force grows more progressively. The fan case thickness affects these forces, with thinner cases transmitting lower forces to the rest of the engine.

In conclusion, understanding the energy transfers, assessing the containment capability, and evaluating the forces transmitted to the rest of the engine are crucial aspects in mitigating the effects of FBO events and ensuring the safe operation of aircraft engines.

Chapter 5

Conclusions and future work

This chapter encapsulates a general exposition of the numerical model for the Hard-wall Containment design, along with the various analysis processes undertaken to ensure its robust functionality. By assimilating the insights garnered from the preceding sections, this chapter offers a comprehensive overview of the essential findings and the principal contributions that have collectively fortified the construction of the fan blade-off model.

5.1 Summary and Main Contributions

For clarity, this section has been divided into the two main phases that has composed this work. On the one hand, familiarization with the field of study and the environment and tools used for the construction of the blade-off model, i.e., training and pre-processing. This phase is collected under the name "Numerical model" in Section 5.1.1.

On the other hand, in Section 5.1.2, and under the name "Analysis procedures", everything related to the post-processing, study of the results obtained and extraction of the main conclusions drawn throughout this report is included.

5.1.1 Numerical Model

The crux of this section resides in the delineation of the numerical model underpinning the Hard-wall Containment design. The subsequent explanation of the various analysis processes serves to corroborate the model's integrity and effectiveness. The following sections summarize the pivotal stages:

- *General Simulation Conditions* (Section 3.1): The foundational simulation conditions are presented in this section and derived sub-sections, providing a fundamental reference point

for all subsequent variations. This elucidation facilitates a coherent comprehension of the foundational framework upon which subsequent analyses are built.

- *Mesh Sensitivity Analysis of Blade Elastic Region* (Section 3.2): Section 3.2 consists of the exploration of the model's sensitivity to mesh variations in the blade elastic region during the application of the pre-stresses. Through distinct sub-sections, the obtained results emerge as a testament to the deliberative process that culminates in the identification of the optimal mesh configuration. These findings serve to substantiate the rationale behind the ultimate mesh selection in this specific context.

- *Mesh Sensitivity Analysis of Hard-wall Containment Model* (Section 3.3): Akin to the previous analysis, Section 3.3 extends the scrutiny to encompass the Hard-wall Containment Model in its entirety. The meticulous examination of numerical results against varying mesh configurations culminates in a judicious selection while acknowledging the model's limitations.

Main Contributions to Fan Blade-Off Model Construction

This study's foremost contributions to the advancement of the simplified fan blade-off model's construction are based especially on decision criteria and technical evaluation through the theoretical concepts acquired during the master's degree. They emerge as key insights extracted from the progressive learning journey through the intricacies of numerical modeling and analysis:

1. *Robust Simulation Foundation*: The establishment of comprehensive simulation conditions in Section 3.1 serves as a bedrock for subsequent analyses. This foundational framework offers potential researchers and practitioners a unified starting point for evaluating variations and optimizing model parameters in future developments.

2. *Refinement of Mesh Configuration*: The exploration of mesh sensitivity in both the blade elastic region and the simplified Hard-wall Containment model accentuates the pivotal role of mesh configuration in attaining accurate and stable results. This examination serves as a guidepost for selecting mesh configurations that yield consistent outcomes while mitigating computational overhead.

3. *Informed Decision-Making Process*: The analytical journey outlined in Chapters 2 and 3 reflects an informed decision-making process, wherein the nuances of mesh selection, contact numerical parameters, material models, amongst others, are elucidated and justified systematically. This transparency empowers future researchers to navigate the complexities of building a similar and more advanced model with precision.

4. *Identification of Model Limitations*: The acknowledgment of model limitations is an indis-

pensable outcome of this study. By recognizing the constraints and approximations inherent in the Hard-wall Containment model, those that are potentially interested are encouraged to refine and expand the model's capabilities in future stages of the design process.

In summation, this chapter synthesizes a comprehensive narrative of the rigorous analyses and empirical investigations conducted to shape the Hard-wall Containment design model. The culmination of these efforts has yielded an extensive understanding of mesh sensitivity, a robust simulation foundation, and a meticulous decision-making process. The insights gleaned herein can serve as a cornerstone, a first step in the process, for future research efforts.

5.1.2 Analysis procedures

The comprehensive analysis conducted in this study provides valuable insights into the behavior of the fan blade-off (FBO) event for the built model and its implications for engine performance and safety. By delving into the complex dynamics of energy transfers, transmitted forces, and structural responses, this section presents a summary of the key findings and main contributions derived from the analysis of results of the constructed FBO model.

Energy Transfers and Impact Dynamics

Understanding the transfer of energies during the FBO event is critical for optimizing energy dissipation mechanisms. The objective of transferring kinetic energy from the detached blade to other forms of energy, such as internal energy of the fan case or frictional energy, has been demonstrated through the performed simulations. The impact event was analyzed in two distinct phases: initial impact and complete impact.

- Initial Impact: The tip of the detached blade contacts the fan case, subsequently experiencing a secondary impact from the trailing blade, resulting in a root-propelled motion.
- Complete Impact: The detached blade's leading edge impacts the fan case, causing a significant contact load against the fan case's surface. Notably, the second phase inflicts the most substantial damage, transforming a considerable portion of the detached blade's kinetic energy into other energy forms, particularly through friction and deformation of the released blade itself.

The reduction of kinetic energy through friction highlights its importance as a primary mechanism for mitigating the severity of the impact event under the undertaken assumptions. This insight underscores the need to prioritize frictional energy dissipation in FBO event considerations in this particular model, offering an avenue for effective energy management.

Effective Plastic Strain Analysis for Containment Capability Assessment

The study also contributes to evaluating the containment capability of the fan case through an examination of effective plastic strains. While the model provides an indicative assessment, further calibration and validation are essential to accurately determine the fan case's capacity to contain the detached blade. The analysis suggests that the simplified model shows potential for effective containment, but refinement and validation are necessary to establish its credibility.

Forces Transmitted and Structural Response

The investigation extends to the analysis of forces transmitted to the rest of the engine, a critical aspect of FBO events. The magnitude of these forces is influenced by the fan case's thickness and its attachment to the engine structure. The examination of the reaction force magnitude oscillations revealed that the resultant force experiences abrupt magnification due to impacts between the detached blade and the fan case. Conversely, the axial force shows gradual growth over time.

Through this analysis, the model's results demonstrate the need to consider transmitted forces for the effective design and implementation of damping or isolation systems. These measures are vital to mitigate the potential adverse effects of FBO events, in alignment with regulatory requirements. However, it should be noted that since the model does not represent the complete engine, this recommendation for stress mitigation is limited to the simplified model studied here.

Main Contributions to the Analysis of the FBO event

The main contributions of this work to the study of the FBO event and post-processing of results are summarized as follows:

1. *Energy Dissipation Mechanisms*: The study highlights the significance of friction and deformation in dissipating the detached blade's kinetic energy. This knowledge enriches the understanding of energy transfers during FBO events and underscores the role of friction in managing impacts.

2. *Containment Capability Assessment*: The effective plastic strain analysis provides insight into the fan case's potential to contain the detached blade. While requiring further validation, this approach offers a preliminary assessment of containment effectiveness.

3. *Force Transmissions and Impact Severity*: By analyzing forces transmitted to the engine, the study contributes to the evaluation of FBO event consequences and the necessity of implementing mitigation measures. This understanding aids in enhancing safety protocols and design considerations, since the value of these loads must be derived to subsequent analyses such as the implicit-solver simulation of the post-containment conditions.

In conclusion, this section summarizes the findings and contributions derived from the study's comprehensive analysis of the FBO event. The insights gained provide a preliminary but robust foundation for further research and the development of strategies to enhance safety in the face of potential FBO events.

5.2 Future Research Perspectives

As the present study draws to a conclusion, it becomes evident that the complexities inherent in the construction and analysis of the Hard-wall Containment design model leave room for substantial improvement and refinement. This section deepens into the myriad avenues that remain uncharted due to the temporal constraints imposed on this MSc thesis. Furthermore, it highlights the characteristics of the model that beckon for enhancement and represent potential domains of future research.

Unexplored Modeling Features

Undoubtedly, the pursuit of scientific inquiry is constrained by the practical limitations of time and resources. This study, while comprehensive within its scope, necessarily omits certain facets of investigation that require dedicated exploration. Given the intricate nature of the Hard-wall Containment design model and the multifaceted dimensions of fan blade-off events, with no deliberate order, several promising avenues warranting deeper analysis are proposed:

- *Dynamic Interaction Effects*: While this study encompasses fundamental analysis of impact phases and energy transfers, the dynamics of interacting components during a fan blade-off event need for extensive investigation. Unraveling the intricate interplay between blade fragments, fan case, and structural attachments could unveil previously unforeseen phenomena.

- *Material Characterization, Failure, and Damage Models*: An in-depth exploration of material behavior and failure and progressive models could augment the precision and realism of the model. Investigation and data disposition of the behavior of materials under extreme conditions (high strain rates and damage/fracture) could provide a more accurate representation of structural response during blade detachment and subsequent impact.

- *Advanced Meshing Techniques*: The current mesh sensitivity analyses provide valuable insights into mesh configuration's impact on results. However, the potential for employing advanced meshing techniques, such as adaptive mesh refinement or hybrid meshing, combining regular and irregular meshes, remains untapped. In addition, the construction of a mesh that allows the complex geometry of the leading and trailing edges of the blade to

be more faithfully represented without encountering elements that excessively jeopardize CPU times could be another notable approach. Exploring these techniques could optimize computational efficiency and result accuracy.

– *Multi-Physics Coupling*: Incorporating multi-physics coupling, encompassing fluid-structure interaction and thermal effects, would confer greater fidelity to the model. The consideration of heat dissipation and fluid flow could yield a comprehensive understanding of the broader impact of blade-off events on engine components.

Enhancements and Future Directions

As this study has paved the way for the construction of the Hard-wall Containment Design model, it is imperative to recognize directions for improvement that could significantly enrich future advancements of the electric fan model:

– *Experimental Validation*: A natural progression entails experimental validation of the model's predictions. The fusion of empirical data with numerical simulations would bolster the model's reliability and validate its accuracy.

– *Advanced Constitutive Models*: Incorporating advanced constitutive models for material behavior, such as strain-rate effects or damage mechanics, could provide a more nuanced understanding of structural response under such dynamic loading conditions.

– *Complex Loading Conditions*: The exploration of diverse loading scenarios, such as varying blade impact angles and speeds, could unearth the model's response to a broader spectrum of fan blade-off events.

– *Multi-Component Analysis*: Extending the model to encompass other engine components' interactions and responses could yield a broader view of fan blade-off events and their repercussions on overall engine performance.

In summation, while this study's contributions to fan blade-off modeling are notable for the granted extension, it is important to acknowledge that the journey has merely scratched the surface of an intricate landscape. The model's dynamic potential and its capacity to simulate the complexities of aviation safety warrant a sustained commitment to further research. The unexplored domains and potential enhancements identified here serve as a rallying call for future developers to go deeper into the field of fan blade-off events, contributing to the ongoing evolution of aviation safety and propulsion engineering.

Bibliography

[1] ANSYS - Engineering Simulation Software. https://www.ansys.com/, .

[2] Ansys Granta - Materials Information Management. https://www.ansys.com/products/materials, .

[3] ASME - The American Society of Mechanical Engineers. https://www.asme.org/.

[4] European Union Aviation Safety Agency. https://www.easa.europa.eu/en.

[5] Federal Aviation Administration. https://www.faa.gov/.

[6] General Electric GE90. https://www.wikiwand.com/en/General_Electric_GE90.

[7] JAHM Software. https://www.jahm.com/.

[8] Air Accidents Investigation Branch reports. https://www.gov.uk/aaib-reports.

[9] Hourglass (HG) Modes - LSTC LS-DYNA Introduction Class. https://ftp.lstc.com/anonymous/outgoing/support/FAQ_docs/hourglass.pdf.

[10] Ansys LS-DYNA. https://www.ansys.com/products/structures/ansys-ls-dyna.

[11] Press releases - GKN Aerospace To Lead Development Of Electric Fan Thruster For Electric Aircraft. https://www.gknaerospace.com/en/newsroom/news-releases/2021/gkn-aerospace-to-lead-development-of-electric-fan-thruster-for-electric-aircraft/.

[12] AWG ERIF Test Case Suite Overview. https://awg.ansys.com/Test+Case+Suite.

[13] 'Uncontained' CFM56-7 FBO Failures: Southwest B737-700s 27 Aug 2016 & 17 Apr 2018. https://aerossurance.com/safety-management/uncontained-cfm56-failure-b737/.

[14] S. Abotula and V. Chalivendra. An experimental and numerical investigation of the static and dynamic constitutive behaviour of aluminium alloys. *Journal of Strain Analysis for Engineering Design*, 1:1–11, November 2010. doi: 10.1243/03093247JSA655.

[15] FAA Advisory Circular. Design considerations for minimizing hazards caused by uncontained turbine engine and auxiliary power unit rotor failure, March 1997. Report No.: 20-128 A.

[16] LS-DYNA Aerospace Working Group. *Modeling Guidelines Document*, 2022.

[17] P. Baranowski, J. Malachowski, P. Płatek, and S. Aleksandra. LENS Ti-6Al-4V alloy material properties determination for LS-Dyna package. page 020058, March 2019. doi: 10.1063/1.5092061.

[18] J. Bonet. *Nonlinear continuum mechanics for finite element analysis*. Cambridge University Press, Cambridge, 2nd edition. edition, 2008. ISBN 9780511755446.

[19] K.S. Carney, J.M. Pereira, D.M. Revilock, and P. Matheny. Jet engine fan blade containment using an alternate geometry. *International Journal of Impact Engineering*, 36(5):720–728, 2009. ISSN 0734-743X. doi: https://doi.org/10.1016/j.ijimpeng.2008.10.002. URL https://www.sciencedirect.com/science/article/pii/S0734743X08002388.

[20] H. Challons and A. Sufiis. Foreign Object Damage and Fan Blade Out. *OTAN*, 2012.

[21] G. Chen. Aviation Engine Structure Design Analysis. 2006.

[22] I. Eryilmaz, B. Guenchi, and V. Pachidis. Multi-blade shedding in turbines with different casing and blade tip architectures. *Aerospace Science and Technology*, 87:300–310, 2019. ISSN 1270-9638. doi: https://doi.org/10.1016/j.ast.2019.02.025. URL https://www.sciencedirect.com/science/article/pii/S1270963818309064.

[23] S. Fabry and M. Češkovič. Aircraft gas turbine engine vibration diagnostics. *MAD - Magazine of Aviation Development*, 5:24, November 2017. doi: 10.14311/MAD.2017.04.04.

[24] Department Of Transportation Federal Aviation Administration. Airworthiness standards: Aircraft engines, January 2002. FAA-FAR-33.94.

[25] H. Geijselaers, A. van der Stelt, and T. Bor. Dry friction during sliding of AA1050 on AA2024 at elevated temperature. *Procedia Engineering*, 207:1671–1676, 2017. ISSN 1877-7058. doi: https://doi.org/10.1016/j.proeng.2017.10.920. URL https://www.sciencedirect.com/science/article/pii/S1877705817357065. International Conference on the Technology of Plasticity, ICTP 2017, 17-22 September 2017, Cambridge, United Kingdom.

[26] J.O. Hallquist. *LS-Dyna Theory manual*. California Livermore Software Technology Corporation, 2006.

[27] M. Heidari, D. Carlson, S. Sinha, R. Sadeghi, C. Heydari, H. Bayoumi, and J. Son. *An Efficient Multi-Disciplinary Simulation of Engine Fan-Blade Out Event Using MD Nastran*. 2012. doi: 10.2514/6.2008-2333. URL https://arc.aiaa.org/doi/abs/10.2514/6.2008-2333.

[28] Systems Honeywell Engines and Services. Explicit Finite Element Modeling of Multilayer Composite Fabric for Gas Turbine Engine Containment Systems, Phase II. Part 4: Model Simulation for Ballistic Tests, Engine Fan Blade-Out, and Generic Engine. Technical report, Department of Transportation Federal Aviation Administration, 2009.

[29] J. B. Husband. *Developing an Efficient FEM Structural Simulation of a Fan Blade Off test in a Turbofan jet engine*. PhD thesis, University of Saskatchewan, 2007.

[30] IATA. Industry net zero resolution. *77th IATA AGM*, 2021.

[31] M. Jamal-Omidi and M. R. Mohammadi Suki. A Numerical Study on Aluminum Plate Response under Low Velocity Impact. *International Journal of Engineering*, March 2017.

[32] Z. Jeffrey. Archive photos: 1989 Flight 232 crash in Sioux City. URL https://eu.desmoinesregister.com/picture-gallery/news/2014/07/11/archive-photos-1989-flight-232-crash-in-sioux-city/12554379/.

[33] S. Krishnam and G. Srinivas. Recent Developments of Materials used in Air breathing and Advanced Air breathing Engines. *IOP Conference Series: Materials Science and Engineering*, 872:012082, June 2020. doi: 10.1088/1757-899X/872/1/012082.

[34] D. Leseur. Experimental investigations of material models for Ti-6A1-4V and 2024-T3. May 1999. doi: 10.2172/11977. URL https://www.osti.gov/biblio/11977.

[35] *LS-Dyna Keyword User's Manual*. Livermore Software Technology, 2021.

[36] G. Marsh. Aero engines lose weight thanks to composites. *Reinforced Plastics*, 56(6): 32–35, 2012. ISSN 0034-3617. doi: https://doi.org/10.1016/S0034-3617(12)70146-7. URL https://www.sciencedirect.com/science/article/pii/S0034361712701467.

[37] J.A. Frutos Martínez, R.R. Ambriz, M. Naït-Abdelaziz, and D. Jaramillo. Impact test behavior of aluminum alloys welded joints: Experimental and numerical analysis. *Fatigue and Fracture of Engineering Materials and Structures*, 44(8):2119–2134, 2021. doi: https://doi.org/10.1111/ffe.13482. URL https://onlinelibrary.wiley.com/doi/abs/10.1111/ffe.13482.

[38] A. Mcmillan. Material development for fan blade containment casing. *Journal of Physics: Conference Series*, 105, March 2008. doi: 10.1088/1742-6596/105/1/012011.

[39] NASA. https://www.nasa.gov/centers/glenn/news/AF/2007/Jan07_printall.html.

[40] NASA Glenn Research Center. Aircraft engines blade out dynamics, 7th International LS-DYNA Users Conference.

[41] M. Nasr and T. Moffat. A design methodology for fan blade-off based on structural failure. November 2009.

[42] J. Ngoret and V.P. Kommula. Monitoring material degradation in aircraft turbine blades: A comprehensive survey on current techniques. May 2016.

[43] T. Nicholas. Dynamic Tensile Testing of Structural Materials Using a Split Hopkinson Bar Apparatus. *Air Force Wright Aeronautical Labs Wright-Patterson AFB OH*, 1980. URL https://apps.dtic.mil/sti/pdfs/ADA092832.pdf.

[44] G. Norris. In Pictures: Rolls-Royce UltraFan Building Blocks. URL https://aviationweek.com/air-transport/aircraft-propulsion/pictures-rolls-royce-ultrafan-building-blocks.

[45] E. Owen. Webinar: LS-DYNA Introduction to contacts. *Oasys*, January 2020.

[46] J. Pereira and D. Revilock. Ballistic Impact Response of Kevlar 49 and Zylon under Conditions Representing Jet Engine Fan Containment. *Journal of Aerospace Engineering - J AEROSP ENG*, 22, July 2009. doi: 10.1061/(ASCE)0893-1321(2009)22:3(240).

[47] J-P. Ponthot. Lecture notes in Large Deformation of Solids, February 2022.

[48] D. M. Revilock and J. M. Pereira. Explicit Finite Element Modeling of Multilayer Composite Fabric for Gas Turbine Engine Containment Systems, Phase II. Part 1; Fabric Material Tests and Modeling. 2009.

[49] D. M. Revilock and J. M. Pereira. Explicit Finite Element Modeling of Multilayer Composite Fabric for Gas Turbine Engine Containment Systems, Phase II. Part 2; Ballistic Impact Testing. 2009.

[50] K. Sengoz, S. Kan, and A. Eskandarian. Development of a Generic Gas Turbine Engine Fan Blade-out Full-Fan Rig Model. 2015.

[51] J. Sharda, C. Deenadayalu, B. Mobasher, and S. D. Rajan. Modeling of multilayer composite fabrics for gas turbine engine containment systems. *Journal of Aerospace Engineering*, 19(1): 38–45, 2006. doi: 10.1061/(ASCE)0893-1321(2006)19:1(38).

[52] Y. Shmotin, D. Gabov, A. Ryabov, S. Kukanov, and V. Rechkin. *Numerical Analysis of Aircraft Engine Fan Blade-Out*. 2012. doi: 10.2514/6.2006-4620. URL https://arc.aiaa.org/doi/abs/10.2514/6.2006-4620.

[53] J. Simmons, D. C. Erlich, and D. A. Shockey. Explicit Finite Element Modeling of Multilayer Composite Fabric for Gas Turbine Engine Containment Systems, Phase II. Part 3; Material Model Development and Simulation of Experiments. 2009.

[54] S. Sinha and S. Dorbala. Dynamic loads in the fan containment structure of a turbofan engine. March 2008.

[55] NASA Safety Center System Failure Case Studies. No left turns. 2008. URL https://en.wikipedia.org/wiki/Turbine_engine_failure#Contained_and_uncontained_failures.

[56] Wikipedia. Uncontained engine failure accidents. URL https://en.wikipedia.org/wiki/Turbine_engine_failure#Contained_and_uncontained_failures. [Online; accessed 17-March-2023].

[57] H. Xuan and R. Wu. Aeroengine Turbine Blade Containment Tests using High-speed Rotor Spin Testing Facility. *Aerospace Science and Technology*, 10(6):501–508, 2006. ISSN 1270-9638. doi: https://doi.org/10.1016/j.ast.2006.04.006. URL https://www.sciencedirect.com/science/article/pii/S1270963806000526.

[58] B. Yang. Blade Containment Evaluation of Civil Aircraft Engines. *Chinese Journal of Aeronautics*, 26(1):9–16, 2013. ISSN 1000-9361. doi: https://doi.org/10.1016/j.cja.2012.12.001. URL https://www.sciencedirect.com/science/article/pii/S100093611200009X.

[59] Z. Zhenhua, L. Lulu, C. Wei, and L. Gang. Numerical simulation methodology of multi-layer Kevlar 49 woven fabrics in aircraft engine containment application. *International Journal of Crashworthiness*, 24(1):86–99, 2019. doi: 10.1080/13588265.2017.1422374.

Appendix A

Johnson-Cook Material Model

This model incorporates factors such as strain hardening, strain rate hardening, and thermal softening to provide a comprehensive analysis. These three effects are combined, in a multiplicative manner, as can be depicted from Eq. A.1.

$$\sigma = (A + B(\bar{\varepsilon}^{pl})^n)\left(1 + Cln\frac{\dot{\bar{\varepsilon}}^{pl}}{\dot{\varepsilon_0}}\right)(1 - T^{*m}), \tag{A.1}$$

where σ is the flow stress, $\dot{\bar{\varepsilon}}^{pl}/\dot{\varepsilon_0}$ is the effective plastic strain rate for $\dot{\varepsilon_0} = 1s^{-1}$, $\bar{\varepsilon}^{pl}$ is the effective plastic strain

$$\bar{\varepsilon}^{pl} = \sqrt{\frac{2}{3}\varepsilon_{ij}^{pl}\varepsilon_{ij}^{pl}}, \tag{A.2}$$

and T^* is defined as

$$T^* = \frac{T - T_{room}}{T_{melt} - T_{room}}, \tag{A.3}$$

where T_{melt} is the melting temperature of the material and T_{room} is the reference room temperature. The rest of parameters, A, B, C, n, and **m** are material constants that need to be obtained experimentally.

Furthermore, it is possible to add the Jonson-Cook damage model, which is defined in Eq. A.4. Similarly, constants $\mathbf{D_1}$ to $\mathbf{D_5}$ are obtained experimentally.

$$\varepsilon^f = (D_1 + D_2 e^{D_3\sigma^*})\left(1 + \frac{D_4 ln\dot{\varepsilon}}{\dot{\varepsilon_0}}\right)(1 - D_5 T), \tag{A.4}$$

where ε^f is the strain at fracture and σ^* is the triaxiality $(p/\bar{\sigma})$, the ratio between the average

pressure p and Von Mises equivalent stress

$$\bar{\sigma} = \sqrt{\frac{3}{2} s_{ij} s_{ij}}, \tag{A.5}$$

where s_{ij} is the deviatoric stress tensor. As can be inferred, in the case of high-energy collision, the introduction of such a model is necessary to assess the damage caused to the material due to ballistic impact.

Appendix B

Cowper-Symonds Yield-Scaling Model

There are different ways of accounting for strain-rate effects. The first one is by the definition of different effective true stress vs. effective true plastic strain curves for each loading speed, which can be obtained from dynamic tensile tests. However, this data input can become very extensive, and although LS-DYNA performs a linear interpolation of the curves between the defined maximum and minimum strain rates, this does not apply when higher/lower strain rates are encountered, respectively. Therefore, in order to properly account for the model, it is necessary to have a considerable database that captures the behavior of the material adequately for the entire range of strain rates that can occur throughout the FBO process. While literature may provide some data to use [43], it is possible that it may not always be readily available for all alloys, thereby hindering anyone who wishes to employ the developed model without making large modifications.

The second methodology is by activating the option for the Cowper-Symonds equation (bracketed term in Eq. B.1). It is based on the assumption that, generally for metals, the yield stress escalates with the strain-rate. This model provides the possibility of accounting for this effect without having to collect large amounts of data.

$$\sigma_y(\bar{\varepsilon}^{pl}, \dot{\bar{\varepsilon}}^{pl}) = \left[1 + \left(\frac{\dot{\bar{\varepsilon}}^{pl}}{C}\right)^{1/p}\right] \sigma_y^S(\bar{\varepsilon}^{pl}), \tag{B.1}$$

where σ_y is the yield stress, $\dot{\bar{\varepsilon}}^{pl}$ is the effective plastic strain rate,

$$\dot{\bar{\varepsilon}}^{pl} = \sqrt{\frac{2}{3} D_{ij}^{pl} D_{ij}^{pl}}, \tag{B.2}$$

where D_{ij}^{pl} is the plastic strain rate tensor.

In Eq. B.1 σ_y^S is the yield stress obtained through static loading (user-defined through the already mentioned 8 points along the plastic region) and the term in brackets is the yield stress scaling factor (also referred to as β). The parameters involved in the equation are C [s^{-1}] and p [non-dimensional], which are experimentally obtained.